OPTICAL WIRELESS COMMUNICATION (OWC) UNDERWATER CHARACTERIZATION FOR ROBOT COMMUNICATION SYSTEM

Kamol Boonlom

Submitted in accordance with the requirements for the degree of Doctor of Philosophy

The University of Leeds

Pollard Institute

School of Electronic and Electrical Engineering

June 2025

Intellectual Property and Publication Statements

I confirm that the work submitted is my own, except where work which has formed part of jointly authored publications has been included. My contribution and the other authors to this work have been explicitly indicated below. I confirm that appropriate credit has been given within the thesis where reference has been made to the work of others.

Citation details	K. Boonlom et al., "Advanced Studies on Optical Wireless Communications for in-Pipe Environments: Bandwidth Exploration and Thermal Management," in IEEE Access, vol. 12, pp. 80607-80632, 2024, doi: 10.1109/ACCESS.2024.3410465.
Contribution of the authors	Kamol Boonlom: Methodology, Software, Validation, Experimentation, Writing – Original Draft, Writing – Review & Editing. Pongsathorn Chomtong: Supervision. Weijia Zhang: Supervision. Timothy J Amsdon: Conceptualization, Methodology, Resources, Supervision, Writing – review & editing. Joachim Oberhammer: Supervision. Ian D Robertson: Methodology, Writing – original draft. Nutapong Somjit: Supervision, Writing – original draft, Writing – review & editing.
Chapters in thesis	Chapter 4, Chapter 5

Citation details	K. Boonlom et al., "Multiwavelength Optical Sensing of Water-Level Stratification in Closed Plastic Pipelines Using Signal Attenuation and CIR Analysis," in IEEE Sensors Journal, vol. 25, no. 19, pp. 35991-36001, 1 Oct.1, 2025, doi: 10.1109/JSEN.2025.3598923.
Contribution of the authors	Kamol Boonlom: Methodology, Software, Validation, Experimentation, Writing – Original Draft, Writing – Review & Editing. Nonchanutt Chudpooti: Supervision, Review & Editing. Suppat Rungraungsilp: review & editing. Weijia Zhang: Supervision. Timothy J Amsdon: Conceptualization, Methodology, Resources, Supervision, Writing – review & editing. Joachim Oberhammer: Supervision. Nutapong Somjit: Supervision, Writing – original draft, Writing – review & editing.
Chapters in thesis	Chapter 6

Citation details	K. Boonlom et al., "Multiwavelength Characterization of Optical Wireless Communication in Complex Water-Filled Pipe Environment," in IEEE Access, vol. 13, pp. 163418-163430, 2025, doi: 10.1109/ACCESS.2025.3610711.
Contribution of the authors	Kamol Boonlom: Methodology, Software, Validation, Experimentation, Writing – Original Draft, Writing – Review & Editing. Nonchanutt Chudpooti: Supervision, Review & Editing. Suppat Rungraungsilp: review & editing. Prayoot Akkaraekthalin: Supervision. Weijia Zhang: Supervision. Timothy J Amsdon: Conceptualization, Methodology, Resources, Supervision, Writing – review & editing. Joachim Oberhammer: Supervision. Nutapong Somjit: Supervision, Writing – original draft, Writing – review & editing.
Chapters in thesis	Chapter 6

Thesis outcomes

Parts of this thesis have been published in 3 journal papers and 5 conference papers

Journal papers

1. Kamol Boonlom, Pongsathorn Chomtong, Weijia Zhang, Timothy J. Amsdon, Joachim Oberhammer, Ian D. Robertson, Nutapong Somjit, "Advanced Studies on Optical Wireless Communications for in-Pipe Environments: Bandwidth Exploration and Thermal Management," in IEEE Access, vol. 12, pp. 80607-80632, 2024, doi: 10.1109/ACCESS.2024.3410465.
2. K. Boonlom et al., "Multiwavelength Optical Sensing of Water-Level Stratification in Closed Plastic Pipelines Using Signal Attenuation and CIR Analysis," in IEEE Sensors Journal, vol. 25, no. 19, pp. 35991-36001, 1 Oct.1, 2025, doi: 10.1109/JSEN.2025.3598923.
3. K. Boonlom et al., "Multiwavelength Characterization of Optical Wireless Communication in Complex Water-Filled Pipe Environment," in IEEE Access, vol. 13, pp. 163418-163430, 2025, doi: 10.1109/ACCESS.2025.3610711.

Conference papers

1. K. Boonlom et al., "Active Pre-Equalizer for Broadband Optical Wireless Communication Integrated with RF Amplifier," 2022 Research, Invention, and Innovation Congress: Innovative Electricals and Electronics (RI2C), Bangkok, Thailand, 2022, pp. 251-254, doi: 10.1109/RI2C56397.2022.9910315.
2. K. Boonlom et al., "Illumination and Bandwidth Control Circuit for LED Optical Wireless Transmitter Driver Integrated with Passive Second-Order Equalizer for Pipe Robot Application," 2023 Research, Invention, and Innovation Congress: Innovative Electricals and Electronics (RI2C), Bangkok, Thailand, 2023, pp. 1-5, doi: 10.1109/RI2C60382.2023.10356036.
3. K. Boonlom et al., "Advancing In-Pipe Robot Communication with High-Speed OWC Transceiver Front-End Circuit: Experimental Insights and Prospects," 2024 21st International Conference on Electrical Engineering/Electronics, Computer, Telecommunications and Information Technology (ECTI-CON), Khon Kaen, Thailand, 2024, pp. 1-6, doi: 10.1109/ECTI-CON60892.2024.10595010.
4. K. Boonlom et al., "Optimization of Heatsink Design for Enhanced Thermal Management in LED-Based Optical Wireless Communication Systems for In-Pipe Inspection Robots," 2024 Research, Invention, and Innovation Congress: Innovative Electricals and Electronics (RI2C), Bangkok, Thailand, 2024, pp. 310-315, doi: 10.1109/RI2C64012.2024.10784399.

5. K. Boonlom et al., "Design and Evaluation of Optical Wireless Communication Systems for Underwater IoT Applications," 2024 11th International Conference on Wireless Networks and Mobile Communications (WINCOM), Leeds, United Kingdom, 2024, pp. 1-6, doi: 10.1109/WINCOM62286.2024.10655875.

Acknowledgements

First and foremost, I would like to express my deepest and most sincere gratitude to Associate Professor Dr. Nutapong Somjit, my principal research advisor, for his outstanding supervision, visionary guidance, and unwavering support throughout the course of this research. His enthusiasm for innovation, coupled with his high standards of academic excellence, has served as a constant source of inspiration and motivation. His tireless dedication and strategic direction have been instrumental in shaping the success of this work, and I am truly privileged to have had the opportunity to learn under his mentorship.

My heartfelt thanks also go to Professor Ian D. Robertson, whose expertise and support have significantly contributed to the success of this study. I deeply appreciate his detailed technical guidance on the use of measurement instruments and experimental setups, as well as his generous financial assistance in acquiring essential laboratory equipment and materials required for the project. His mentorship has enriched my knowledge and experimental skills tremendously.

I am also profoundly grateful to my co-supervisor, Associate Professor Dr. Tim Amsdon, for his invaluable technical advice, constructive feedback, and programming expertise related to Optical Wireless Communication (OWC). His consistent guidance and critical insights have been fundamental in navigating the experimental challenges and in ensuring the accuracy and rigor of the research outcomes.

I would also like to express my sincere appreciation to Dr. D Paul Steenson for his excellent technical advice and profound knowledge in the field of optical wireless communication and laser devices. His insights into laser operation principles and optical signal propagation provided valuable depth to this research and significantly enhanced the technical accuracy of the experimental framework.

I would like to express my sincere gratitude to Dr. Li X. Zhang for her invaluable guidance, insightful feedback, and continuous support throughout the writing and editing of this thesis. Her expertise, patience, and encouragement have been instrumental in enhancing the clarity, structure, and overall quality of this work.

I would like to extend my gratitude to my co-authors, especially Professor Joachim Oberhammer and Dr. Weijia, for their valuable contributions in editing and reviewing the manuscript. I am particularly thankful for their support in the simulation and modeling aspects of the project, particularly the implementation and use of Ansys Zemax OpticStudio, which was vital for the optical simulations presented in this thesis.

Special appreciation is also due to the PipeBot Project under the Communication and Power Research Programme, which provided the necessary research funding and logistical support that enabled the successful execution of this work. This platform has also facilitated the real-world application of research findings in autonomous robotic systems, broadening the impact of the study.

I would like to acknowledge the generous support of the Royal Thai Government, my primary sponsor throughout my Ph.D. journey. Without their financial assistance and trust in my academic pursuits, the successful completion of this project would not have been possible. I am grateful for the opportunity to pursue advanced research abroad and contribute knowledge back to my home country.

“I acknowledge the use of ChatGPT-4.0 (Open AI, https://chat.openai.com/) to proofread my final draft.”

Lastly, but most importantly, I extend my deepest love and appreciation to my beloved family. Their unwavering encouragement, emotional support, and countless sacrifices have been the foundation of my academic journey. Their faith in me has been a constant source of strength, and I dedicate this work to them with immense gratitude.

Abstract

This thesis presents a comprehensive study on the design, optimization, and evaluation of LED-based Optical Wireless Communication (OWC) systems within confined pipeline environments, including both air-filled (free-space) and water-filled conditions. The investigation begins with an experimental characterization of light transmission in an empty PVC pipe, where line-of-sight (LOS) and multipath reflections are assessed using multiple wavelength LEDs. Optical enhancements such as collimating lenses and reflectors are integrated and analyzed through simulation and measurement to quantify their effects on received power and frequency bandwidth.

To address the thermal limitations of high-power LEDs, an optimized heatsink structure is developed using heat transfer modeling and validated through SolidWorks CFD simulations. Experimental results confirm that the optimized heatsink significantly improves LED frequency response and receives optical power, with up to a 245% enhancement observed in certain wavelengths compared to conventional cooling solutions.

Subsequently, the thesis focuses on the challenges of underwater optical transmission. Water-filled pipe environments are investigated through both theoretical and experimental frameworks, incorporating Fresnel's reflection theory, Beer–Lambert law, and Henyey–Greenstein scattering models. A controlled testbed is used to evaluate LED performance under various water levels, revealing the wavelength-dependent attenuation behaviors. Simulation results using Ansys Zemax OpticStudio corroborate experimental findings, demonstrating the impact of beam divergence, and material interfaces.

The outcomes of this research provide critical insights into the optical, thermal, and environmental factors influencing OWC in pipeline systems. These findings inform the development of robust, high-efficiency communication platforms for applications in pipeline monitoring, submerged robotics, and smart infrastructure systems.

Table of Contents

List of Tables

List of Figures

Glossary

Acronyms

AGC	Automatic Gain Control
AC	alternating current
ADC	analog-to-digital converter
AIM	Analog Intensity Modulation
APD	avalanche photodiode
AUVs	autonomous underwater vehicles
BER	bit error rate
BRDF	Bidirectional Reflectance Distribution Function
BTDF	Bidirectional Transmittance Distribution Function
CFD	Computational Fluid Dynamics
CIR	Channel Impulse Response
CFR	Channel Frequency Response
CVHD	conventional heatsink
CSK	Color Shift Keying
DLOS	directed line-of-sight
DSO	digital storage oscilloscope
DC	direct current
DD	direct detection
FOV	field of view
FET	field-effect transistor
HG	Henyey-Greenstein
IOPPM	inversion offset pulse position modulation
ISI	inter-symbol interference
IR	infrared
IM	intensity modulation
IoT	Internet-of-Things
IOPs	inherent optical properties
IPHD	improved heatsink

LED	light-emitting diode
LOS	line-of-sight
MIMO	multiple-in-multiple-out
N LOS	nondirected line-of-sight
OOK	on-off keying
Op-amp	operational amplifier
OWC	optical wireless communications
OFDM	Orthogonal Frequency Division Multiplexing
PAM	Pulse Amplitude Modulation
PC	polycarbonate
PD	photodiode/photodetector (interchangeable)
PPM	Pulse Position Modulation
PMMA	polymethyl methacrylate
PWM	pulse-width modulation
PVC	Polyvinyl Chloride
QAM	Quadrature Amplitude Modulation
RGB	red, green and blue
RZ	return-to-zero
ROVs	remotely operated vehicles
SISO	serial-in serial-out
RF	radio frequency
Rx	receiver
SNR	signal-to-noise ratio
TIA	transimpedance amplifier
TIR	total internal reflection
Tx	transmitter
TTL	transistor-transistor logic
TCP	transmission control protocol
UOWC	underwater optical wireless communication
VLC	visible light communications

Notation

A_{Rx}	PD active area
C_D	diode capacitance
C_d	LED depletion capacitance
C_f	feedback capacitance
C_s	LED charge diffusion and storage capacitance
d	distance between transmitter and receiver
E	photon energy (radiated by a light-emitting diode)
f_c	center frequency
$g(\psi)$	optical gain of the concentrator (incidence angle)
$h_{LOS}(t)$	optical channel impulse response
$H_{LOS}(0)$	DC gain for DLOS transmission
$H(f)$	channel frequency response at frequency
I_D	current supplied by the external source
I_p	DC component (average photocurrent)
I_{ph}	generated photocurrent
$P0_{(int)}$	internally generated radiant flux
P_0	average optical power
PRx	optical power received at PD
PTx	optical power transmitted by LED
q	elementary charge of the electron
$R_0(\phi)$	radiant intensity
$R_{\theta JA}$	junction-to-ambient thermal resistance
$R(\lambda)$	responsive at wavelength
$s(t)$	modulation signal
S_{opt}	optimal spacing between adjacent fins
$\delta(t-d/c)$	Dirac delta function
T_j	junction temperature
T_a	ambient temperature
T_{avg}	kinematic viscosity of air

θ	angle in radians
λ	wavelength
τ	pulse period
$\emptyset$	irradiance angle
$\emptyset_{1/2}$	emission half-power/semi-angle/3 dB point
ψ	angle between Tx and Rx, or incidence angle
ψc	FOV angle

Constants

h	Planck's constant (exactly 6.62607015×10−34 $J\ s$)
q	charge of an electron (approximately 1.60217662 ×10−19 C)
k	Boltzmann's constant
	(approximately 1.38064852 ×1023 $m2\ kg\ s{-}2\ K{-}1$)
c	speed of light (approximately 299792458 $m\ s{-}1$)

Chapter 1

Introduction

1.1 Background and Motivation

The increasing demand for autonomous robotic systems in infrastructure inspection and environmental monitoring has driven the development of advanced in-pipe communication technologies. Among various communication methods, Optical Wireless Communication (OWC) has emerged as a promising solution, particularly for short-range, high-speed data transfer in confined and submerged environments such as closed plastic pipelines. Traditional methods, including radio frequency (RF) and acoustic communication, often suffer from severe attenuation, high latency, or susceptibility to interference in these settings, limiting their effectiveness in real-time robotic coordination.

Recent advancements in optoelectronic components, particularly light-emitting diodes (LEDs) operating in the visible light spectrum, have enabled the realization of compact, energy-efficient, and high-bandwidth OWC systems. These systems can overcome the limitations of conventional techniques, offering non-invasive, interference-resistant, and secure line-of-sight communication channels. The unique behavior of light under varying fluid conditions, particularly within water-filled or stratified PVC pipes, opens new research opportunities for robotic communication and embedded sensing in underwater and subterranean infrastructure.

1.2 Problem Statement

Despite the promise of OWC systems in pipe-based applications, significant challenges remain in understanding and optimizing light propagation under dynamic water conditions. Light transmission in such environments is strongly influenced by absorption, scattering, and reflection at material interfaces and media boundaries. The presence of air–water stratification, variations in water fill levels, and pipe surface roughness further complicate the channel characteristics, affecting signal strength, bandwidth, and impulse response.

Most prior studies have focused on homogeneous water environments or open containers, leaving a research gap in characterizing light transmission behavior in closed, stratified, and partially filled pipeline systems. A detailed analysis of how different wavelengths interact with these media, including their frequency response and channel impulse response (CIR), is essential for optimizing in-pipe OWC systems for robotic communication tasks.

1.3 Research Objectives

This research aims to develop a comprehensive understanding of optical wireless communication in water-filled pipe environments for robotic applications. The specific objectives are as follows:

1. To characterize the transmission properties of visible-light LEDs (475 nm, 528 nm, 583 nm, and 625 nm) across varying water levels inside PVC pipes.
2. To investigate the absorption, scattering, and reflection effects at air–water and water–pipe interfaces using both experimental and simulation methods.
3. To model and analyze the channel impulse response (CIR) under stratified water conditions and evaluate its dependence on wavelength and fill level.
4. To validate experimental measurements with raytracing and Monte Carlo simulations using Ansys Zemax OpticStudio and Keysight ADS tools.
5. To derive design guidelines for efficient in-pipe OWC systems applicable to autonomous robotic platforms.

1.4 Research Questions

Based on the stated objectives and the identified research gaps, this study is guided by the following key research questions:

1. How do optical and material properties of PVC and stratified water layers affect light propagation within confined in-pipe environments?
   – This question addresses the lack of empirical data on wavelength-dependent reflection, absorption, and scattering in non-homogeneous media.
2. What is the quantifiable impact of LED thermal management on optical output power, modulation bandwidth, and overall system performance in OWC transmitters?
   – This question investigates the relationship between junction temperature and communication efficiency, contributing new knowledge on the thermal–optical coupling mechanism in LED-based OWC systems.
3. How do varying water levels and stratified interfaces influence signal attenuation, scattering, and channel impulse response (CIR) within PVC pipelines?
   – This explores the dynamic interaction between environmental factors and optical channel characteristics, a gap largely overlooked in existing literature.
4. Which LED wavelength and optical configuration (reflector/lens combination) yield the optimal balance between bandwidth, signal-to-noise ratio (SNR), and channel capacity for in-pipe OWC?
   – This provides a performance-based guideline for selecting LED wavelengths and optical components tailored to confined aquatic communication.
5. How can the integration of thermal, optical, and environmental modeling frameworks advance the design of efficient OWC systems for robotic pipeline inspection and underwater communication?
   – This synthesizes the study's multidisciplinary approach into a coherent design methodology, extending the current state-of-the-art in confined OWC system design.

1.5 Scope and Limitations

This study focuses on short-range optical transmission in static, sealed PVC pipe sections with controlled water fill levels (0%, 25%, 50%, 75%, and 100%). The analysis is limited to four monochromatic LED wavelengths in the visible spectrum.

The water medium is assumed to be clear tap water, with negligible turbidity or particle load.

While both experimental measurements and simulation models are employed, the study does not address dynamic flow conditions, turbulent mixing, or long-distance multi-hop communication scenarios. Furthermore, the mechanical integration of optical components into a full robotic system is beyond the scope, although the implications for robotic design are discussed.

1.6 Thesis Organization

The remainder of this thesis is organized as follows:

- Chapter 2: Literature Review presents a comprehensive overview of OWC systems, light propagation theories in fluidic environments, and previous studies on in-pipe and underwater optical transmission.
- Chapter 3: Theoretical Framework introduces the core physical models used in this research, including Beer–Lambert law, Fresnel reflection, and CIR analysis.
- Chapter 4: This chapter presents baseline OWC measurements in empty PVC pipes, analyzing LOS/NLOS transmission, multipath effects, and LED frequency response. Using various LEDs and optical components, it evaluates received power and bandwidth to inform system design for more complex environments.
- Chapter 5: This chapter investigates an optimized square-fin heatsink to enhance LED cooling and bandwidth. Using heat transfer principles, the design maximizes airflow efficiency. LED performance is evaluated across five wavelengths under varying bias currents (10–1,000 mA).
- Chapter 6: This chapter investigates the performance of OWC systems in water-filled pipelines using LEDs of various wavelengths. It examines how water levels affect attenuation, received power, and channel behavior. The results guide wavelength selection and system design for effective in-pipe optical communication.
- Chapter 7: Conclusion and Future Work summarize the main findings and propose future directions, including real-time robotic integration and advanced optical modulation techniques.

1.7 Novel Contributions

This research makes several novel contributions to the field of Optical Wireless Communication (OWC) for underwater and in-pipe robotic systems. Unlike most previous studies that focus on open-tank or homogeneous water environments, this work investigates OWC performance within confined, stratified, and partially filled pipeline systems—conditions representative of real-world robotic inspection and sensing applications. The major contributions are summarized as follows:

- **Experimental Characterization of OWC in Stratified In-Pipe Environments**

A systematic experimental framework was developed to measure optical signal transmission in PVC pipes at varying water fill levels (0%–100%). This is one of the first studies to quantify how stratified air–water interfaces influence attenuation, scattering, and received signal strength for multiple visible wavelengths.

- **Multi-Wavelength Optical Channel Analysis**

Four visible-light LEDs (475 nm, 528 nm, 583 nm, 625 nm) were analyzed to determine wavelength-dependent absorption and scattering behavior. The comparative results establish empirical relationships between wavelength selection and communication performance under different optical path conditions.

- **Integration of Simulation and Empirical Modeling**

The study combines Ansys Zemax OpticStudio raytracing and Keysight ADS circuit-level simulations with measured data. This dual-domain approach provides a validated methodology for predicting channel impulse response (CIR) and received power in complex water–pipe geometries.

- **Introduction of Channel Impulse Response (CIR) Modeling for In-Pipe OWC**

A time-domain CIR framework was proposed to capture multipath effects and signal dispersion within partially filled pipelines. This modeling approach extends traditional underwater OWC analysis into confined geometries and offers new insight into temporal spreading and link reliability.

- **Design Guidelines for Robotic Optical Communication Systems**

Based on experimental and simulation results, the research formulates practical design criteria for wavelength selection, transmitter–receiver alignment, and power optimization. These guidelines directly support the integration of compact OWC modules into autonomous robotic platforms for pipeline inspection and environmental monitoring.

- **Thermal and Optical Optimization of LED Transmitters**

A thermally enhanced LED transceiver using an optimized square-fin heat-sink design was developed and characterized. The improved thermal management significantly increases LED bandwidth and optical stability under high-current operation, contributing to higher data-rate capability in submerged applications.

Collectively, these contributions establish a comprehensive framework for analyzing, modeling, and optimizing short-range OWC in confined aquatic environments. The results advance the state of the art in underwater robotic communication and provide a foundation for future integration of adaptive modulation and multi-robot optical networking.

Chapter 2

Literature Review

2.1 Overview of Optical Wireless Communication (OWC)

Optical Wireless Communication (OWC) refers to the transmission of modulated optical signals through free space or transparent media without physical conductors. Unlike radio frequency (RF) or acoustic systems, OWC employs infrared, visible, or ultraviolet light for high-speed data exchange. This technology offers several advantages—wide unregulated bandwidth, immunity to electromagnetic interference, and compact low-power transceivers—making it a strong candidate for environments where RF and acoustic signals are unreliable.

OWC systems are generally composed of a light source (LED or laser diode), a propagation medium (air, water, or plastic), and a photodetector receiver with amplification circuitry. Data are typically encoded in the light's intensity or phase using modulation schemes such as On-Off Keying (OOK), Pulse-Position Modulation (PPM), or Orthogonal Frequency-Division Multiplexing (OFDM), depending on requirements for bit-error rate, spectral efficiency, and hardware complexity (1).

Visible Light Communication (VLC), which uses LEDs operating between 400–700 nm, is particularly attractive because it enables dual functionality for both illumination and data transfer. LEDs offer fast switching speed, low heat dissipation, and inexpensive manufacturing, while silicon photodiodes provide high sensitivity in the visible spectrum (2). These attributes enable robust and energy-efficient links suitable for robotic platforms and embedded systems.

In underwater or in-pipe conditions, RF waves are heavily attenuated by conductive media and boundary losses, whereas visible light—especially within the blue-green band—can propagate several meters depending on turbidity and water composition. However, wavelength-dependent absorption, scattering, and interface reflection significantly influence link performance (3). Understanding and mitigating these effects are essential for designing reliable OWC systems in confined environments.

2.2 Communication Challenges in Underwater Environments

Underwater environments pose severe challenges for wireless data transmission due to absorption, multipath propagation, and noise. As autonomous robotic systems are increasingly deployed in submerged pipelines and reservoirs, the selection of an appropriate communication method becomes critical.

2.2.1 Limitations of Radio Frequency (RF) Communication

RF signals experience strong attenuation in water, particularly above a few hundred kilohertz. In seawater, the skin depth is only a few centimeters at MHz

frequencies, limiting usable communication to very low frequencies (< 30 kHz). Such low frequencies require large antennas, high power, and yield low data rates, making RF unsuitable for compact or battery-powered robots (4). In non-metallic pipes, additional dielectric losses and interface reflections further reduce transmission efficiency.

2.2.2 Constraints of Acoustic Communication

Acoustic communication, while capable of long-range propagation, offers limited bandwidth and high latency because the sound speed in water is only ~1500 m/s. Bandwidth decreases with distance—around 1 kHz at 100 km—and data rates rarely exceed tens of kilobits per second. Furthermore, performance is degraded by multipath propagation, Doppler effects, and environmental noise from flow turbulence, reverberation, and surface reflections. These factors make acoustic systems impractical for real-time, high-throughput robotic tasks such as imaging or video streaming (5).

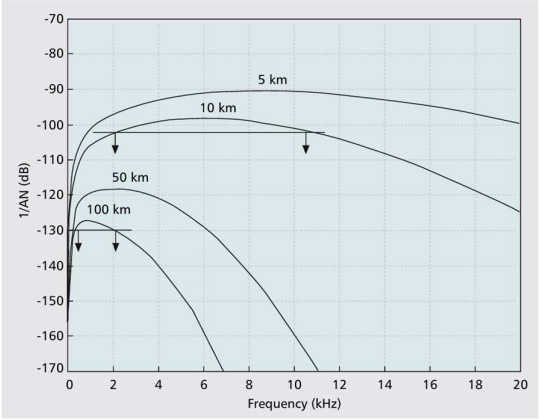

Figure 2.1 The SNR in an acoustic channel varies depending on frequency and distance (Stojanovic & Preisig, 2009) (5).

2.2.3 Optical Wireless Communication Constraints

OWC offers substantially higher bandwidth but is limited by absorption, scattering, and refraction. The absorption coefficient of water increases with wavelength, making blue-green light (≈ 450–550 nm) the optimal transmission window. Scattering from particles and microbubbles widens the beam and reduces received power, while Fresnel reflections and Snell's refraction at interfaces (e.g., air–water or water–pipe) cause energy losses and beam misalignment. In turbid or stratified water, spatial variations in refractive index distorts the beam and decreases link reliability (3).

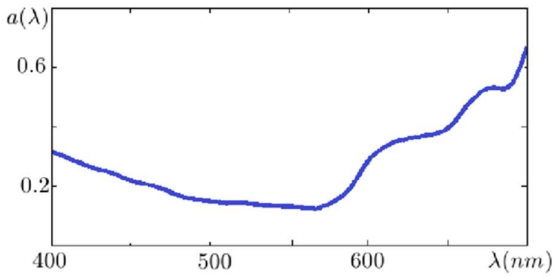

Figure 2.2 Coastal water absorption spectra (3).

2.2.4 Structural and Environmental Constraints

Pipe geometry, curvature, diameter, and material significantly affect optical propagation. PVC pipes, for example, exhibit strong internal reflections and scattering. Environmental variables such as temperature, salinity, and biofouling alter absorption over time, necessitating adaptive modeling and dynamic link optimization (6).

2.2.5 Implications for Robotic Systems

Autonomous robots operating in water-filled pipelines require compact, low-latency communication links. While RF and acoustic methods fall short in bandwidth and responsiveness, OWC provides high-speed interference-free data transfer if its range and alignment challenges are addressed. This motivates experimental and simulation-based investigations—such as those presented in this thesis—to optimize OWC performance under variable water levels and material boundaries.

2.3 State-of-the-Art in Underwater Optical Wireless Communication

Recent progress has transformed underwater OWC from laboratory curiosity into a viable high-speed communication technology. Research between 2020 and 2025 demonstrates significant enhancements in range, reliability, and adaptability through improved modulation, hybrid integration, and intelligent control.

- **High-Speed Demonstrations**

(Arvanitakis et al., 7) achieved 1 Gbps transmission over 6 m in clear water using blue LED arrays and OFDM. Similarly, (Ge et al., 8) realized 500 Mbps over 4 m using multiple parallel optical channels, highlighting the potential of multiplexed architectures. These results confirm that OWC can outperform acoustic systems by several orders of magnitude in bandwidth for short-range communication.

- **Adaptive and Machine-Learning-Aided Systems**

(Zhang et al., 9) introduced a neural-network-based channel estimator capable of predicting attenuation and optimizing LED drive currents in real time. (Chen et al. , 10) developed an adaptive beam-steering mechanism for autonomous underwater vehicles (AUVs), maintaining alignment despite flow disturbances. Such intelligent

techniques enable dynamic control of beam direction, modulation index, and wavelength.

- **Hybrid Optical–Acoustic Networks**

(Luo et al., 11) proposed a hybrid system that switches between optical and acoustic links depending on turbidity levels, maintaining connectivity in variable underwater conditions. Similar architectures have been used for mobile robotic swarms to ensure reliable data transfer in turbid coastal regions.

- **Energy-Efficient and MIMO Techniques**

(Li et al., 12) demonstrated multiple-input multiple-output (MIMO) optical links achieving up to 60% energy savings while sustaining high throughput. Integration of OFDM and adaptive biasing further enhances spectral efficiency and reduces flicker noise.

Despite these advancements, most reported systems operate in open-tank or open-sea conditions. There remains limited research on OWC performance inside enclosed or partially filled pipelines, where curved boundaries and stratified layers introduce unique multipath and reflection phenomena. Addressing this gap is central to the present thesis.

2.4 Gaps in Current Research

Despite considerable advancements in wireless communication technologies for robotic systems, several critical gaps remain, particularly in the domain of underwater and in-pipe environments. These limitations hinder the effective deployment of high-performance, autonomous robotic systems in real-world infrastructure applications. A review of existing literature highlights the following key areas where further research is needed.

2.4.1 Limited Focus on Stratified Water Environments

Most current studies on underwater optical wireless communication (UOWC) systems assume a homogeneous medium, such as clear open water or fully submerged tanks. However, in real-world pipeline environments, water often exists in stratified layers—a mix of air, water, and sometimes sediment or gas pockets. These layered media introduce non-uniform refractive indices, surface reflections, and localized scattering effects, all of which affect the transmission characteristics of optical signals. There is a notable lack of research exploring how these stratified interfaces alter channel behavior, signal strength, or impulse response in OWC systems.

2.4.2 Insufficient Characterization of In-Pipe Optical Channels

While some efforts have been made to model underwater optical channels in controlled testbeds, the optical propagation characteristics inside enclosed, narrow-diameter pipelines remain under-explored. Such environments exhibit unique challenges, including multiple boundary reflections, complex beam-path geometries, and high sensitivity to surface roughness and curvature. Few existing studies have

systematically evaluated how pipe diameter, material (e.g., PVC), and geometry influence light transmission and scattering. Additionally, attenuation trends in partially filled or curved pipe segments are largely undocumented, yet crucial for optimizing in-pipe communication systems.

2.4.3 Lack of Multi-Wavelength Comparative Studies

Many prior works focus on single-wavelength analysis, particularly around the blue-green spectrum (~470–530 nm), which has the lowest absorption in water. However, multi-wavelength studies that compare the performance of various visible-light LEDs across different water depths and turbidity levels are limited. The interaction between wavelength and media properties, including absorption coefficient, beam divergence, and CIR behavior—must be better understood to inform optimal wavelength selection for specific environmental conditions.

2.4.4 Underutilization of CIR Modeling in UOWC

Channel Impulse Response (CIR) modeling is critical for analyzing multipath propagation, signal delay spread, and bandwidth performance in optical communication systems. Although CIR is a standard analytical tool in RF and acoustic domains, its application in underwater or in-pipe optical environments is still limited. Recent studies have begun to explore time-domain CIR analysis using Monte Carlo simulations and ray tracing, but there is a lack of empirical validation in structured pipeline settings. The incorporation of CIR metrics into OWC system design remains an open area for enhancement.

2.5 Conclusion

This chapter reviewed the fundamentals, challenges, and modern developments of underwater and in-pipe communication technologies. OWC stands out for its large bandwidth, low latency, and immunity to electromagnetic interference, positioning it as a key enabler for next-generation robotic and sensor systems. However, its real-world implementation is constrained by absorption, scattering, and alignment sensitivity in confined or turbid media.

The state-of-the-art analysis revealed significant progress in high-speed modulation, adaptive beam control, and hybrid architectures, yet little attention has been given to optical transmission in stratified, enclosed, or pipeline environments. This thesis therefore aims to experimentally and numerically characterize the underwater optical channel under these practical conditions, providing the groundwork for efficient robotic communication within submerged infrastructures.

Chapter 3

Theoretical Framework

3.1 Light Propagation in Water

The behavior of light in underwater environments is shaped by three primary phenomena: absorption, scattering, and refraction. These physical processes are influenced by the inherent optical properties of water such as temperature, salinity, turbidity—and by environmental conditions and medium interfaces. For Optical Wireless Communication (OWC) systems operating in stratified, confined environments like pipelines, understanding these processes is vital for accurately modeling signal attenuation, distortion, and propagation reliability.

3.1.1 Absorption and Scattering

Absorption occurs when photons lose energy to the medium, typically transforming into heat. The absorption level depends on the water composition and is highly wavelength dependent. Blue-green wavelengths (450–550 nm) have minimal absorption, making them optimal for underwater OWC, while red and infrared light are significantly attenuated within just a few centimeters (3).

Scattering is the redirection of light due to interaction with particles or inhomogeneities in the medium. It can be classified as:

- Rayleigh scattering, dominant when particles are much smaller than wavelength,
- Mie scattering, significant when particles are comparable in size to the wavelength.

In real underwater environments—especially in pipelines—Mie scattering often dominates due to suspended sediments, biological matter, and microbubbles. These effects lead to beam divergence and signal dispersion, especially in turbid water.

The combined impact of absorption and scattering is quantified by the attenuation coefficient, often modeled via the Beer–Lambert Law, which describes the exponential reduction in light intensity with distance. This principle is critical in estimating the power budget for OWC systems deployed in varying water depths and quality conditions (13).

3.1.2 Surface Roughness Scattering for the PVC Pipe Surface, Water, and Air

- Scattering from PVC Pipe Surfaces

The internal surfaces of PVC pipes, which are commonly used in water infrastructure, are generally not optically smooth. Factors such as manufacturing inconsistencies, surface aging, biofilm accumulation, or mineral fouling contribute to microscale surface roughness. When a collimated optical beam strikes such a rough surface, light is no longer reflected uniformly; instead, it undergoes non-specular reflection, resulting in angular scattering. Even surface deviations on the order of the incident light's wavelength can cause significant diffuse reflection (14).

These scattering phenomena are mathematically characterized by the Bidirectional Reflectance Distribution Function (BRDF) and, in transmissive cases, by the Bidirectional Transmittance Distribution Function (BTDF). These models are fundamental in radiative transfer theory and are widely used in simulation software for optical system design.

- The BRDF quantifies how much light is reflected in each direction from a surface when illuminated from another specific direction. It is defined as the ratio of reflected radiance in each outgoing direction to the incident irradiance from a given incoming direction:

$$BRDF\left(\theta_i,\phi_i;\theta_r,\phi_r\right)=\frac{dL_r\left(\theta_r,\phi_r\right)}{dE_i\left(\theta_i,\phi_i\right)} \tag{3.1}$$

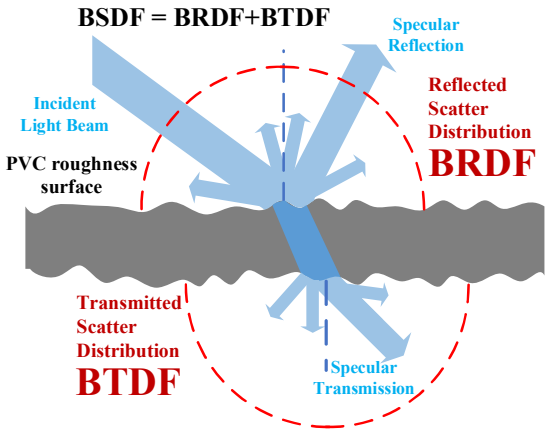

Figure 3.1 Illustrates the effect of microscale surface roughness on optical signal propagation within a PVC pipe (14).

where θ and ϕ denote the zenith and azimuth angles for the incident (i) and reflected (r) directions, L_r is the reflected radiance, and E_i is the incident irradiance.

- The BTDF similarly describes light transmission through a surface, mapping the distribution of transmitted radiance over exit angles for a given incident beam. It is essential when light traverses from one medium to another—such as from air through a clear acrylic pipe wall into water—where surface irregularities may also scatter the beam.

In the context of OWC in PVC pipelines, the BRDF is particularly relevant because most internal surfaces behave as partially diffuse reflectors. Real PVC materials exhibit a mixed scattering profile, falling between purely specular (mirror-like) and perfectly diffuse (Lambertian) reflection. The BRDF allows this hybrid behavior to be accurately modeled, predicting how much light is scattered at various angles after contact with rough pipe walls.

This angular dispersion causes the optical beam to lose collimation, reducing the energy that reaches the photodetector. As a result, the Channel Impulse Response

(CIR) broadens, increasing temporal spread and causing intersymbol interference (ISI)—a major concern for high-speed data transmission in narrow pipeline geometries.

Furthermore, although BTDF plays a less direct role inside opaque PVC pipes, it becomes crucial in segments where light must transmit through boundaries, such as acrylic windows or protective enclosures. In these cases, surface roughness on the transmissive interface can redirect light away from the intended optical path, compounding losses.

- Scattering within the Water Medium

Even clear water is subject to volumetric scattering, caused by suspended particulates, refractive index gradients, or biological elements. In pipelines, stratified water layers with differing temperatures or salinity act as optical discontinuities, further scattering and refracting light unpredictably (13), (15).

Mie scattering dominates in these environments, particularly when particle sizes approach or exceed the wavelength of light used. The result is reduced signal coherence and lower received power, especially in turbid or biologically active water (16).

- Implications for OWC System Design

These scattering phenomena—whether from PVC walls, air–water interfaces, or within the water itself—pose several design challenges:

- Angular spread increases the loss of collimated light,
- Temporal dispersion degrades signal timing and bandwidth,
- Environmental variability causes inconsistent communication performance.

To mitigate these effects, designers may implement:

- Narrow-beam LEDs to reduce wall and surface interaction,
- Spatial filtering at the receiver to reject scattered rays,
- Adaptive modulation and coding to combat multipath distortion.

This research integrates both experimental measurements and ray-tracing simulations to assess how surface roughness and scattering influence OWC performance in partially water-filled pipes.

3.1.3 Refractive Index Variations

Refraction governs the bending of light as it passes across boundaries between materials of different optical densities. This phenomenon is mathematically described by Snell's Law, which relates the angle of incidence to the angle of refraction as follows:

$$n_1.\sin(\theta_1) = n_2.\sin(\theta_2) \tag{3.2}$$

where n_1 and n_2 are the refractive indices of the incident and transmission media, respectively, θ_1 is the angle of incidence, θ_2 is the angle of refraction.

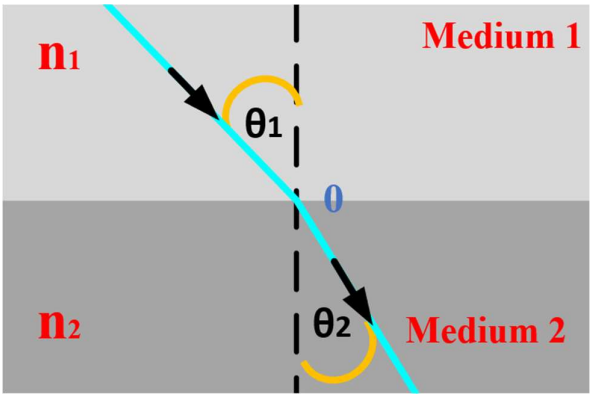

Figure 3.2 Refraction occurs when light traverses the boundary between two distinct media (17).

In optical wireless communication (OWC) systems, light typically propagates through multiple layers—starting in air, then through the pipe wall material (e.g., PMMA or acrylic), into water, and eventually reflecting off the inner PVC surface. At each of these interfaces, the direction of beam propagation is governed by Snell's Law, which describes the angular change of light due to the contrast in refractive indices between adjoining media. Additionally, the Fresnel equations determine the proportion of light that is reflected versus transmitted at each boundary. These equations are particularly critical in OWC systems where interfaces between air, solid, and liquid introduce discontinuities that affect both signal power and directionality (13).

The Fresnel equations describe the reflection and transmission of light based on the refractive indices of the two media and the angle of incidence. For unpolarized light, the reflectance R at an interface can be approximated as the average of the parallel (R_p) and perpendicular (R_s) polarization components:

$$R(\theta_i) = \frac{1}{2}\left[\left(\frac{n_i\cos\theta_i - n_t\cos\theta_t}{n_i\cos\theta_i + n_t\cos\theta_t}\right)^2 + \left(\frac{n_i\cos\theta_t - n_t\cos\theta_i}{n_i\cos\theta_t + n_t\cos\theta_i}\right)^2\right] \tag{3.3}$$

where n_1 and n_2 are the refractive indices of the incident and transmitted media, and θ_i and θ_t are the angles of incidence and transmission, respectively (18). These relationships highlight that reflective losses increase with larger index mismatches and higher angles of incidence. In confined OWC channels, such as pipelines, this leads to partial reflection at each boundary—most notably at the air–acrylic and acrylic–water interfaces—resulting in multipath propagation and reduced energy transfer to the receiver.

The refractive index of water, approximately 1.333 at 20 °C, is not constant; it exhibits slight variation with wavelength (dispersion), temperature, and salinity (19). In stratified pipeline environments, such as those where partially filled flow or layered thermal/salinity gradients exist, these variations create refractive index gradients. As light travels through these layers, it experiences gradual redirection, a process known as optical lensing, which can distort the beam path and shift it away from the intended line-of-sight, thereby affecting detection and communication reliability (13), (20).

Furthermore, partial reflection occurs at every optical interface, especially at the air–water boundary, where mismatched refractive indices, combined with surface roughness and curvature, intensify light scattering and reflection losses. The result is a reduction in transmitted optical power, misalignment of optical paths, and degradation of signal quality.

To accurately model these effects, this study employs Ansys Zemax OpticStudio, a ray-tracing software that simulates the impact of refractive index variations, surface reflections, and layered media interfaces on beam propagation. This enables a precise evaluation of signal behavior under different pipeline fill levels and guides the design of robust OWC systems for in-pipe robotic communication.

3.2 Optical Transmission Model

3.2.1 Lambertian Emission

In optical wireless communication (OWC) systems, particularly those utilizing light-emitting diodes (LEDs) as transmitters, the angular distribution of emitted optical power plays a critical role in determining the signal propagation characteristics. Most commercial LEDs exhibit a Lambertian radiation pattern, which models the emission intensity as a function of the cosine of the angle from the LED's optical axis.

A Lambertian source is defined as one that emits light with intensity proportional to the cosine of the emission angle ϕ, relative to the normal surface. The radiant intensity $R_0(\phi)$ of a Lambertian emitter is described by:

$$R_0(\emptyset) = \left[\frac{m+1}{2\pi}\right] cos^m(\emptyset) \tag{3.4}$$

where ϕ is the angle between the surface normal and the observation direction, mmm is the Lambertian emission order, which quantifies the directionality of the LED beam, $R_0(\phi)$ is normalized such that the total emitted power is distributed across a hemisphere (21).

The Lambertian order mmm is determined based on the semi-angle at half-power $\phi_{1/2}$, which is the angle at which the emitted power falls to 50% (−3 dB) of the maximum on-axis power. The relation is given by:

$$m = \frac{-ln2}{ln\left(cos\left(\emptyset_{1/2}\right)\right)} \tag{3.5}$$

As $\phi_{1/2}$ decreases (i.e., the LED becomes more directional), the Lambertian order *m* increases, indicating a narrower beamwidth. Conversely, larger semi-angles correspond to more diffused radiation profiles with lower *m* values.

Understanding and modeling Lambertian emission is essential for channel modeling, link budget analysis, and beam shaping in OWC systems. In confined or reflective environments—such as underwater pipes or robotic inspection platforms, the angular distribution defined by Equations (3.4) and (3.5) helps predict how much optical power reaches the receiver under various alignment and scattering conditions.

In practical terms: Low *m* values (e.g., $m \approx 1$m) result in wide-angle emissions suitable for broad coverage.

High *m* values (e.g., $m > 10$m) produce more collimated beams ideal for point-to-point links.

The Lambertian model is widely used in OWC simulation platforms and optical design tools, offering a computationally tractable approximation for real-world LED emission profiles.

3.2.2 Directed Line-of-Sight (DLOS) Transmission Model

In optical wireless communication (OWC) systems, the Directed Line-of-Sight (DLOS) model is a fundamental configuration in which the LED transmitter and the photodetector (PD) receiver are precisely aligned, ensuring that the light beam travels directly between them without relying on reflections. This model assumes minimal or no multipath interference, meaning that reflections from surrounding surfaces such as walls, ceilings, floors, or objects are not received or are negligible in their effect (22).

The direct current (DC) channel gain $H_{LOS}(0)$, representing the fraction of transmitted optical power collected by the receiver, is given by:

$$H_{LOS}(0) = \begin{cases} \frac{A_{Rx}}{d^2} R_0(\emptyset) cos(\psi), & 0 < \psi < \psi_C \\ 0, & elsewhere \end{cases} \tag{3.6}$$

where A_{rx} is the physical area of the PD receiver, *d* is the separation distance between the LED transmitter and the PD receiver, $R_0(\phi)$ is the radiant intensity of the LED as a function of the emission angle ϕ, modeled using the Lambertian distribution, ψ is the angle of incidence at the PD, ψ_C is the field of view (FOV) of the photodetector, which limits the acceptance angle beyond which the receiver does not detect incoming light.

This equation incorporates the inverse-square law ($1/d^2$), which represents the free-space path loss—i.e., the decrease in received power with increasing distance

due to the spatial dispersion of light (23). In ideal DLOS configurations, the incidence angle $\psi=0^{\circ}$, meaning the LED beam is perfectly aligned with the PD. Under these conditions, the received optical power is maximized.

The diagrammatic representation of Equation (3.6), as shown in Figure 3.3, visualizes this ideal scenario. In the illustration, the LED's optical beam is incident perpendicularly on the photodiode surface, which ensures that both $cos(\psi)$ and $cos(\varphi)$ equal 1, delivering the maximum possible channel gain.

Several system design parameters influence the received optical power in DLOS:

- Reducing the LED's irradiance angle (i.e., narrowing its beam) concentrates the emitted power and enhances intensity in the forward direction, improving the received signal.
- Increasing the PD's surface area increases the amount of light captured, thereby improving signal reception and overall system sensitivity.

However, these improvements introduce trade-offs:

- A larger PD surface area results in increased junction capacitance, which reduces the bandwidth of the receiver by limiting its electrical response speed (22).
- Furthermore, a larger detector area increases the susceptibility to background noise and ambient light interference, potentially degrading the signal-to-noise ratio (SNR).

Thus, optimizing a DLOS-based OWC link involves balancing the alignment, optical geometry, and receiver dimensions to achieve both high signal strength and adequate system bandwidth while minimizing noise and path loss.

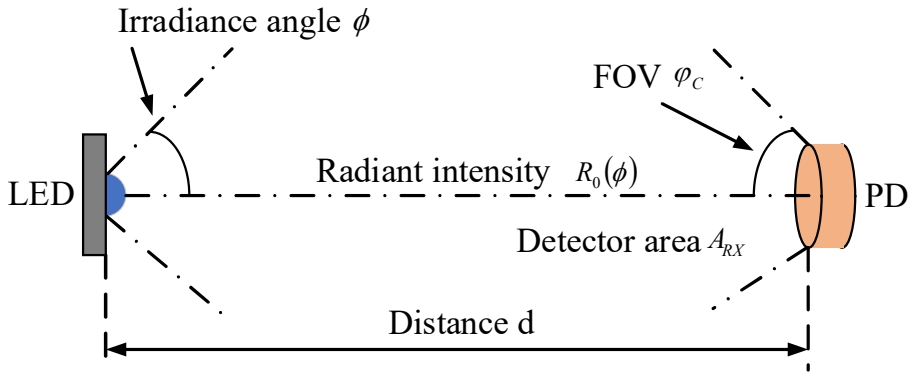

Figure 3.3 DLOS transmission with spatial components (22).

In conventional optical wireless communication (OWC) systems, when the photodetector (PD) collects only the photons that directly strike its active area, the system is classified as a non-imaging configuration. This is illustrated in Figure 3.3, where the PD is positioned to capture light within its defined field of view (FOV) but does not use any optical elements to reshape or redirect incoming light. While simple

and compact, such configurations may suffer from limited optical power reception, particularly when the emitted light is diffused or the distance from the transmitter is substantial.

To address this limitation, optical concentrators can be integrated into the receiver design, as depicted in Figure 3.4. These concentrators—such as compound parabolic concentrators (CPCs) or lens-based systems—are designed to collect and focus a broader range of incident light angles onto the photodiode, thereby enhancing the effective collection area without increasing the physical size of the PD (22). The gain of the concentrator, denoted $g(\phi)$, is a function of the angle of incidence ϕ and serves to amplify the received optical power while preserving the geometric alignment of the DLOS link.

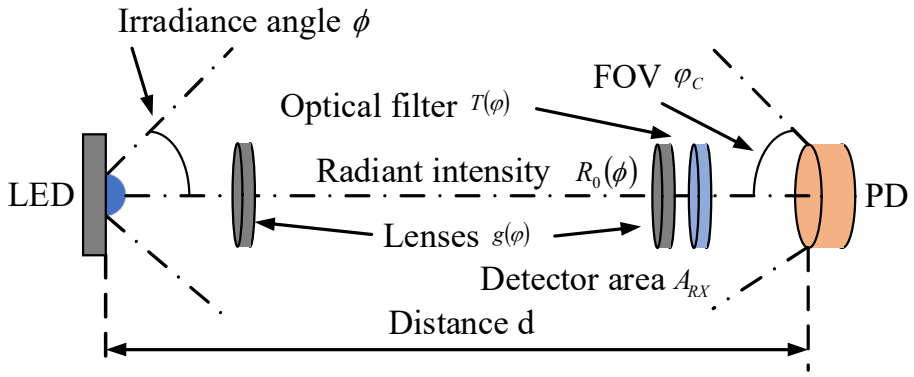

Figure 3.4 Directed LOS transmission using optical filters and concentrators (22).

In parallel, optical filters are often used to selectively transmit specific wavelength bands, especially in systems using phosphor-coated white LEDs, which emit both fast (blue) and slow (phosphorescent) components. These band-pass filters are employed to suppress the slower components, thereby improving the modulation bandwidth of the received signal. However, filters introduce optical attenuation, as only a portion of the incident light is transmitted through. This filter transmittance is represented by $T(\phi)$, which also varies with the incident angle.

The gain of an ideal non-imaging optical concentrator is defined by Equation (3.7). This gain accounts for the concentrator's ability to enhance the optical power incident on the photodetector (PD) by focusing incoming light within its acceptance angle. The gain $g(\phi)$ is given as (22):

$$g(\varphi) = \begin{cases} \frac{n^2}{sin^2\psi_C}, & 0 \le \psi \le \psi_C \\ 0, & \psi > \psi_C \end{cases} \tag{3.7}$$

where n is the refractive index of the concentrator material, ψ is the angle of incidence at the PD, ψ_C is the field of view (FOV) of the receiver, and the condition

$\psi_C \leq 2/\pi$ ensures proper concentration behavior within geometric limits. To incorporate both concentrator gain and optical filter attenuation, the DC channel gain expression in Equation (3.6) is modified, resulting in Equation (3.8):

$$H_{LOS}(0) = \begin{cases} \frac{A_{RX}}{d^2} R_0(0) cos(\psi) g(\varphi) T(\varphi), & 0 \leq \psi \leq \psi_C \\ 0, & elsewhere \end{cases} \quad (3.8)$$

Here A_{rx} is the area of the PD, d is the distance between transmitter and receiver, $R_0(0)$ is the radiant intensity of the LED at normal incidence, $g(\phi)$ is the concentrator gain, $T(\phi)$ represents the transmittance of the optical band-pass filter. With this adjusted DC gain, the optical power received at the photodetector is computed using:

$$P_{RX} = H_{LOS}(0) P_{TX} \quad (3.9)$$

where P_{Rx} is the power received at the PD, P_{Tx} is the transmitted optical power from the LED. The optical wireless channel can thus be modeled as a linear system with both attenuation and propagation delays. The corresponding impulse response of the channel, accounting for time delay d/c, is given by:

$$H_{LOS}(t) = \frac{A_{RX}}{d^2} R_0(0) cos(\psi) g(\varphi) T(\varphi) \delta\left(t - \frac{d}{C}\right) \quad (3.10)$$

In this expression:

- $\delta(t - d/c)$ is the Dirac delta function, representing the signal delay,
- c is the speed of light in free space.

This model provides a foundation for evaluating signal propagation in direct line-of-sight (DLOS) optical links, where geometric alignment, optical filtering, and concentration mechanisms collectively determine system performance.

3.2.3 Non-Directed Line-of-Sight (NLOS) Transmission Model

In contrast to the Directed Line-of-Sight (DLOS) configuration, the Non-Directed Line-of-Sight (NLOS) transmission model does not rely on direct alignment between the transmitter and receiver. Instead, it assumes that the photodetector (PD) receives optical signals via reflections and scatters from surrounding surfaces such as walls, ceilings, floors, or environmental features. This model is particularly relevant for indoor environments and constrained spaces like pipes or tunnels, where direct optical paths may be obstructed or geometrically impractical (22).

Figure 3.5 illustrates an optical wireless communication scenario in which the LED transmitter emits light diffusely, following a Lambertian pattern. The emitted light reflects off an intermediate surface (e.g., wall or ceiling), and the reflected optical signal is captured by the photodetector (PD) positioned within its field of view (FOV). The geometry highlights the angles of emission ϕ and incidence ψ, as well as the distances from the transmitter to the reflecting surface d_1, and from the surface to the receiver d_2. The NLOS model accounts for surface reflectivity, angular dependencies, and multipath effects, and is typically used in environments where direct line-of-sight between transmitter and receiver is obstructed.

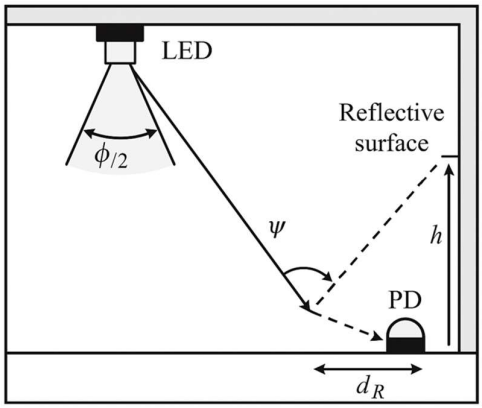

Figure 3.5 Non-Directed Line-of-Sight (NLOS) Transmission Model (22).

In NLOS systems, the transmitter emits light in a diffuse manner, often modeled by a Lambertian radiation profile, and the receiver collects only a portion of the reflected or scattered optical power. This results in a significant reduction in received signal strength, increased delay spread, and greater sensitivity to multipath distortion. Consequently, the NLOS model generally suffers from lower signal-to-noise ratios (SNR) and narrower bandwidths than its DLOS counterpart.

The DC gain of the NLOS link can be described using the integral form:

$$H_{NLOS}(0) = \iint_{wall} \frac{\rho_s A_{Rx} R_0(\phi) \cos(\phi) \cos(\psi)}{\pi d_1^2 d_2^2} dA \tag{3.11}$$

where ρ_s is the reflectivity of the reflecting surface, A_{rx} is the physical area of the photodetector, $R_0(\phi)$ is the radiant intensity of the LED, ϕ and ψ are the angles of incidence and reflection, $d_1$is the distance from transmitter to the reflecting point, d_2 is the distance from the reflecting point to the receiver, and the integration occurs over the reflective surface area.

This formulation indicates that the received power is heavily influenced by surface reflectivity (ρ_s), angle of incidence/reflection, path lengths, and the Lambertian emission characteristics of the LED.

The received optical power in the NLOS model is then given by:

$$P_{Rx} = H_{NLOS}(0).P_{Tx} \tag{3.12}$$

The corresponding channel impulse response, incorporating the delay induced by longer optical paths, is expressed as:

$$h_{NLOS}(t) = H_{NLOS}(0).\delta\left(t - \frac{d_1 + d_2}{c}\right) \tag{3.13}$$

where $\delta(t)$ is the Dirac delta function, and c is the speed of light in free space.

Due to the increased propagation delay and multipath components, NLOS channels require advanced equalization and signal processing techniques to maintain link quality. Nevertheless, their inherent flexibility, lack of alignment constraints, and wider coverage area make them a practical solution in cluttered or mobile environments where precise alignment is not feasible.

3.3 LED Thermal Management

Thermal management is a critical aspect of LED-based optical wireless communication (OWC) systems, particularly in scenarios where high optical power, narrow beam divergence, and continuous operation are required. LEDs are inherently temperature-sensitive devices; their performance characteristics—including output power, wavelength stability, lifetime, and efficiency—can degrade significantly under elevated junction temperatures. Therefore, proper thermal control is essential not only for maintaining system performance but also for ensuring device longevity and reliability.

3.3.1 Impact of Temperature on LED Performance

As junction temperature increases, several undesirable effects occur:

- Optical Output Power Degradation: The light output from an LED typically decreases with increasing temperature due to reduced radiative recombination efficiency.
- Wavelength Shift: Higher temperatures result in a redshift of the emission spectrum, which may impact on the spectral alignment with optical filters or photodetectors in wavelength-sensitive OWC systems.
- Increased Forward Voltage Drop: The forward voltage of the LED decreases with temperature, altering power consumption and affecting driver stability.
- Accelerated Aging and Reduced Lifetime: Prolonged exposure to high temperatures can lead to thermal degradation of the semiconductor junction and encapsulant materials, reducing LED lifespan.

These factors make thermal control indispensable, especially in embedded or enclosed environments such as in-pipe robotic systems or sealed sensor modules, where convective cooling is limited.

3.3.2 Thermal Resistance and Junction Temperature

The junction temperature T_j of an LED is governed by the following relationship:

$$T_j = T_a + \left(R_{\theta JA}.P_{th}\right) \tag{3.14}$$

where T_j is the junction temperature (°C), T_a is the ambient temperature (°C), $R_{\theta JA}$ is the junction-to-ambient thermal resistance (°C/W), P_{th} is the thermal power dissipated (W), which is typically the electrical input power minus the emitted optical power.

This equation highlights the importance of minimizing $R_{\theta JA}$ using efficient thermal interfaces, such as metal-core PCBs, thermal vias, and active heatsinks.

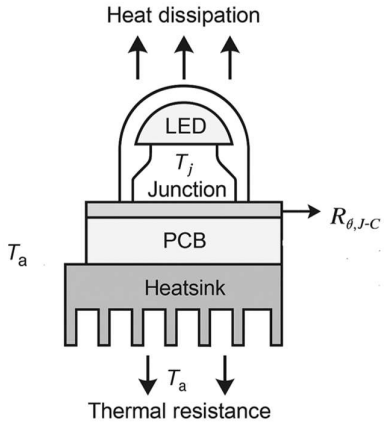

Figure 3.6 Thermal resistance and heat dissipation model of an LED package (24).

3.3.3 Heat Sink Design and Optimization

To effectively manage heat, LEDs in high-speed OWC systems are often mounted on aluminum or copper heat sinks, sometimes with finned geometries to increase surface area and improve natural or forced convection. The heat sink's design must balance:

- Thermal conductivity,
- Physical volume constraints (especially in robotic applications),
- Weight limitations, and
- Cost-effectiveness.

- Heatsink design with natural convection

Figure 3.7 presents the structural configuration of a finned heat sink, where the key geometrical parameters are identified as follows: L denotes the fin height, W is the base width, H represents the fin thickness, and S_{opt} indicates the optimal spacing between adjacent fins. These parameters are essential for determining the total number of fins (N) and the overall surface area available for heat dissipation.

The convective heat dissipation from the external fin surfaces (A_1), as shown in the diagram, is a critical factor in assessing the thermal performance of the heat sink. It can be estimated to be used by empirical thermal models. The initial heat transfer by convection, denoted Q_{c1}, is calculated based on the standard heat transfer equation:

$$Q_{c1} = 2h_1A_1(T_s - T_{amb}) \tag{3.15}$$

The variable T_s denotes the temperature of the heat source, while T_{amb} refers to the ambient air temperature. The surface area A_1, which contributes to convective heat transfer, can be determined using Equation (3.16).

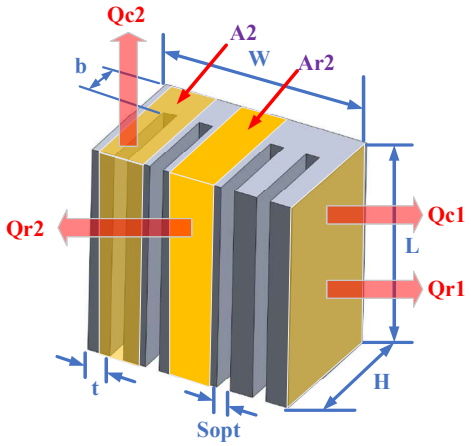

Figure 3.7 delineates the distinct areas used in the calculation of heat dissipation from the heat sink (25).

$$A_1 = HL + t(2H + L) \tag{3.16}$$

The convective heat transfer coefficient h_1 corresponding to the area A_1 is evaluated using Equation (3.17), which is specifically formulated for natural convection from vertical surfaces (25). Although A_1 encompasses some minor horizontal surfaces, their contribution to total heat dissipation is negligible when compared to the dominant effect of the vertical fin surfaces, which are primarily responsible for natural convective cooling.

$$h_1 = 1.42\left[\frac{T_s - T_{amb}}{H}\right]^{1/4} \tag{3.17}$$

The heat dissipated by natural convection, denoted as Q_{c2}, from the fin surface area A_2, can be determined using Equation (3.18).

$$Q_{c2} = h_2 A_2 (T_s - T_{amb}) \tag{3.18}$$

The area A_2 is obtained from equation (3.19).

$$A_2 = L\big[2(H - b) + S_{opt}\big] + 2\big(tH + S_{opt}b\big) + tL \tag{3.19}$$

Equation (3.20) defines the optimal fin spacing S_{opt}, which maximizes natural convective heat transfer between the fins. This expression is derived by optimizing the product of the internal fin surface area and the convective heat transfer coefficient, ensuring maximum thermal dissipation under natural convection conditions (26).

$$S_{opt} = 2.71 \left[\frac{g\beta(T_s - T_{amb})}{L\alpha v}\right]^{-1/4} \tag{3.20}$$

The convective heat transfer coefficient between adjacent fins is given by Equation (3.21), as proposed in Bar-Cohen and Rohsenow's model (26). In this equation, g represents the acceleration due to gravity, β is the thermal expansion coefficient with units in Kelvin, defined as $\beta = 1/T_{avg}$, α denotes the thermal diffusivity of air evaluated at the average temperature T_{avg}, v is the kinematic viscosity of air also evaluated at T_{avg}, and k represents the thermal conductivity of air at the same reference temperature. The average temperature is computed as:

$$T_{avg} = \frac{(T_s - T_{amb})}{2} \tag{3.21}$$

The contribution of radiative heat dissipation can be substantial in natural convection-cooled heat sinks and should therefore be included in the thermal design and sizing calculations of the heat sink. The radiative heat transfer from the surface area A_1, denoted as Q_{r1}, can be calculated using Equation (3.22).

$$Q_{r1} = 2\varepsilon\sigma A_1 (T_s^4 - T_{amb}^4) \tag{3.22}$$

In this context, the variable ε denotes the surface emissivity of the heat sink, while the Stefan–Boltzmann constant σ has a fixed value of 5.67×10^{-8} W/m^{2}K^4. Radiative heat transfer from the surface area A_2 is calculated using Equation (3.23). The corresponding effective radiative area A_{r2} is determined from Equation (3.24).

$$Q_{r2} = \varepsilon\sigma A_{r2} (T_s^4 - T_{amb}^4) \tag{3.23}$$

$$A_{r2} = L\big(t + S_{opt}\big) + 2\big(tH + S_{opt}b\big) \tag{3.24}$$

The number of fins N required to dissipate heat at a specified surface temperature T_s can be determined based on the principle of energy conservation. Under steady-state conditions, the total heat generated by the source (Q) must be equal to the total heat dissipated by the heat sink through a combination of convection and radiation. This thermal balance is mathematically expressed by Equation (3.25).

Furthermore, using this relationship, the appropriate fin width W can also be derived, as shown in Equation (3.26). These expressions are essential for the thermal and geometric optimization of fin heat sinks, particularly in passively cooled electronic systems such as LED-based OWC modules (26).

$$N = \left[1 + \frac{Q - Q_{r2} - Q_{c2}}{Q_{r1} - Q_{c1}}\right] \tag{3.25}$$

$$W = (N - 1)S_{opt} + Nt \tag{3.26}$$

This section underscores the vital importance of thermal management in maintaining the performance, efficiency, and longevity of LED-based optical wireless communication (OWC) systems. Excessive junction temperatures can lead to reduced optical output, spectral shift, and accelerated degradation of LED materials. To mitigate these effects, the section introduces the concept of thermal resistance, emphasizing the role of minimizing the overall junction-to-ambient thermal resistance $R_{\theta JA}$.

The design and optimization of finned heat sinks are explored as the primary means of passive cooling, with attention given to key geometric parameters such as fin height, spacing, width, and surface area. Analytical expressions for convection and radiation heat dissipation are provided, including methods to calculate optimal fin spacing and convection coefficients, based on natural convection principles and temperature-dependent air properties.

To further enhance heat dissipation, especially in high-power or confined environments, advanced cooling solutions are discussed. These include microporous copper foams, heat pipes, and active cooling mechanisms such as miniature fans or thermoelectric coolers (TECs). These technologies help improve thermal regulation where passive methods are insufficient.

3.4 OWC Channel Modelling

Optical Wireless Communication (OWC) systems rely heavily on accurate channel modelling to predict signal behavior and system performance in different propagation environments. In applications such as in-pipe communication or underwater channels, light propagation is influenced by absorption, scattering, and medium inhomogeneity. This chapter provides a comprehensive discussion on two essential models for OWC channel characterization: the Beer–Lambert Law and the Channel Impulse Response (CIR).

3.4.1 Beer–Lambert Law

The Beer–Lambert Law is a foundational model used to describe the exponential attenuation of optical power as light travels through an absorbing and/or scattering medium. This model is particularly relevant for underwater or water-filled

pipe environments, where medium-induced attenuation significantly affects communication performance. The Beer–Lambert Law is mathematically expressed as:

$$P(d) = P_0 . e^{-\alpha d} \tag{3.27}$$

where P_0 is the transmitted optical power, $P(d)$ is the received power after travelling a distance d, α is the attenuation coefficient (in m^{-1}), incorporating both absorption (a) and scattering (b): $\alpha = a + b$.

This exponential decay model assumes a collimated beam and a homogenous medium, making it especially applicable for in-pipe environments with known materials such as water-filled or air-filled PVC pipes. The attenuation coefficient varies with wavelength and medium properties; for example, shorter visible wavelengths generally exhibit lower absorption in pure water but higher scattering.

The Beer–Lambert Law is essential in calculating link budgets and signal power decay, especially in stratified or turbid media. Its simplicity makes it widely adapted in both theoretical and practical modelling of underwater or intra-pipe optical channels (22).

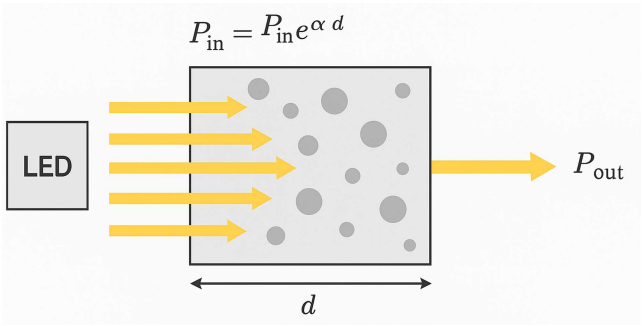

Figure 3.8 Illustration of the Beer–Lambert Law in an optical wireless communication channel (16).

Figure 3.8 Illustration of the Beer–Lambert Law in an optical wireless communication channel. This diagram shows a beam of light emitted by an optical transmitter (e.g., LED) propagating through a medium such as water or air over a distance d. As the light travels, it undergoes attenuation due to absorption and scattering.

3.4.2 Channel Impulse Response (CIR)

The Channel Impulse Response (CIR) is a fundamental metric that describes how an optical channel modifies an input pulse over time due to multiple propagation paths and delays. In directed or non-directed optical wireless channels, CIR plays a central role in evaluating inter-symbol interference (ISI), time dispersion, and channel bandwidth.

The CIR *h(t)* can be derived using Monte Carlo ray-tracing or analytical models that simulate photon travel through scattering media. A typical expression for CIR in a Line-of-Sight (LOS) or underwater medium is:

$$h(t) = \sum_i \delta(t - \tau_i).a_i \tag{3.28}$$

where $\delta(\cdot)$ is the Dirac delta function, τ_i is the delay of the i-th path, a_i is the corresponding path attenuation due to absorption and scattering. In a scattering-dominant channel (e.g., water with suspended particles), light is diffused and delayed, resulting in a broader CIR and lower peak intensity. The CIR is highly dependent on system parameters such as LED divergence, photodetector field of view (FOV), and medium refractive index. For example, narrow-beam LEDs in clear water produce short-delay and high-SNR CIRs, while wide-beam LEDs in turbid water led to elongated CIRs with reduced clarity.

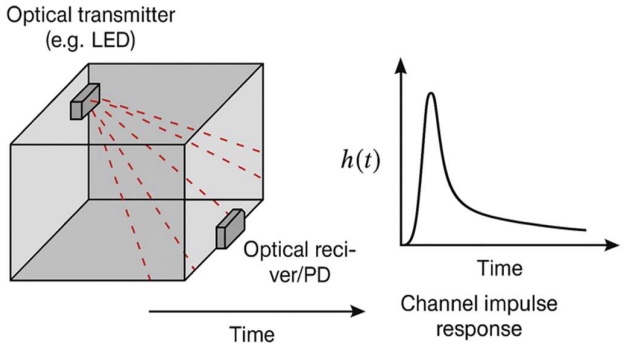

Figure 3.9 The channel impulse response (CIR) diagram (3).

Figure 3.9 illustration of the Channel Impulse Response (CIR) in an optical wireless communication system. This diagram depicts the temporal behavior of a transmitted optical pulse as it propagates through a scattering and reflecting medium, such as water or an in-pipe environment. The top portion of the figure shows an ideal short pulse (e.g., a delta function) emitted by the optical transmitter. Through pulse travels through the channel, it experiences multipath propagation due to scattering, reflection, and refraction, resulting in a spread-out waveform at the receiver.

The bottom portion illustrates the corresponding CIR, *h(t)*, which quantifies how the received signal is distributed in time. The CIR typically features a main peak corresponding to the direct path and a series of delayed components with reduced amplitude, caused by indirect paths. These delayed paths introduce inter-symbol interference (ISI) in digital communication systems, especially in wide-beam or turbid media. The shape and width of the CIR are critical for assessing system bandwidth, equalization requirements, and overall data integrity in OWC environments.

Simulation tools (e.g., MATLAB, Python, Zemax) or numerical photo-based models can be used to compute CIRs for various conditions. These CIR models are then used in convolution with the transmitted data to predict received signals and estimate bit error rate (BER) performance under different modulation schemes. Accurate CIR modelling enables system designers to select suitable modulation formats, optimize LED and photodetector alignment, and determine the required equalization or filtering strategies (27).

3.4.3 Scattering Phase Function

In optical wireless communication, especially in underwater or in-pipe environments, scattering plays a critical role in signal degradation. To accurately characterize scattering behavior, the scattering phase function is used. This function describes the angular distribution of scattered light intensity as a function of the scattering angle.

- Mie Scattering

Mie scattering theory is applied when the scattering particles are of comparable size to the wavelength of the incident light. This is typically the case in underwater environments, where suspended particles such as plankton and sediments influence light propagation.

Mie theory accounts for the complex angular distribution of scattered light and is computationally intensive. The scattering phase function derived from Mie theory is strongly forward directed, meaning most of the scattered light remains near the incident direction. This anisotropic scattering behavior impacts both the spatial and temporal characteristics of the channel.

- Henyey-Greenstein Phase Function

To simplify the modeling of anisotropic scattering, the Henyey-Greenstein (HG) phase function is often used (16). It approximates the angular scattering distribution with a single parameter , known as the asymmetry factor, which ranges from -1 to 1:

$$P(\theta) = \frac{1 - g^2}{\left(1 + g^2 - 2g\cos\theta\right)^{3/2}} \tag{3.29}$$

Where $P(\theta)$ is the probability density function of scattering at angle, and g is the asymmetry parameter, where $g=0$ represents isotropic scattering, $g>0$ indicates forward scattering, and $g<0$ indicates backwards scattering.

The HG function provides a convenient and effective approximation of the Mie phase function, especially for Monte Carlo simulations and analytical modeling. Its flexibility and mathematical simplicity make it a preferred tool in the study of scattering behavior in OWC systems.

3.4.4 Channel Frequency Response (CFR)

The Channel Frequency Response (CFR) describes how different frequency components of an optical signal are affected by the communication channel. It is the Fourier Transform of the Channel Impulse Response (CIR) and provides crucial insight into the channel's bandwidth and frequency-dependent attenuation characteristics (28). Mathematically, the CFR is expressed as:

$$H(f) = \int_{-\infty}^{\infty} h(t).e^{-j2\pi ft} dt \tag{3.30}$$

where *H(f)* is the channel frequency response at frequency, and *h(t)* is the channel impulse response, *f* represents the frequency (Hz).

CFR is essential for understanding how the channel behaves in the frequency domain. It allows system designers to determine:

- Bandwidth limitations, i.e., the frequency range over which the signal can pass with minimal distortion
- Notch frequencies, where deep attenuation occurs due to multipath interference
- System capacity, by evaluating how much usable spectral content remains after channel distortion

In optical wireless systems, particularly underwater or in-pipe environments, the CFR can be significantly affected by scattering, absorption, and boundary reflections. The shape of the CFR can vary with different modulation schemes, LED spectral characteristics, and photodetector responses. A flat CFR indicates that the channel supports all frequency components equally, whereas a decaying CFR suggests low-pass characteristics typical in diffusion-dominated environments.

3.5 Modulation Techniques for OWC

Modulation techniques play a critical role in determining the performance, spectral efficiency, and robustness of Optical Wireless Communication (OWC) systems. The choice of modulation is influenced by factors such as channel conditions, transmission power, data rate requirements, and the characteristics of optical sources and detectors. In OWC, modulation can be broadly categorized into intensity modulation with direct detection (IM/DD) and coherent modulation, with IM/DD being most commonly used due to its simplicity and compatibility with photo detectors.

3.5.1 On-Off Keying (OOK)

OOK is the simplest and most widely used modulation technique in OWC. It represents digital data with the presence or absence of lightly using LEDs or laser diodes as the transmitter. A logical '1' corresponds to a light pulse, while a '0'

corresponds to no light. OOK is energy-efficient and easy to implement, but it is sensitive to background noise and ambient light interference.

3.5.2 Pulse Position Modulation (PPM)

PPM improves upon OOK by encoding data in the position of a single pulse within a predefined time slot. It provides better power efficiency and robustness in low-light conditions. However, it requires higher synchronization accuracy and may suffer from lower spectral efficiency.

3.5.3 Pulse Amplitude Modulation (PAM)

PAM transmits data by varying the amplitude of the optical pulses. It allows for multiple amplitude levels, enabling higher data rates compared to OOK. However, PAM is more susceptible to amplitude distortion and requires more sophisticated receivers to distinguish between different levels.

3.5.4 Orthogonal Frequency Division Multiplexing (OFDM)

OFDM is a multicarrier modulation technique that divides the data stream into multiple parallel sub-streams, each modulated onto a separate carrier frequency. Optical OFDM provides high spectral efficiency and resilience to multipath distortion, making it suitable for high-speed OWC systems. Nonetheless, it requires complex transceiver design and may have high peak-to-average power ratios.

Chapter 4

Experimental Characterization of Optical Wireless Communication in an Empty Pipe (Free-Space) Environment

4.1 Introduction

Optical Wireless Communication (OWC) systems deployed in confined environments such as pipelines require thorough characterization to evaluate signal behavior across different propagation scenarios. A fundamental aspect of this evaluation involves studying the OWC channel within an empty pipe, where air serves as the transmission medium. This condition closely resembles a free-space environment and provides a crucial baseline for comparison with more complex media, such as water-filled or turbid conditions. By establishing this reference, subsequent analyses can more accurately assess the performance degradation or enhancement caused by medium-induced absorption and scattering.

In the absence of absorptive or scattering materials, the transmission primarily exhibits line-of-sight (LOS) and non-line-of-sight (NLOS) characteristics, with minimal attenuation. However, the cylindrical geometry of the pipe introduces boundary reflections that can lead to multipath propagation and potential signal distortion. This section focuses on examining the effects of such geometrical constraints on the received signal strength, frequency response, and overall signal attenuation. A particular emphasis is placed on evaluating the bandwidth behavior of monochromatic LEDs under various conditions, highlighting their suitability for high-speed OWC applications.

The experimental setup comprises a 350 mm and 1,000 mm long PVC pipe, within which a five-wavelength LED transmitter is installed. To investigate the enhancement of optical power, additional optical components such as reflectors and lenses are employed. A Thorlabs PDA10A2 photodiode is positioned coaxially at the receiving end to capture the transmitted signals. Measurements are taken across a range of LED bias currents and alignment configurations, enabling the analysis of key parameters such as received optical power and frequency-dependent behavior. The findings from this study contribute to foundational insights necessary for modeling and optimizing OWC systems, particularly when transitioning to more attenuative environments like water or mixed media.

This chapter addresses Research Questions 1 and 4, which investigate how the optical and material properties of PVC and stratified water layers affect light propagation within confined in-pipe environments, and which LED wavelength and optical configuration yield optimal performance. The chapter presents a series of simulations and experimental validations performed using Ansys Zemax OpticStudio to analyze wavelength-dependent reflection, scattering, and transmission. It also evaluates the performance impact of optical enhancements such as reflectors and lenses across multiple LED wavelengths.

By correlating simulation results with experimental measurements, this chapter quantifies how different optical designs influence received signal strength and beam uniformity, providing critical insight into wavelength selection and component optimization for efficient in-pipe optical wireless communication (OWC).

4.2 In-pipe environment simulation and experimental Setup

The simulation work was performed using Ansys Zemax OpticStudio (Non-Sequential Mode), incorporating manufacturer-supplied LED ray files (OSRAM) to accurately model the optical emission profiles. The PVC pipe geometry—with an inner diameter of 50 mm and lengths of 350 mm and 1,000 mm—was constructed within the optical model. Surface scattering was characterized using the tabular BSDF data, which replicates diffuse reflection from the pipe walls. Simulations were carried out for five wavelengths—410 nm, 475 nm, 528 nm, 583 nm, and 625 nm—to evaluate wavelength-dependent propagation behavior and its effect on system performance.

Figure 4.1 illustrates the experimental setup designed to evaluate the alternating current (AC) response of the Optical Wireless Communication (OWC) system within an air-filled (free space) pipe environment. The setup integrates both electronic and optoelectronic subsystems to analyze the modulation and transmission characteristics of high-power LEDs over a wide frequency range.

At the core of the system, a Python-based control program interfaces with a Keysight E8257D signal generator via an Ethernet connection using the TCP Modbus protocol. The generator produces a continuous-wave RF signal from 250 kHz to 30 MHz at a constant +10 dBm output power, which is capacitively coupled with a DC bias supplied from a regulated power source (Appendix B.2). The coupling network consists of a 1 nF RF capacitor (ATC Kyocera AVX 700B102FT50XT, ±1% tolerance) in series with a 1.2 Ω resistor, ensuring impedance matching, preventing DC backflow to the signal generator, and maintaining signal integrity. The combined AC–DC drive enables LED modulation under realistic bias conditions suitable for high-speed optical communication analysis.

For optical transmission, an optical lens is used to collimate the LED's divergent beam before it propagates through a 350 mm PVC pipe. An optical reflector is positioned at the transmitter end to enhance forward-directed optical power and improve received signal strength. To assess long-distance propagation effects, the pipe length is extended to 1,000 mm in selected trials.

At the receiver, a Si-amplified photodetector (Thorlabs PDA10A2) equipped with an internal Thorlabs FDS010 photodiode captures the transmitted optical signal. The detector, with a spectral sensitivity range of 200–1,100 nm, is well-suited for visible and near-infrared measurements. Its output is fed into an Agilent CXA N9000A signal analyzer, which digitizes and processes the received waveform. All measured signals are logged and visualized in Python, providing real-time plots and data export for further post-processing.

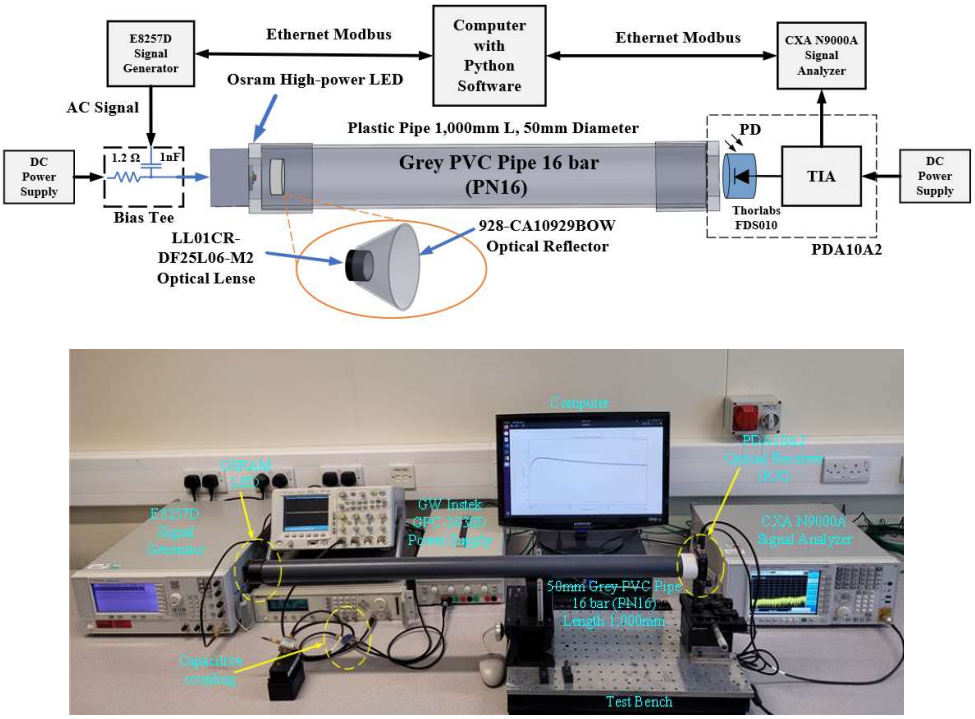

Figure 4.1 The experimental setup employed for empty pipe characterization measurements in this study.

Table 4-1 Specifications of optical devices used in the in-pipe frequency response measurements

LED color	LED wavelength (nm)	Part number
Red	625	720-LJCKBPJZKZ251
Green	528	720-LTCQBPKYLYA3581
Yellow	583	720-GYCSHPM123A0763
Purple	410	897-LZ1-00UB0R-00U4
Blue	475	720-LBCRBPA6186
Optical devices	**Viewing Angle (degree)**	**Part number**
Lens	25	LL01CR-DF25L06-M2
Reflector	54	Ledil, CA10929

During testing, a noticeable drop in received power between 0 and 2 MHz was observed. This behavior is attributed to the capacitive reactance of the 1 nF

coupling capacitor, which attenuates low-frequency components—an important factor in defining the system's lower frequency response limit.

Table 4-1 lists the main optical components used in the setup, including the specifications of LEDs, lenses, and reflectors. This rigorous configuration ensures accurate AC characterization and provides a reliable foundation for optimizing OWC system performance in confined, free-space pipeline environments.

4.3 Simulation In-pipe frequency response and scattering

4.3.1 LED Frequency response simulation.

This section provides an in-depth analysis of the frequency response behavior of light-emitting diodes (LEDs) simulated across five discrete wavelengths using advanced circuit modeling techniques. The electrical characteristics of each LED are represented using an equivalent circuit model consisting of a series resistor (RS) and an inductor (L), configured in parallel with a junction composed of a diode (D) and a diffusion plus junction capacitance component (CD). This widely accepted modeling approach is consistent with the method reported by O'Brien et al. and effectively captures both the static and dynamic behavior of LEDs under modulation.

To ensure accurate simulation fidelity, the study utilizes the manufacturer-supplied SPICE model of the OSRAM LED series. This model has been imported and configured within the Keysight Advanced Design System (ADS); a professional-grade electronic design automation (EDA) tool used for RF, microwave, and high-speed digital applications. Figure 4.2 illustrates the complete simulation topology as implemented in Keysight ADS, including the biasing network, termination loads, and measurement probes.

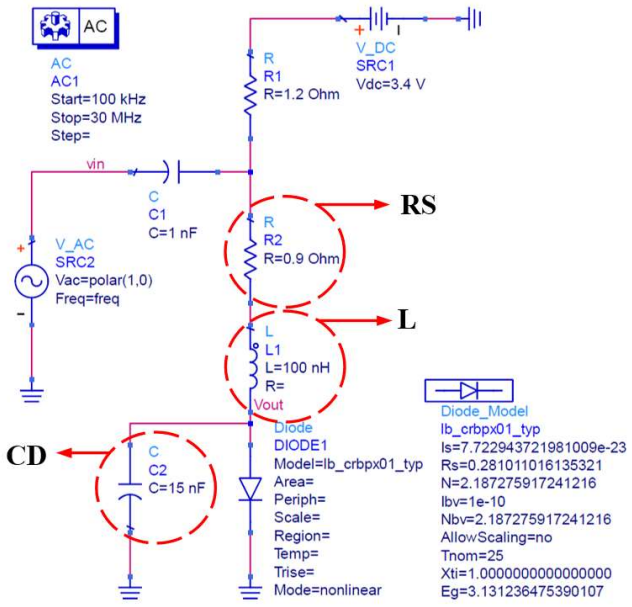

Figure 4.2 A schematic diagram of the OSRAM LED characteristics using the Keysight ADS software.

The integration of the SPICE model within Keysight ADS allows for precise simulation of the LED's modulation response under variable operating frequencies and bias conditions. This setup facilitates detailed extraction of key parameters such as 3 dB bandwidth, impedance response, and transient behavior. The results obtained from this simulation provide critical insights into how LED structure and internal parasitic components affect frequency performance across different emission wavelengths. These findings support the optimal selection of LED types for high-speed optical wireless communication (OWC) applications, particularly in bandwidth-constrained or noise-sensitive environments.

During the simulation phase, the electrical parameters specified in the SPICE model for the OSRAM LEDs were rigorously applied to accurately replicate the real-world behavior of each device. The simulation setup involved injecting a sinusoidal input signal with a power level of 10 dBm through a 1 nF high frequency coupling capacitor, thereby mimicking high-speed modulation conditions. Concurrently, each LED was forward biased with a constant current of 350 mA to simulate its typical operational regime in optical wireless communication (OWC) systems.

To ensure color-specific accuracy, key circuit components—particularly the inductance (L) and the parallel capacitance (CD)were meticulously tuned for each LED based on its emission wavelength. These adjustments are critical due to the intrinsic differences in junction capacitance, charge storage behavior, and carrier dynamics that arise from variations in LED material composition across the visible spectrum. Such color-specific tuning enables a more accurate modeling of the frequency-dependent electrical response of each LED.

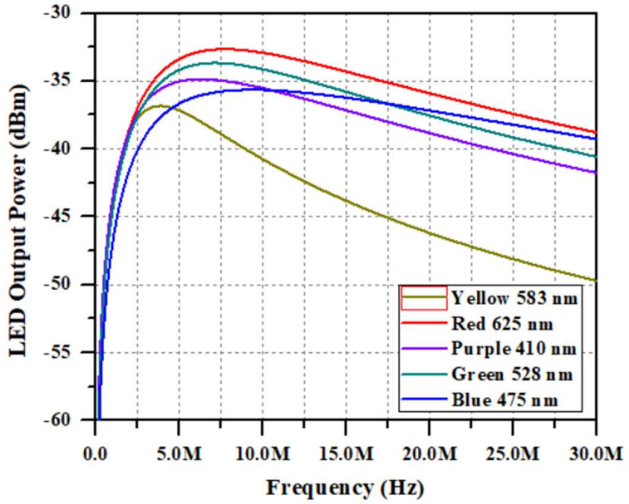

Figure 4.3 the simulation results of the LED's frequency response using Keysight ADS software.

The simulation was conducted using the Keysight Advanced Design System (ADS), a high-performance RF and optoelectronic circuit simulation platform. The model topology includes a combination of series and parallel passive components

arranged to emulate the high-frequency small-signal behavior of the LED under test. The simulation results, summarized in Table 4-2 and graphically illustrated in Figure 4.3, reveal key performance metrics such as the output signal strength in dBm and the 3 dB modulation bandwidth for each wavelength.

Table 4-2 the parasitic value of HB-LED at each wavelength with a bias current of 350 mA

LED wavelength (nm)	Inductor (L) (nH)	Capacitor (C) (nF)
625	100	16
528	100	20
583	150	40
410	150	15
475	100	10

Specifically, the red LED exhibited a signal strength of –32.65 dBm and a 3 dB bandwidth of 16.1 MHz, while the green LED measured –33.66 dBm with a bandwidth of 14.4 MHz. The yellow LED demonstrated a narrower bandwidth of 7 MHz and signal strength of –36.82 dBm, indicating a limited high-frequency performance. In contrast, the purple LED (410 nm) showed –34.86 dBm with a bandwidth of 14.8 MHz, and the blue LED (475 nm) delivered the highest bandwidth at 23.8 MHz, with an output of –35.64 dBm.

These findings emphasize the importance of wavelength-dependent circuit optimization in LED-based transmitters. The clear variation in bandwidth and signal output across the LED spectrum highlights the role of component tuning in maximizing modulation efficiency and system throughput for OWC applications. By leveraging the flexibility of SPICE modeling in a robust simulation environment, the study establishes a strong foundation for selecting and optimizing LEDs for specific spectral and bandwidth requirements in high-speed optical communication systems.

4.3.2 Simulation results of the in-pipe characteristics.

This section focuses on modeling optical behavior within a confined pipeline environment, using parameters derived from LED frequency response simulations conducted in Keysight Advanced Design System (ADS). The primary objective is to evaluate and simulate the propagation and modulation characteristics of optical signals transmitted through the pipe across multiple LED wavelengths. To achieve this, comprehensive optical simulations were performed using Ansys Zemax OpticStudio, a ray-tracing software platform widely recognized for advanced optical system analysis.

The simulation framework incorporates detailed models of five monochromatic LEDs—spanning wavelengths of 410 nm (purple), 475 nm (blue),

528 nm (green), 583 nm (yellow), and 625 nm (red)—together with optical accessories such as reflectors and collimating lenses. These components were integrated to enhance coupling efficiency, increase beam directivity, and improve the uniformity of light propagation within the pipe. The influence of these accessories on the system's frequency response and bandwidth was evaluated across all wavelengths.

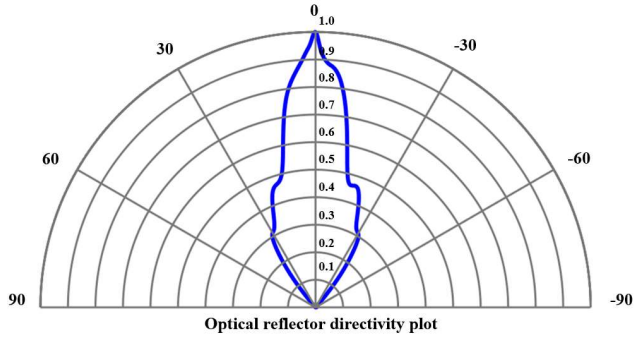

Figure 4.4 The optical reflector directivity results of the simulation using Ansys Zemax Optics Studio software.

To ensure accuracy, the LED–reflector assembly was modeled using manufacturer-provided ray files from OSRAM, which describe the angular emission and luminous intensity characteristics of each LED under various operating conditions. The reflectors were designed based on the manufacturer's specifications and constructed from metallized polycarbonate (PC), a material chosen for its high reflectivity and low optical loss due to scattering or absorption.

Figure 4.4 presents the results of the optical ray-tracing simulation conducted in Ansys Zemax OpticStudio, illustrating the integration of an LED with a precision-engineered optical reflector. The simulation accurately reproduces the reflector's angular emission profile, yielding a directivity angle of approximately 55°, which closely matches the 54° specified in the manufacturer's datasheet. This strong correlation validates the reliability of the optical model and confirms the reflector's effectiveness in shaping and enhancing the LED's emission characteristics within the pipeline environment.

Building upon these findings, a secondary simulation was performed to analyze the interaction between the LED and an optical lens. The lens was modeled in Ansys Zemax OpticStudio using the manufacturer's dimensional and optical parameters, including key material properties such as the refractive index and transmission characteristics of polymethyl methacrylate (PMMA).

Figure 4.5 presents the simulated optical behavior of the LED–lens assembly. The results depict the angular intensity distribution of the collimated light beam, showing a viewing angle of approximately 25.18°, which aligns closely with the 25° directivity angle specified by the manufacturer. This close agreement further demonstrates the precision of the optical modeling approach and confirms the lens's

capability to effectively collimate and steer the emitted light in accordance with its design specifications.

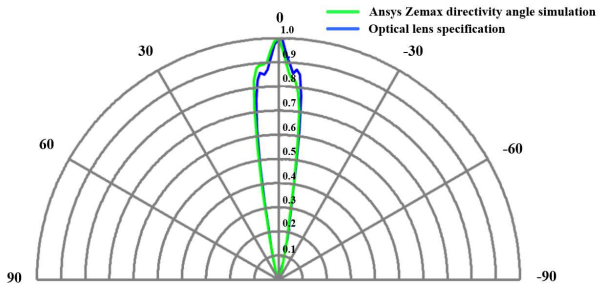

Figure 4.5 the optical lens directivity results of the simulation using Ansys Zemax Optics Studio software.

The development of the optical reflector and lens components followed rigorous modeling procedures that adhered strictly to dimensional and material specifications outlined in the manufacturer's documentation. These optical components were subsequently integrated into a simulated in-pipe Optical Wireless Communication (OWC) environment. The pipe used in the simulation was defined as a standard inner diameter of 50 mm and a length of 350 mm to reflect realistic deployment conditions. To ensure alignment between the simulation and actual experimental setups, the detector size was configured to match the active area of the Thorlabs PDA10A2 photodetector, which features a sensing area of 0.8 mm².

Accurate modeling of material properties is crucial when simulating optical interactions with internal surfaces of the pipe. In this context, the inner surface of the PVC pipe was characterized by using a refractive index value of approximately 1.5514, as reported in literature (29). This parameter plays a pivotal role in determining how light reflects and refracts within the confined geometry of the pipe, influencing both direct and scattered optical paths. The precise representation of this refractive index enables realistic simulation outcomes, supporting the validity of the optical power propagation models and enhancing the fidelity of the system performance analysis under controlled conditions.

To accurately model the scattering behavior of light within the pipe environment, a Lambertian scattering model is employed. This model assumes that incident light is diffusely reflected in all directions, which is characteristic of surfaces with matte or non-specular finishes, such as the interior of PVC pipes. By integrating the Lambertian model with the known refractive index of PVC (approximately 1.5514), the simulation achieves a realistic approximation of light interaction with pipe surfaces. This approach is essential for understanding light distribution and signal integrity in confined and multipath-prone optical wireless communication (OWC) channels.

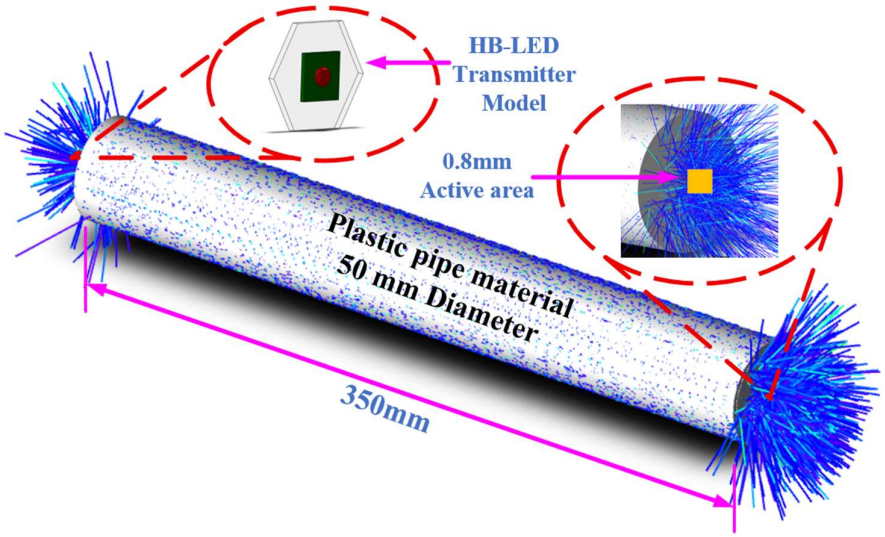

Figure 4.6 Simulation setups of the optical wireless communication system using the Zemax OpticStudio model.

Figures 4.6 illustrate both the simulation and experimental setups designed to investigate the propagation of optical beams under various configurations. The simulations, performed in Ansys Zemax OpticStudio, visualize how different optical components—such as lenses, apertures, and pipe materials—affect beam divergence, reflection, and scattering within the in-pipe environment.

The corresponding experimental setup replicates these configurations using the actual LED transmitter, photodiode receiver, and PVC pipe assembly to validate the simulation results. This side-by-side presentation provides a clear comparison between theoretical modeling and simulation optical behavior, ensuring that the figure communicates the relationship between the simulation parameters and the physical testing arrangement.

Figure 4.7 illustrates the spectral responsivity profile of the photodetector used in the experimental setup. This profile is essential for assessing detector sensitivity across different wavelengths and for calibrating simulation results against measured data. In the simulation, the output signal is calculated by integrating three key parameters: the optical power incident on the detector's rectangular active area, the wavelength-dependent responsivity of the photo detector, and the transimpedance gain of the optical receiver. For the Thorlabs PDA10A2 photodetector, this gain is approximately 5,000 V/A (PDA10A2, n.d.).

This integrated modeling approach provides a high-fidelity representation of the received electrical signal, effectively linking optical power transmission to electronic signal processing. Such detailed modeling is crucial for evaluating and optimizing the overall performance of the OWC system, particularly within confined and reflective environments such as PVC pipelines.

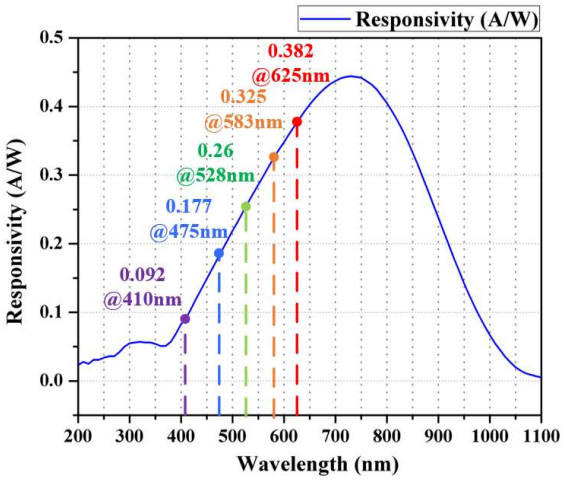

Figure 4.7 The responsivity of the optical receiver for each of the five wavelengths.

The simulation results in Figures 4.8 (a)–(e) collectively demonstrate the influence of optical enhancement components—reflectors and lenses—on the received signal strength across five LED wavelengths. Overall, the incorporation of these optical accessories substantially improves light-coupling efficiency and transmission performance within the 350 mm in-pipe OWC configuration.

Among all tested wavelengths, the red LED (625 nm) achieved the highest total gain of 20.26 dB, highlighting its superior compatibility with reflector- and lens-assisted configurations due to its lower intrinsic scattering losses. The blue LED (475 nm) followed with a combined improvement of 13.92 dB, while the yellow (583 nm) and green (528 nm) LEDs exhibited moderate gains of 12.44 dB and 10.53 dB, respectively. The purple LED (410 nm) recorded the lowest initial power and the smallest overall enhancement (10.82 dB), consistent with the higher absorption and scattering typically observed at shorter wavelengths.

These results confirm that integrating reflectors and lenses markedly enhances optical transmission efficiency by narrowing the beam divergence and concentrating emitted power toward the photodetector. Furthermore, the data indicates that longer wavelengths experience reduced attenuation and better propagation stability within the PVC pipe, establishing a clear correlation between wavelength selection and achievable signal performance. Collectively, the findings validate the optical modeling framework and demonstrate the importance of wavelength-specific optimization for effective in-pipe OWC system design.

This study investigates the modeling of LED optical behavior within a confined pipeline environment using Ansys Zemax OpticStudio simulations informed by electrical parameters derived from Keysight ADS. The analysis focuses on integrating high-power LEDs with optical reflectors made of metallized polycarbonate (PC) and lenses fabricated from polymethyl methacrylate (PMMA), emphasizing their roles in enhancing beam directivity and light focusing. The

simulation results confirm the validity of the optical models through strong agreement with manufacturer specifications.

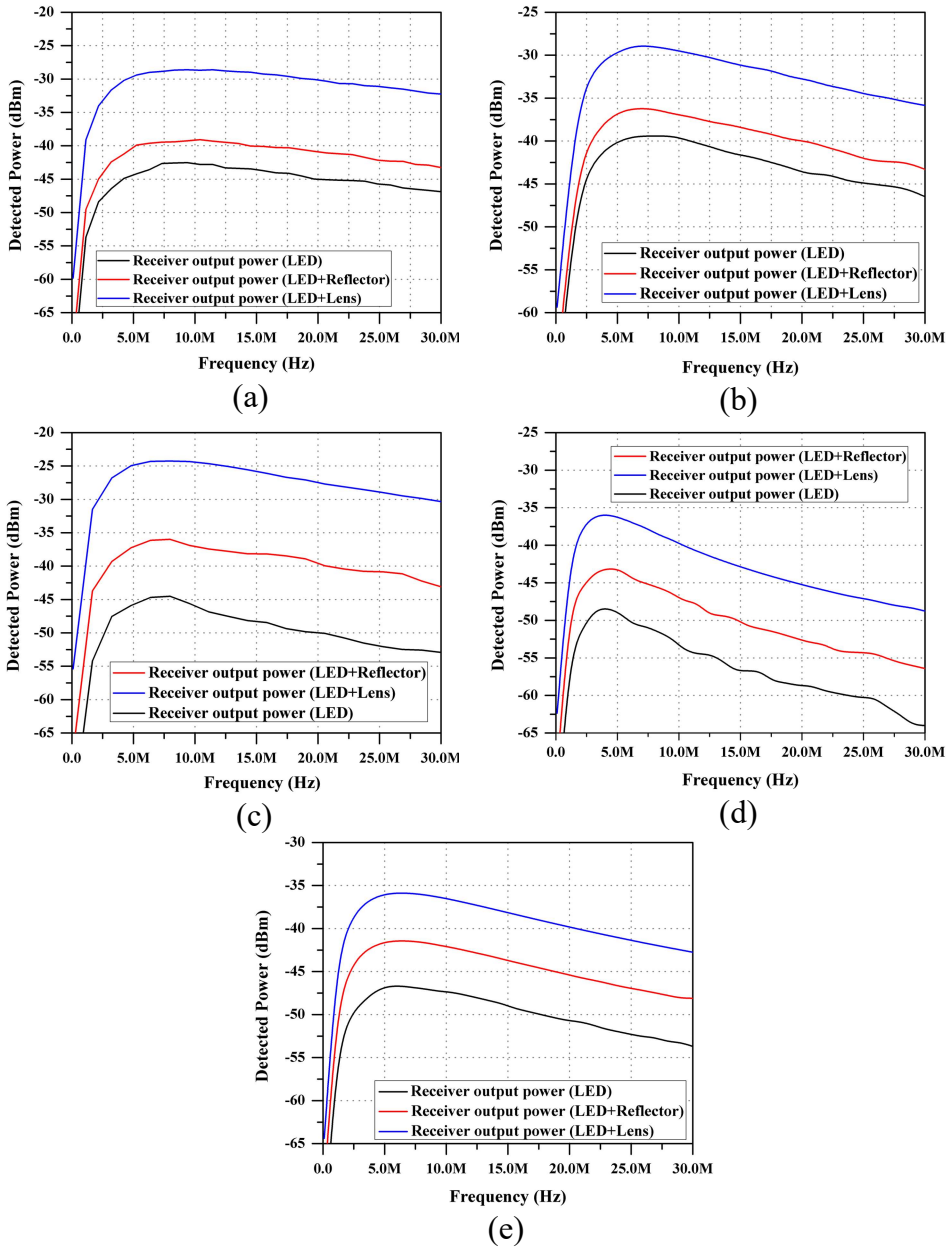

Figure 4.8 In-pipe frequency response simulation of the blue LED: (a) 475 nm, (b) 528 nm, (c) 625 nm, (d) 583 nm, (e) 410 nm.

The study further explores various optical configurations within the pipeline system to evaluate their influence on light propagation. As shown in Figures 4.8(a)–(e), the combined use of reflectors and lenses yields significant gains in received optical power across all tested wavelengths. These findings highlight the effectiveness of integrated optical designs in improving transmission efficiency within confined

and reflective environments such as pipelines. Overall, this work provides valuable insights into the optimal deployment of optical components for achieving high-performance optical wireless communication and sensing in enclosed or challenging propagation scenarios.

4.3.3 The index of refraction at a specific wavelength

This study centers on simulating the reflective characteristics of polyvinyl chloride (PVC) plastic pipes, a critical factor influencing light scattering within confined optical environments. The simulation seeks to determine the refractive index of PVC, a key optical property influenced by both the material composition and the wavelength of the incident LED light. The wavelength dependency arises from the spectral properties of the LED source, making it essential to evaluate how different wavelengths interact with the PVC surface. These simulation results are vital for understanding the optical behavior of PVC in systems where accurate control of light propagation is required.

To illustrate the relationship between LED wavelength and the refractive index of PVC, the results are presented through a dispersion diagram. This graphical representation elucidates how the refractive index changes across various wavelengths, offering valuable insights for optimizing optical system design involving PVC components. Furthermore, the study acknowledges the relationship between refractive index and attenuation, governed by the complex refractive index—a concept used to describe light behavior in absorbing media. This comprehensive approach supports the development of more efficient and precisely tuned optical communication and sensing systems within PVC-based structures.

A comparative analysis between the refractive index values obtained from Ansys Zemax OpticStudio simulations and those sourced from a standard refractive index database reveals strong agreement, confirming the accuracy of the simulated optical model (29). The propagation of light within absorbing media is governed by the complex refractive index, where the real component determines the phase velocity of light (refraction), and the imaginary component accounts for material absorption and attenuation losses (30).

Across the visible spectrum, the refractive index exhibits wavelength-dependent variation, typically fluctuating by a few percent due to dispersion effects. To quantify this behavior, Table 4-3 presents the refractive index and absorption coefficient values at five selected wavelengths. These results illustrate how the optical properties of the material evolve across the spectral range, providing essential insight for the accurate modeling of light–matter interactions and the design of high-precision optical systems.

Table 4-3 The refractive index and the absorption coefficient values

LED wavelength (nm)	PVC Refractive index	PVC Absorption coefficient (cm^{-1})
625	1.543	0.37196
528	1.546	0.46251
583	1.544	0.50179
410	1.556	0.73340
475	1.551	0.42064

The results presented in Table 4-3 demonstrate that the absorption coefficient of PVC material varies noticeably across different wavelengths. Specifically, the absorption coefficients were found to be 0.7334 at 410 nm, 0.4206 at 475 nm, 0.4625 at 528 nm, 0.5018 at 583 nm, and 0.3720 at 625 nm. These results clearly illustrate the wavelength-dependent absorption behavior of PVC, indicating that its ability to absorb optical energy changes significantly throughout the visible spectrum.

The relationship between the optical absorption coefficient and light attenuation is direct—higher absorption coefficients correspond to increased light attenuation due to stronger interactions between the propagating optical wave and the molecular structure of the material (31). This trend is evident in Table 4-3, where higher absorption at shorter wavelengths (e.g., 410 nm) results in greater attenuation compared with longer wavelengths (e.g., 625 nm). Such wavelength-dependent behavior underscores the importance of considering spectral dispersion when designing or modeling optical systems incorporating PVC materials.

The close agreement between the simulated results and theoretical expectations validates the accuracy and reliability of the optical model. This validation establishes confidence in the simulation tool's predictive capability and supports its application in the development and optimization of advanced optical systems for both experimental and engineering design purposes.

4.3.4 A partially reflective and partially scattering surface

This section explores the reflective properties of PVC plastic pipe surfaces through detailed simulation. Surface characteristics are defined using coating parameters derived from established refractive index databases, enabling accurate optical modeling. A rectangular volume is used in the simulation to represent a partially reflective surface, incorporating both diffuse and specular reflection components. Diffuse reflection is modeled using a Lambertian distribution, while the remaining portion of incident light is treated as specularly reflected. The simulation employs three non-sequential objects to analyze the complex interaction of light with the PVC surface under different reflection regimes. This approach offers a comprehensive assessment of how light behaves upon encountering coated PVC

surfaces. The resulting optical effects and reflection dynamics are visually summarized in Figure 4.9, providing valuable insights into the material's light interaction profile.

The simulation effectively captures both specular and diffuse reflection phenomena, contributing to a deeper understanding of light propagation through material interfaces. This modeling approach aligns with established optical theories, notably Fresnel's reflection theory (32), which describes light behavior at dielectric boundaries, and the Beer–Lambert Law (33), which governs the attenuation of light as it travels through absorbing media. By integrating these foundational principles, simulation provides a robust framework for analyzing optical interactions, thereby supporting advancements in material science and the design of efficient optical systems.

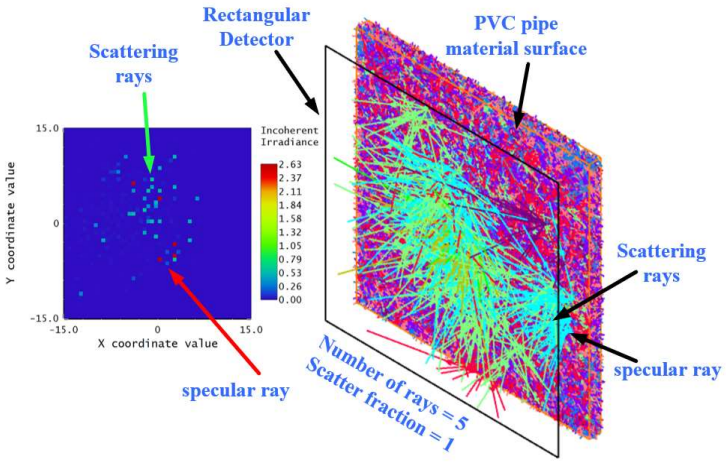

Figure 4.9 the reflective and scattering surface of PVC pipe (34).

In this investigation, Ansys Zemax OpticStudio was employed to simulate the interaction between light and the surface of PVC plastic pipes, characterized as both partially reflective and partially scattering. Simulation parameters were carefully calibrated, with the source ray power normalized to 1 W, a scatter fraction set to 1, and five rays utilized to effectively analyze scattering behaviors across multiple wavelengths. The primary metric of interest was the diffuse reflectance (R%), representing the proportion of incident light scattered by the PVC surface.

As shown in Figure 4.10, the diffuse reflectance values display a gradual, wavelength-dependent decrease—from 11.18% at 410 nm to 10.42% at 625 nm. Although this variation appears minor (a total difference of less than 1%), its significance lies in the cumulative effect over the propagation path. In short-pipe configurations, the impact of this variation on overall signal attenuation is negligible. However, as pipe length increases, even small differences in surface scattering become increasingly influential, leading to measurable reductions in received optical power and potential distortion of the beam profile. This relationship underscores the

importance of accurately accounting for wavelength-dependent scattering when modeling or designing long-distance in-pipe optical communication systems.

Furthermore, comparison with previously published reference data confirms the accuracy of the simulation model in reproducing the optical scattering characteristics of PVC (35). These findings reinforce that even subtle wavelength-specific changes in reflectance can accumulate significantly across extended optical paths, emphasizing the need for precise material characterization in large-scale or long-range OWC applications.

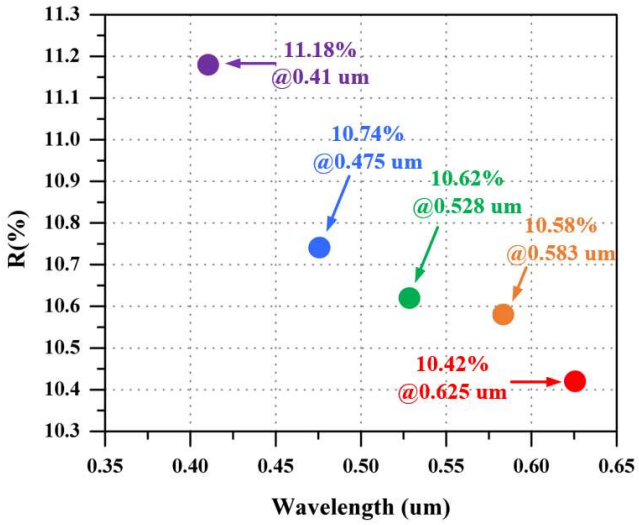

Figure 4.10 Diffuse reflectance spectra of the PVC material (34).

4.4 Measured In-pipe frequency response

4.4.1 Experimental results of the 350-mm pipe length

This section discusses the in-pipe frequency response of LEDs across five wavelengths (410–625 nm) in a 350 mm PVC conduit, highlighting how optical components—reflectors and lenses—affect received power and bandwidth. The results, summarized in Figure 4.11(a) to 4.11(e), show a consistent pattern across all wavelengths: received power decreases gradually with increasing frequency, reflecting frequency-dependent attenuation due to scattering and absorption losses within the pipe medium.

The measured frequency responses show a gradual reduction in received optical power with increasing modulation frequency for all wavelengths, indicating that the in-pipe optical channel exhibits frequency-dependent attenuation caused by scattering, absorption, and confinement losses within the PVC pipes. This attenuation becomes more pronounced at higher frequencies, where surface scattering and multipath dispersion increasingly degrade the detected signal.

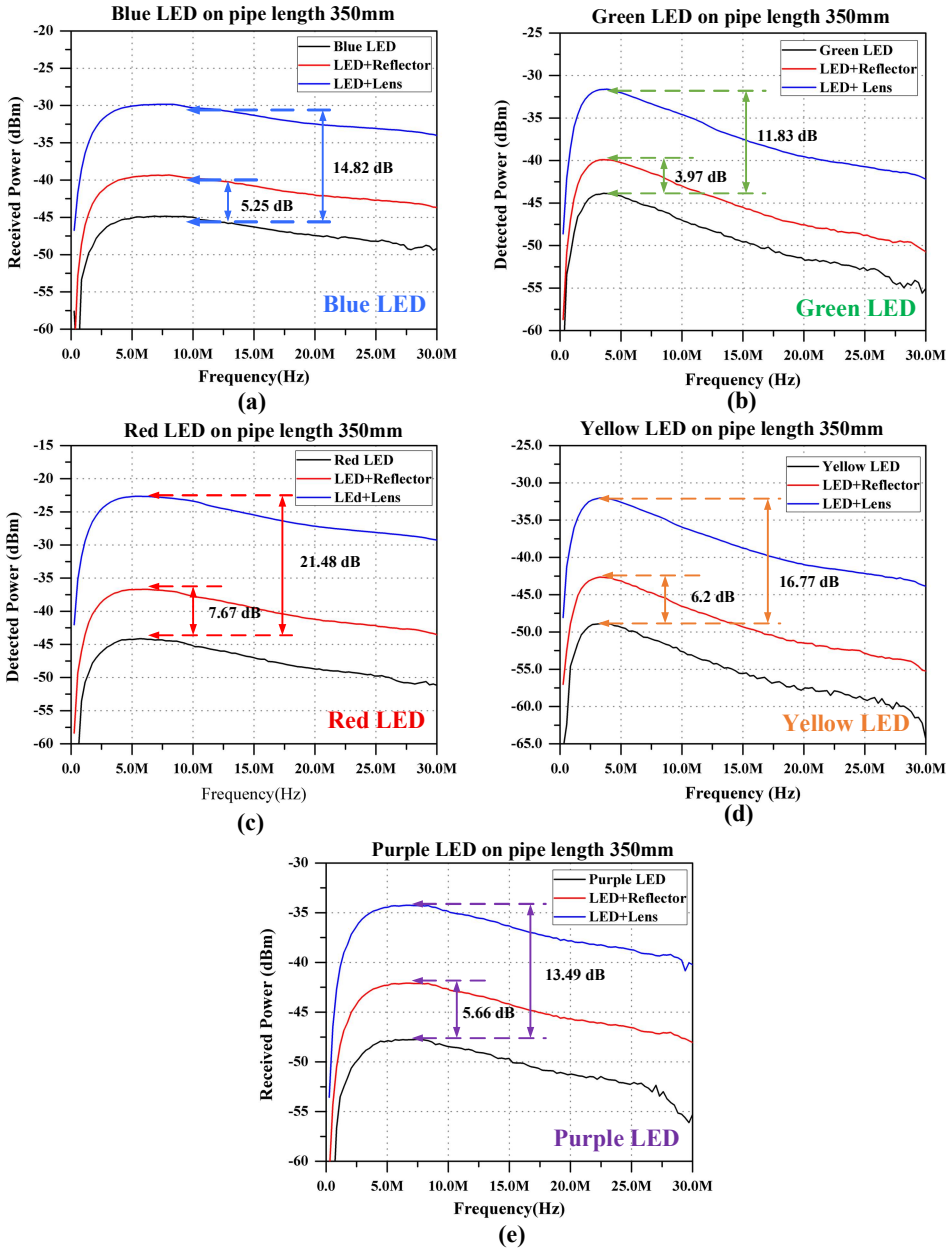

Figure 4.11 In-pipe frequency response of the LED at the pipe length of 350 mm: (a) 475 nm, (b) 528 nm, (c) 625 nm, (d) 583 nm, (e) 410 nm.

The incorporation of optical components significantly improves system performance. Optical reflectors enhance received power by approximately 3–8 dB by redirecting otherwise lost optical rays and improving confinement within the pipe. The addition of optical lenses provides a further 8–14 dB gain by narrowing the LED divergence and improving spatial coupling efficiency between the transmitter and receiver. When combined, these components act synergistically to suppress angular spread and reduce scattering-induced losses, resulting in the highest observed gain—up to 21 dB for the red LED.

Performance improvements are wavelength dependent, with longer wavelengths (yellow and red) consistently outperforming shorter wavelengths (blue and violet). This behavior is attributed to reduced Rayleigh scattering and improved directional confinement at longer wavelengths, which preserve higher-frequency signal components more effectively. Overall, the results demonstrate that wavelength selection and optical component optimization directly enable improved power efficiency and bandwidth in confined optical wireless communication systems.

4.4.2 Experimental results of the 1,000-mm pipe length

This section presents the experimental analysis of received optical power in a 1,000 mm in-pipe transmission setup, examining how wavelength and optical enhancements influence performance. The extended path length introduces higher attenuation and increased multipath interference, providing a more rigorous assessment of signal stability and propagation behavior in confined environments.

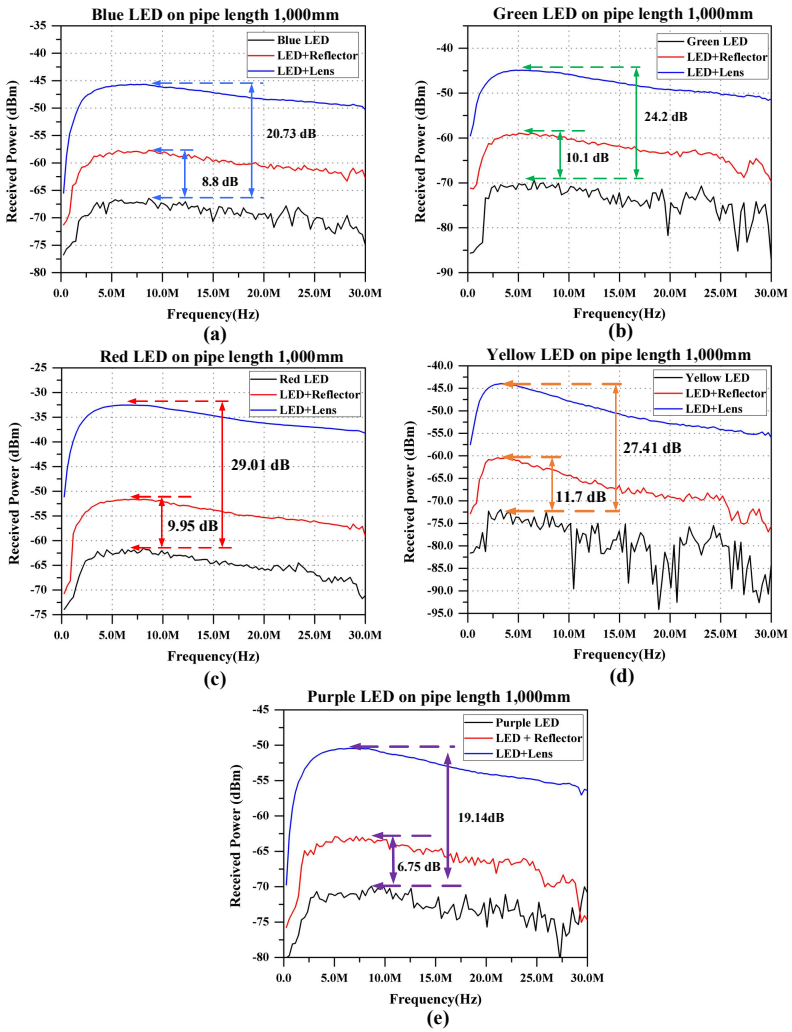

Figure 4.12 In-pipe frequency response of the LED at the pipe length of 1,000 mm: (a) 475 nm, (b) 528 nm, (c) 625 nm, (d) 583 nm, (e) 410 nm.

As shown in Figures 4.12(a)–4.12(e), all LEDs experienced a reduction in received power below –50 dBm at higher frequencies, with longer wavelengths (red and yellow) generally maintaining higher signal stability.

The experimental results show that extending the in-pipe transmission distance to 1,000 mm leads to a noticeable reduction in received optical power at higher modulation frequencies for all wavelengths, with signal levels falling below –50 dBm. This behavior confirms that increased path length intensifies attenuation and multipath effects due to cumulative scattering, absorption, and wall interactions within the confined pipe environment. Despite this, longer wavelengths (red and yellow) exhibit higher signal stability and reduced fluctuation, indicating more robust propagation over extended distances.

The use of optical reflectors improves received power by approximately 9–12 dB by enhancing optical confinement and redirecting otherwise lost rays toward the receiver. Further gains are achieved with optical lenses and the combined lens–reflector configuration, yielding total enhancements of up to 24 dB. These improvements occur because beam collimation and improved alignment reduce angular spread and multipath dispersion, preserving more optical power over the longer propagation distance.

Shorter wavelengths (blue and green) benefit most from optical enhancement due to their inherently wider divergence and higher sensitivity to beam shaping, while longer wavelengths maintain higher baseline power because of reduced scattering and more efficient surface coupling. Overall, the results demonstrate that the proposed optical design effectively compensates for distance-induced losses, enabling improved signal stability and extended communication range in long-distance in-pipe optical wireless communication systems.

4.4.3 The frequency response of the plastic pipe channel

In this section, we present a comprehensive analysis of the frequency response characteristics of the plastic pipe channel, with particular emphasis on the total attenuation per unit length. The experimental investigation is based on precise measurements of received optical power conducted at two different pipe lengths: 350 mm and 1,000 mm—representative scenarios for Optical Wireless Communication (OWC) applications in confined environments.

The total attenuation per unit distance encompasses both atmospheric attenuation and geometric spreading losses that occur in air-filled media, as supported by previous studies (36), (37). This cumulative attenuation effect is governed by a combination of absorption, scattering, and geometric dispersion, which collectively influence signal degradation as the light propagates through the pipe.

The attenuation behavior is quantitatively described by the following equation, adapted from established theoretical frameworks (38):

$$attenuation\left(dB/cm\right)=\frac{10\log}{l}\left[\frac{P(1)}{P(2)}\right] \tag{4.1}$$

where *P(1)* is the received power at 350mm, *P(2)* is the received power at 1,000mm, and *l* is the length of the plastic pipe in centimeters.

Figure 4.13 illustrates the measured in-pipe attenuation characteristics across five different LED wavelengths: 410 nm (purple), 470 nm (blue), 525 nm (green), 590 nm (yellow), and 625 nm (red). The results reveal a clear wavelength-dependent attenuation trend, with the highest attenuation observed at 410 nm (purple), measuring 0.301 dB/cm. In contrast, the lowest attenuation occurs at 625 nm (red), with a value of 0.218 dB/cm.

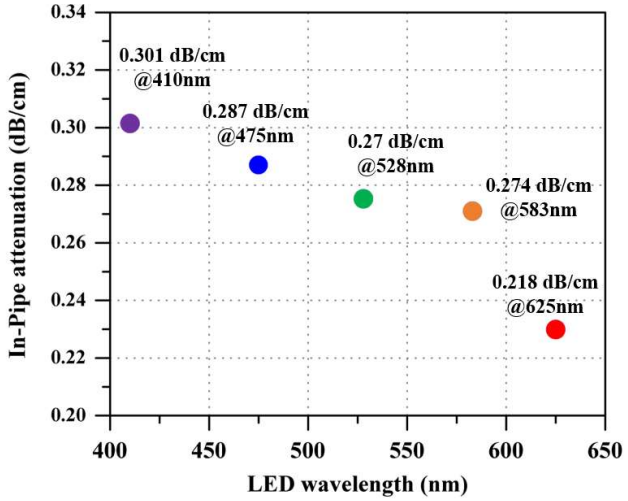

Figure 4.13 The in-pipe attenuation per unit length for different LED wavelengths.

A comparison between the attenuation values measured in the in-pipe experiments and those obtained under free-space conditions reveals a consistent trend that corresponds with the transmittance windows observed in the optical absorption spectrum (39). Notably, shorter wavelengths exhibit significantly higher attenuation compared to longer wavelengths, corroborating findings from previous studies (40), (41), (42), (43).

The experimental results show a clear wavelength-dependent attenuation behavior in the plastic pipe OWC channel, with attenuation increasing as the wavelength decreases. Measurements at 350 mm and 1,000 mm consistently indicate that shorter wavelengths, particularly 410 nm, experience the highest attenuation per unit length, while longer wavelengths, especially 625 nm, exhibit the lowest attenuation. This confirms that signal degradation in the pipe intensifies with propagation distance and is strongly influenced by spectral characteristics.

This behavior arises from the combined effects of absorption, scattering, and geometric spreading within the confined pipe environment. Shorter wavelengths are more susceptible to scattering and surface interactions with the plastic pipe walls, leading to higher energy loss and reduced transmission efficiency. In contrast, longer wavelengths experience reduced scattering and more efficient propagation, resulting in lower attenuation per unit distance and improved signal stability.

The close agreement between the in-pipe attenuation trend and free-space transmittance windows further validates the physical consistency of the measurements and confirms that the pipe primarily amplifies wavelength-dependent losses already present in air.

4.5 Discussion

This chapter presented a comprehensive study on the frequency response and signal attenuation characteristics of optical wireless communication (OWC) in a plastic pipe under free-space (air-filled) conditions. The investigation began with detailed simulations of LED electronic behavior using Keysight ADS and optical modeling in Ansys Zemax OpticStudio. These simulations evaluated the frequency response across five monochromatic LEDs (410, 475, 528, 583, and 625 nm) and assessed how different circuit configurations affect bandwidth and signal strength.

Subsequent experimental validation employed a 350 mm PVC pipe to assess in-pipe transmission performance. Optical enhancements, including metallized polycarbonate reflectors and PMMA lenses, were analyzed for their role in improving signal directivity and power. The integration of these components led to significant gains in received power, with blue and red LEDs benefiting most from combined optical enhancements.

Further experiments extended the pipe length to 1,000 mm to evaluate long-range transmission effects. Results showed pronounced signal fluctuations at lower received power levels, particularly for LEDs with shorter wavelengths. However, optical elements mitigated these losses, with notable improvements in received power and reduced signal instability.

Finally, the chapter calculated the in-pipe attenuation per unit distance across different wavelengths. The results confirmed a wavelength-dependent trend, with higher attenuation observed at shorter wavelengths (e.g., 410 nm) and lower attenuation at longer wavelengths (e.g., 625 nm). These findings aligned well with theoretical absorption spectra and established the foundational characteristics for optimizing OWC systems in confined air-filled pipe environments.

This chapter provides one of the first comprehensive experimental and simulation-based analyses of LED behavior in enclosed PVC pipelines, quantifying the effect of pipe geometry and optical component integration on frequency response. This contributes new insight into wavelength-dependent propagation in confined air-filled structures.

Chapter 5

Thermal Management and Heatsink Optimization in LED-Based OWC Systems

5.1 Introduction

Effective thermal management is essential to maintaining the performance, reliability, and lifespan of light-emitting diodes (LEDs) used in optical wireless communication (OWC) systems. Elevated junction temperatures can significantly degrade optical output, cause spectral wavelength shifts, and accelerate device aging. A common measure of LED reliability is the relative luminous flux, defined as the percentage of initial light output maintained over time, with 70% often used as the standard lifetime benchmark (44), (45).

To mitigate thermal effects, two primary cooling approaches are widely employed: heat pipe cooling and heatsink-based cooling. While heat pipes achieve high heat transfer efficiency through liquid-phase mechanisms, they introduce structural complexity and bulk. In contrast, heatsink cooling relies on conductive and convective dissipation through extended metallic surfaces, offering a simpler and more practical solution for compact OWC systems (40).

This chapter presents a systematic investigation into the thermal behavior of high-power LEDs equipped with an optimized heatsink structure, designed to improve cooling efficiency and enhance modulation bandwidth in optical wireless communication (OWC) systems. The experimental study varies the LED forward bias current from 10 mA to 1,000 mA across five wavelengths to evaluate the influence of temperature on both optical output and frequency performance. The heatsink design maximizes fin surface area for forced convection airflow, following the square fin geometry and heat transfer analysis framework proposed by (Incropera et al., 25).

Addressing Research Question 2, this study investigates the quantifiable impact of thermal management on LED transmitted performance in OWC systems. Through a combination of SolidWorks CFD simulations and experimental validation, the chapter quantifies how improved thermal regulation affects junction temperature, optical power, and modulation bandwidth. The results advance the understanding of thermal–optical coupling and highlight the critical role of thermal optimization in enhancing the overall efficiency and reliability of LED-based OWC transmitters.

5.2 Thermal and Frequency Response Setup

Thermal analysis and frequency response experiments were performed using five monochromatic LEDs integrated with three heatsink designs: starboard baseline, conventional aluminum fin, and optimized square-fin heatsink developed in SolidWorks and validated through CFD thermal simulations. LEDs were driven by a Keysight technology E3632A DC power supply, supplying variable forward currents between 10 mA and 1,000 mA

Figure 5.1 illustrates the experimental setup used to evaluate the frequency response characteristics of the Optical Wireless Communication (OWC) system within a 350 mm PVC pipe. The configuration integrates both electronic and optoelectronic subsystems to analyze the modulation behavior of high-power LEDs across a wide frequency range. Frequency response measurements were conducted using a Keysight E8257D signal generator, which modulated the LED with sinusoidal signals up to 50 MHz. The resulting optical signal was captured by a Thorlabs PDA10A2 photodetector equipped with an internal transimpedance amplifier, and the electrical output was analyzed using an Agilent CXA N9000A signal analyzer. The –3 dB bandwidth was determined from the normalized frequency response curve, allowing direct correlation between thermal effects, modulation performance, and the system's overall communication bandwidth.

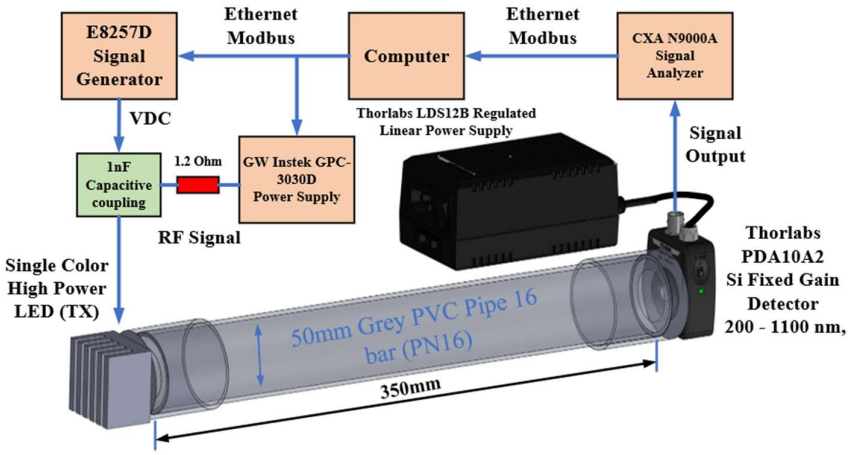

Figure 5.1 The frequency response and thermal analysis experimental setup.

5.3 The thermal analysis

Effective thermal management is critical in optimizing the performance and longevity of LEDs, particularly in optical wireless communication (OWC) systems where temperature directly affects optical output and device reliability. To achieve efficient heat dissipation, the thermal behavior of heatsinks must be rigorously analyzed and optimized. In this context, thermal resistance modeling serves as a vital analytical tool, enabling the evaluation of heat transfer pathways within the cooling structure. In particular, heat transfer equations allow for the systematic representation of the multiple thermal resistances that contribute to the total thermal impedance of the system. As described by (Lasance and Poppe., 45), the formulation of thermal resistance provides a foundational understanding of how heat is conducted, convected, and dissipated through different components of the heatsink. By quantifying each individual resistance, their cumulative effect can be assessed through summation, ultimately determining the total thermal resistance of the system, as presented in Equation (5.1).

$$R_{total} = R_{chip} + R_{TC} + R_{base,cond} + \left(\frac{R_{base,conv}.R_{fins,conv}}{R_{base,conv} + R_{fins,conv}} \right) + R_{flow} \tag{5.1}$$

Here, R_{total} represents the thermal resistance value of the heatsink; R_{chip} denotes the thermal resistance value of the LED chip; R_{TC} represents the thermal resistance of the thermal compound, with a specified value of 0.128 K/W; $R_{fins,conv}$ signifies the thermal resistance value of the fin array; $R_{base,conv}$ refers to the thermal resistance of the base area between the fins, and R_{flow} represents the thermal resistance associated with the airflow over surfaces.

Figure 5.2 presents a visual representation of the thermal network model derived from heatsink, while Figure 5.3 provides a detailed illustration of the heat transfer pathway from the LED to the ambient environment, as described by (Lasance and Poppe., 45). The determination of the optimal number of cooling fins is governed by Equation (5.2).

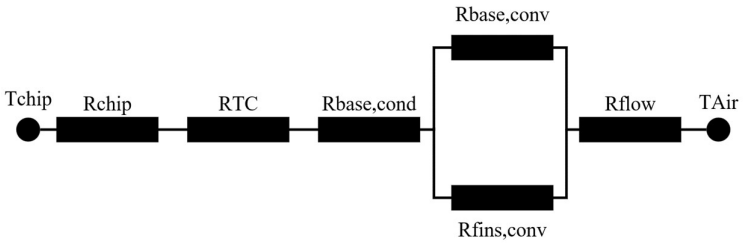

Figure 5.2 The heat sink's thermal network models (45).

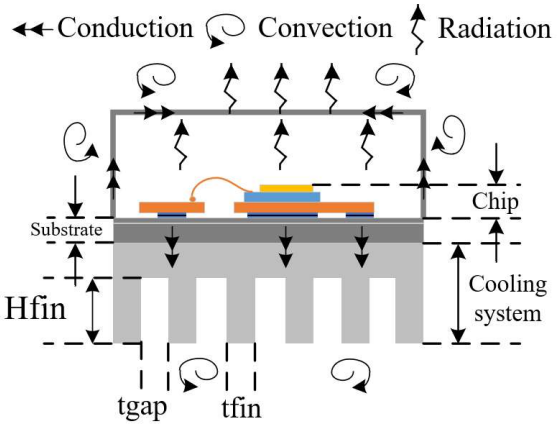

Figure 5.3 Thermodynamics of LED systems, which provide light on the complex interaction between the semiconductor device (45).

$$N_{fin} = \frac{t_{gap} + 0.025}{t_{gap} + t_{fin}} \tag{5.2}$$

In this context, N_{fin} denotes the number of cooling fins on the heatsink, t_{gap} represents the spacing between the fins, and t_{fin} corresponds to the thickness of each fin. T_{chip} and T_{air} refer to the temperatures of the LED chip and ambient air, respectively.

With regard to response time analysis, the heat capacity (H.C.) of the heatsink—an essential parameter for evaluating thermal inertia—can be defined following the methodologies outlined by (Bar-Cohen et al., 26).

5.4 Heatsink optimization and simulation

This section focuses on the thermal optimization of a square aluminum heatsink measuring 25 mm, aimed at enhancing LED efficiency for optical wireless communication (OWC) applications. The study involves a comparative analysis between a baseline design—featuring six fins with equal fin and gap widths (t_{gap}=t_{fin}=2 mm) and an improved configuration in which key design parameters are systematically varied. While environmental constants, such as ambient air properties, remain fixed, selected heatsink characteristics are modified as outlined in Table 5-1. This structured investigation seeks to evaluate the influence of specific geometric adjustments on the heartsink's thermal performance, ultimately supporting the development of more efficient thermal management solutions for LED-based OWC systems.

Table 5-1 variable parameters

Parameters	Value
Length of the block (L)	25 mm
Width of the block (W_{base})	25 mm
Base thickness	2 mm.
Heat Capacity Aluminum (6063)	875 J/kg K
Density of Aluminum	2,700 kg/m^3
Thickness of the fin $(\boldsymbol{t_{fin}})$	0.5, 1.0, 1.5, 2.0, 2.5, 3.0 mm.
The gap thickness $(\boldsymbol{t_{gap}})$	0.5, 1.0, 1.5, 2.0, 2.5, 3.0 mm.
Height of the fin $(\boldsymbol{H_{fin}})$	8, 10, 15 mm.
Number of the fins $(\boldsymbol{N_{fin}})$	27 – 4 fins
Air flow rate $(\boldsymbol{Air_{flow\ rate}})$	15, 10, 5, 2 CFM

In evaluating the performance of the heatsink designs, the influence of airflow rates—specifically 15, 10, 5, and 2 CFM—was systematically analyzed. Among

these, the 15 CFM airflow rate yielded the most significant reduction in chip temperature, as presented in Table 5-2. Additionally, the impact of fin height variations (8 mm, 10 mm, and 15 mm) was investigated. The configuration with a 15 mm fin height demonstrated the highest thermal efficiency, achieving an overall efficiency of 0.869.

Table 5-2 The impact of chip temperature at fin heights of 8, 10, and 15 mm

t_{gap} (mm)	t_{fin} (mm)	H_{fin} (mm)	t_{chip} ℃	N_{fin}	η_{fin}	η_0
2.0	2.0	8,10,15	31.18	6	0.691	0.694
			32.35		0.815	0.817
			33.45		0.867	0.869

Table 5-3 presents the optimal values for key heatsink design parameters, including air inlet flow rate, fin thickness, fin height, and the number of fins, determined through an in-depth analysis aimed at minimizing chip temperature. The study evaluated thermal performance under airflow rates of 15, 10, 5, and 2 CFM, offering valuable insights into the influence of these parameters. The configuration that achieved the most effective thermal performance consisted of a fin gap (t_{gap}) of 0.5 mm, fin thickness (t_{fin}) of 2 mm, fin height (H_{fin}) of 15 mm, number of fins (N_{fin}) equal to 10, and an airflow rate of 15 CFM. These parameter values were identified as critical for optimizing the thermal management system and achieving the lowest chip temperature.

Table 5-3 Optimal values for air inlet and fin thickness

t_{gap} **(mm)**	t_{fin} **(mm)**	H_{fin} **(mm)**	t_{chip} **℃**	$Air_{flowrate}$ **(CFM)**	N_{fin}	η_0
0.5	2.0	8	27.3	15	10	0.775
			28.42	10		0.696
			32.05	5		0.793
			36.91	2		0.842
0.5	2.0	10	27.15	15	10	0.534
			28.24	10		0.616
			31.68	5		0.725
			36.35	2		0.785
0.5	2.0	15	27.06	15	10	0.386
			28.06	10		0.460
			31.27	5		0.575
			35.69	2		0.648

The analysis of the heatsink design's influence on the total thermal resistance (R_{total}) reveals its critical role in governing chip temperature and overall thermal

performance. As depicted in Figure 5.4, a lower R_{total} directly correlates with enhanced heat transfer efficiency, enabling more effective dissipation of thermal energy from the LED chip. This relationship is consistent with findings reported by Lasance and Poppe, who emphasized the importance of minimizing thermal resistance in high-performance electronic cooling systems (45).

Key design parameters contributing to the reduction of R_{total} include increased fin thickness, a greater number of fins, and higher forced airflow rates. These factors synergistically improve convective heat transfer by expanding the surface area available for thermal exchange and accelerating the rate at which heat is removed from the heatsink surface.

Furthermore, the impact of R_{total} on chip temperature becomes even more pronounced under transient thermal conditions. A comparative assessment of the original and optimized heatsink configurations highlights substantial improvements in thermal regulation, as summarized in Table 5-4, which provides the time-response equation used to model temperature evolution. During the initial high-temperature phase, thermal inertia results in residual heat accumulation within the LED chip. The optimized heatsink configuration mitigates this effect more effectively, thereby ensuring faster thermal stabilization and reducing the risk of thermal degradation over time.

Table 5-4 Temporal Variation of Dynamic Chip Temperature

$t_{gap}, t_{fin}, H_{fin}, Air_{flowrate}$	Time-dependent chip temperature
(2.0,2.0,8,15) Conventional	$T(t) = 306.5954 + (-11.4454)(e^{-0.2026t})$
(0.5,2.0,8,15)	$T(t) = 300.4524 + (-5.3024)(e^{-0.3041t})$
(0.5,2.0,10,15)	$T(t) = 300.2952 + (-5.1452)(e^{-0.2633t})$
(0.5,2.0,15,15)	$T(t) = 300.1957 + (-5.0457)(e^{-0.1917t})$

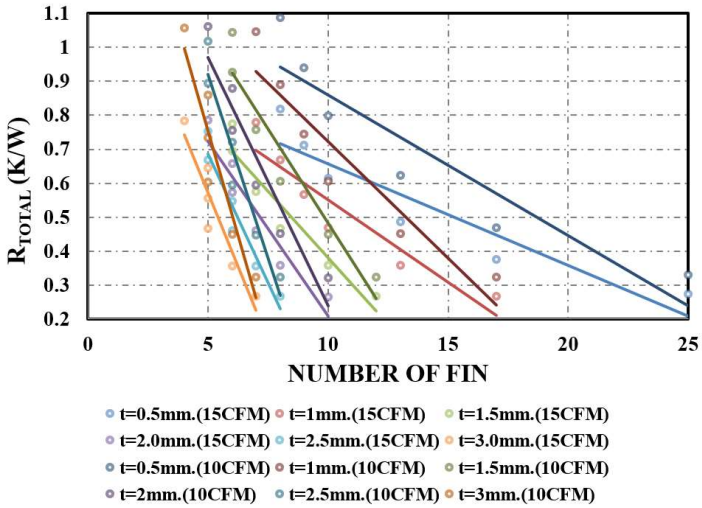

Figure 5.4 The relationship between fin thickness, quantity of fins, airflow rate, and total resistance (R_{total})**.**

The analysis of the transient thermal response time of the LED chip, as illustrated in Figure 5.5, demonstrates that the optimized heatsink design significantly reduces the duration required to reach thermal equilibrium when compared to the original configuration. Specifically, the redesigned configurations exhibit notably shorter transient durations than the baseline design, which requires approximately 15 seconds to stabilize. Exceptions to this trend are observed in the configuration employing a 15 mm fin height, where the transient duration slightly increases to 17 seconds. This increase is attributed to the added thermal mass and surface area, which, while enhancing steady-state cooling, require a longer time to fully dissipate the initial heat load.

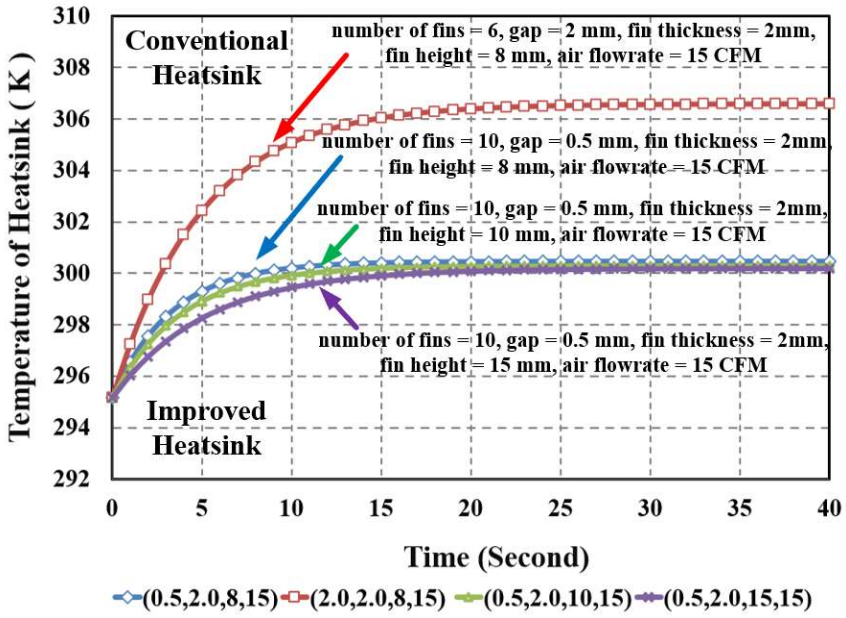

Figure 5.5 the ephemeral thermal response of the optimized chip.

Optimization results obtained through MATLAB simulations further corroborate these findings. The conventional heatsink exhibits a steady-state chip temperature of approximately 306.6 K, whereas the optimized heatsink design maintains a substantially lower and more stable chip temperature of 300.3 K. This 6.3 K reduction highlights the effectiveness of the design modifications—particularly adjustments to fin geometry and airflow conditions—in enhancing the thermal performance of the system. These improvements contribute not only to increased LED lifespan and stability but also to the overall efficiency of the optical wireless communication (OWC) system.

The experimental methodology replicates the real-world heat dissipation conditions encountered by a commercial LED heatsink, incorporating modifications in the number of cooling fins to assess their influence on thermal performance. For simulation purposes, SolidWorks thermal analysis tools were employed to calculate temperature distributions and heat transfer behavior within a three-dimensional model of heatsink. The comparative analysis revealed that the conventional heatsink

design resulted in a minimum fin temperature of 315 K. In contrast, the optimized heatsink design demonstrated improved thermal performance, with a reduced fin temperature of 306 K, as depicted in Figure 5.6.

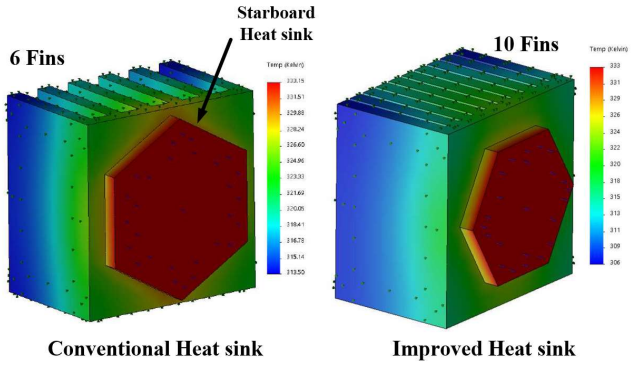

Figure 5.6 Results of a 3D thermal simulation using SolidWorks software.

To further evaluate the thermal efficiency of the redesigned, heatsink, SolidWorks Computational Fluid Dynamics (CFD) and Flow Simulation modules were utilized. These simulations focused primarily on characterizing natural convection heat transfer mechanisms under varying airflow conditions. The comprehensive CFD setup and its corresponding outcomes are illustrated in Figure 5.7 The analysis allowed for an in-depth investigation of how different fin configurations and airflow rates impact the overall thermal behavior of the system. The resulting data provided critical insights into the optimization of fin geometry and spacing for maximum heat dissipation efficiency, reinforcing the effectiveness of the new heatsink design in enhancing the thermal management of high-power LEDs in optical wireless communication (OWC) systems.

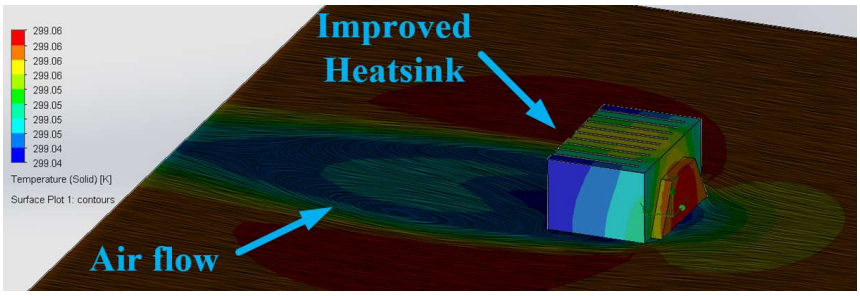

Figure 5.7 shows the results of a 3D CFD simulation using SolidWorks software.

Figure 5.8 presents the simulation results for the improved heatsink design under varying natural convection airflow conditions, as modeled using SolidWorks CFD tools. The outcomes underscore a pronounced inverse relationship between airflow rate, and the resulting heatsink temperature. As the airflow rate increases, the

thermal resistance of the system decreases, thereby enhancing convective heat transfer and reducing the steady-state temperature of the heatsink.

For instance, at a high airflow rate of 40 cubic feet per minute (CFM), the heatsink achieves a significantly reduced operating temperature of 303.5 K. Conversely, when the airflow is limited to 5 CFM, the heatsink temperature rises markedly to 313.6 K. This 10.1 K differential highlights the critical influence of airflow dynamics on thermal performance. The findings emphasize that optimizing the airflow rate is essential for maintaining lower junction temperatures in LED systems, which is vital for preserving luminous efficacy, preventing thermal degradation, and extending operational lifespan in optical wireless communication (OWC) applications. These results further validate the importance of integrating appropriate forced convection strategies into the thermal design of high-power LED systems.

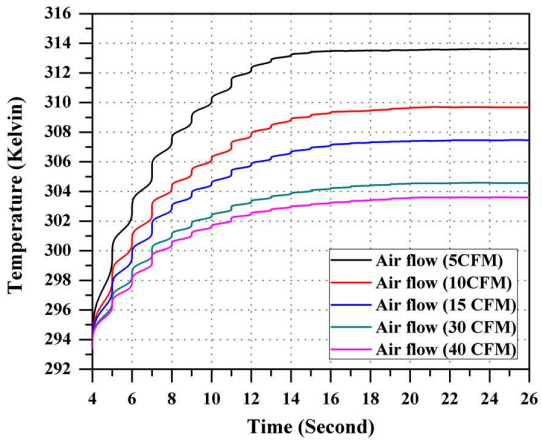

Figure 5.8 The air flow rate varies as a consequence of a 3D CFD simulation.

The thermal optimization analysis yielded a marked improvement in the heatsink's cooling performance when compared to the conventional configuration. Specifically, the conventional heatsink exhibited an operational temperature of approximately 306.6 K, whereas the optimized design, featuring a fin height of 15 mm, successfully reduced the temperature to 300.2 K. These findings indicate that increasing the number and height of the fins significantly reduces the overall thermal resistance of the system, thereby enhancing heat dissipation via improved conduction and convection mechanisms.

The optimization results suggest that while augmenting fin count and height generally contributes to better thermal management, practical limitations must be considered. As observed by Gaikwad et al., excessive fin density can lead to non-compact geometries, increased material usage, and elevated fabrication costs, thereby undermining the economic and spatial feasibility of the heatsink design (46). Furthermore, increasing fin height beyond a certain threshold may result in

diminishing returns, as the thermal benefit may plateau despite added material and volume.

The study observed that increasing the number of fins from 6 to 10 led to a substantial reduction in heatsink temperature—from 306.6 K to 300.2 K—demonstrating the efficiency gains achieved through optimized surface area exposure. However, modifications based solely on increasing fin height revealed only marginal improvements in thermal performance. This outcome emphasizes the need for a balanced design strategy that optimizes both the number and height of the fins to achieve effective heat dissipation without compromising the compactness or manufacturability of the system.

The operating temperature of a heatsink is intrinsically linked to its total thermal resistance, particularly in applications involving high-power components such as LEDs. During operation, LEDs generate heat that must be promptly and efficiently transferred away from the device to prevent thermal degradation and maintain optical performance. The heatsink functions as a critical thermal interface by absorbing the generated heat and dissipating it into the ambient environment. Therefore, reducing thermal resistance through thoughtful design directly contributes to system reliability, prolonged device lifetime, and stable performance in optical wireless communication (OWC) applications.

The operational temperature of a heatsink is intrinsically linked to its thermal resistance, a relationship that can be quantitatively defined by Equation (5.3):

$$\Delta T = P \times R_{th} \tag{5.3}$$

where ΔT represents the temperature differential across the heatsink, P denotes the thermal power input, and R_{th} is the total thermal resistance. This equation highlights the fundamental role of thermal resistance in determining the heatsink's temperature under load conditions. In practical terms, reducing R_{th} through strategic design improvements directly lowers the temperature rise, thereby enhancing the overall heat dissipation efficiency.

Extensive research and design modifications, such as increasing the number and height of fins, have shown to significantly reduce thermal resistance. These enhancements promote more efficient convective heat transfer by increasing the surface area available for air contact, thus improving the overall thermal performance of the system.

Experimental validation of this principle is evident in the observed temperature profiles of various heatsink configurations. A conventional heatsink equipped with six fins demonstrated an operational temperature of 306.6 K, whereas an optimized design incorporating ten fins achieved a reduced temperature of 300.3 K. This 6.3 K decrease in operating temperature has notable implications for LED performance. Elevated temperatures are associated with diminished optical power output and reduced frequency bandwidth, both of which are critical parameters in optical wireless communication (OWC) systems. These performance degradations were clearly observed in the experimental measurements detailed in Figures 5.9.

In conclusion, these findings underscore the indispensable role of thermal management in LED-based systems. The optimization of heatsink design not only ensures lower operating temperatures and improved energy efficiency but also extends the functional lifetime and reliability of the LED components.

5.5 Experimental results of heatsink optimization

5.5.1 Experimental measurement of received power

This section presents a comparative evaluation of the frequency response and received optical power of LEDs within a 350 mm in-pipe configuration under three heatsink designs: a standard starboard heatsink, conventional aluminum fin heatsinks, and an optimized improved heatsink.

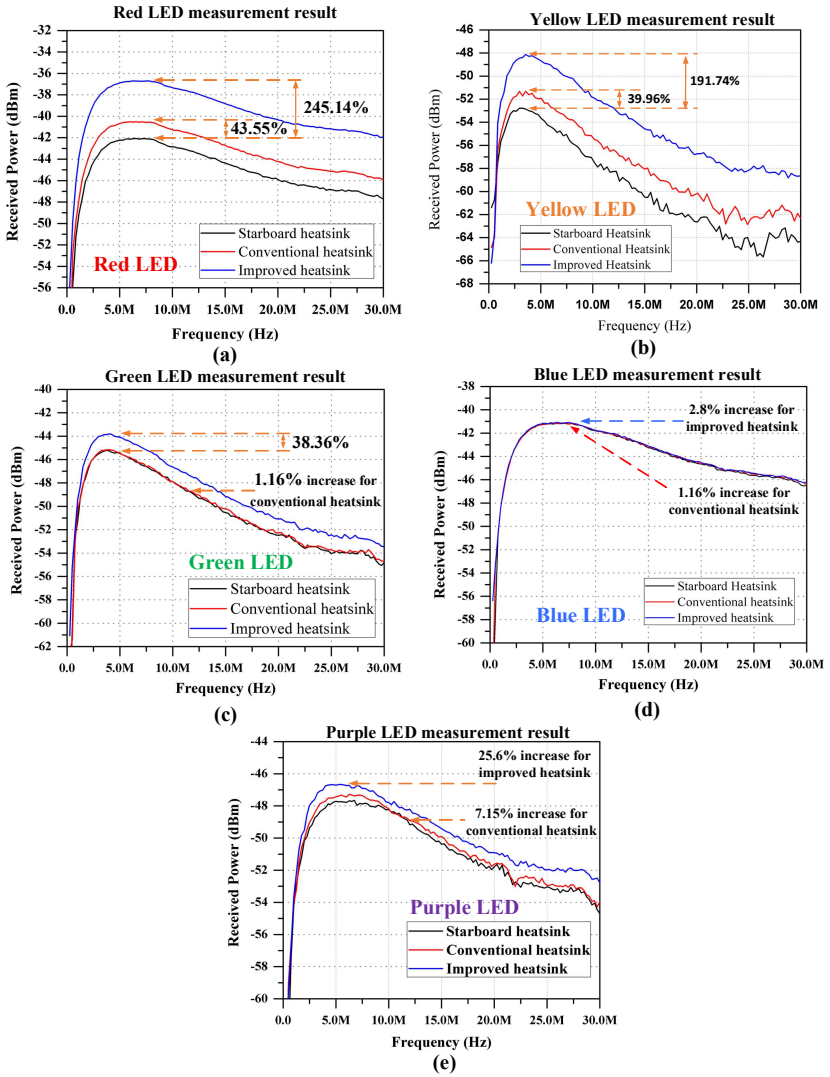

Figure 5.9 Comparative evaluation of received optical power of LEDs with three heatsinks implemented: (a) Red LED, (b) Yellow LED, (c) Green LED, (d) Blue LED, (e) Purple LED.

The results, summarized in Figures 5.9(a)–5.9(e), reveal a consistent enhancement in received power across all wavelengths when improved thermal management is applied, confirming the strong coupling between thermal regulation and optical performance.

The experimental results demonstrate that improved thermal management consistently enhances received optical power across all wavelengths in the 350 mm in-pipe configuration. Compared with the starboard and conventional fin heatsinks, the optimized heatsink delivers the highest performance, confirming that effective LED thermal regulation has a direct impact on optical output and frequency-response stability.

Across the visible spectrum, the optimized heatsink achieves the greatest improvement in received power, with gains of 245% for red (625 nm), 192% for yellow (590 nm), and 38% for green (525 nm) relative to the baseline starboard design. Shorter wavelengths such as blue (470 nm) and purple (410 nm) show more modest enhancements of 2.8% and 25.6%, respectively. These variations indicate that longer wavelengths benefit more strongly from thermal stabilization because their quantum efficiency and radiative recombination processes are more sensitive to junction temperature. Improved heat dissipation lowers the junction temperature, suppresses nonradiative recombination, and preserves luminous efficiency, thereby increasing the received optical power.

The smaller gains observed at shorter wavelengths can be explained by Wien's displacement law (66), whereby temperature variations cause a spectral shift toward shorter wavelengths, resulting in higher photon energy losses and a reduced relative benefit from cooling. In addition, thermal stress affects the internal quantum efficiency of blue and violet LEDs less significantly than that of red and yellow devices, which rely more heavily on temperature-dependent carrier dynamics.

Overall, these results confirm that optimized heatsink design directly mitigates thermal degradation mechanisms in LEDs, substantially enhancing signal strength and spectral stability—particularly under high-bias operation where thermal loading is pronounced. The findings are consistent with prior studies (Lasance et al. [43]) showing that elevated junction temperatures reduce LED output due to increased nonradiative recombination.

5.5.2 Experimental measurement of frequency bandwidth

This section analyzes the in-pipe frequency bandwidth characteristics of LEDs across five wavelengths and evaluates the influence of three heatsink configurations on thermal performance. The frequency bandwidth, defined as the frequency at which the alternating current (AC) optical power falls to 50% of its baseline value (–3 dB point), directly determines the achievable data rate and channel capacity in OWC systems (47), (48), (49).

The experimental results show that improving thermal management through optimized heatsink design consistently increases the in-pipe frequency bandwidth of

LEDs, with the magnitude of improvement strongly dependent on wavelength. As summarized in Table 5-5, longer-wavelength LEDs (red and yellow) exhibit the largest bandwidth enhancements, while shorter-wavelength LEDs (blue and purple) show only marginal gains.

The results align with the findings of (Alexeev et al., 50) who reported a nearly linear relationship between temperature and 3 dB bandwidth, where a 100 K increase could reduce bandwidth by up to 15%. Additionally, the measured 3 dB bandwidth of the 470 nm blue LED (27.07 MHz) closely matches the 30 MHz reported by (Wan et al., 51) confirming the validity of the experimental data.

This behavior occurs because the modulation bandwidth of LEDs is directly influenced by junction temperature, which affects carrier lifetime, recombination dynamics, and bandgap stability. The improved heatsink more effectively dissipates heat, reducing junction temperature fluctuations and suppressing carrier leakage and nonradiative recombination. As a result, carrier dynamics become faster and more stable, extending the –3 dB bandwidth. Longer-wavelength LEDs benefit more from this thermal stabilization because their radiative efficiency and recombination rates are more sensitive to temperature variations, leading to substantial bandwidth recovery when thermal loading is reduced.

In contrast, shorter-wavelength LEDs operate at higher photon energies and exhibit weaker thermal–optical coupling, limiting the extent to which improved cooling can enhance their modulation bandwidth. The agreement between the measured bandwidth values and previously reported results further validates the experimental approach and confirms that the observed improvements arise from effective thermal optimization rather than measurement artifacts.

Table 5-5 summarizes the frequency bandwidth and received power comparison.

LED wavelength (nm)	Received Power (dBm)			The increase in received power (%)		Frequency Bandwidth (MHz)			The increase in frequency bandwidth (%)	
	Starboard heatsink	Conventional heatsink	Improved heatsink	Conventional heatsink	Improved heatsink	Starboard heatsink	Conventional heatsink	Improved heatsink	Conventional heatsink	Improved heatsink
Red LED (625nm)	-42.08	-40.51	-36.7	43.55%	245.14 %	18.63	20.73	25.24	11.27%	35.48 %
Yellow LED (583nm)	-52.77	-51.31	-48.12	39.96%	191.74 %	8.41	9.32	9.62	23.94%	27.93 %
Green LED (528nm)	-45.21	-45.16	-43.8	1.16%	38.36 %	21	23.5	23.75	11.9%	13.1%
Blue LED (475nm)	-41.19	-41.14	-41.07	1.16%	2.8%	57.14	58.15	58.65	1.77%	2.64%
Purple LED (410nm)	-47.65	-47.35	-46.66	7.15%	25.6%	24.5	24.80	24.83	1.25%	1.36%

5.5.3 Modulation and data rate

In this section, a comparative evaluation is conducted between the conventional heatsink and the optimized heatsink design, with particular emphasis on assessing the maximum achievable data rate capacity within an optical wireless communication (OWC) system employing a digital single-carrier modulation scheme. The calculated results are comprehensively presented in Table 5-6.

The analysis is grounded in an idealized framework that assumes a noiseless communication environment to isolate and quantify the impact of bandwidth enhancement attributable solely to thermal management improvements. The computation of data rate capacity is performed using the Nyquist theorem (52), (53), which defines the theoretical maximum data transmission rate for a given bandwidth in a noise-free channel. This relationship is expressed as:

$$C = 2B\log_2(M) \tag{5.4}$$

where C represents the channel capacity in bits per second (bps), B denotes the frequency bandwidth in hertz (Hz), and M is the modulation level (number of signal levels or symbols). In this context, M is assumed to be constant across all comparative scenarios to isolate the influence of thermal performance on bandwidth.

By applying this model, the study effectively correlates the enhancements in thermal dissipation—achieved through the improved heatsink—with measurable increases in bandwidth, and consequently, in data rate capacity. The improved heatsink, by maintaining lower LED junction temperatures, supports higher modulation frequencies, thereby expanding the communication system's potential throughput.

Table 5-6 Modulation PPM/PAM schemes data rates

Modulation Scheme	Red LED data rate (Mbps)		Yellow LED data rate (Mbps)		Green LED data rate (Mbps)		Blue LED data rate (Mbps)		Purple LED data rate (Mbps)	
	CVHD	IPHD	CVHD	IPHD	CVHD	IPHD	CVHD	IPHD	CVHD	IPHD
2PPM/2PAM	41.45	50.48	18.64	19.24	47.00	47.50	116.30	117.30	49.61	49.67
4PPM/4PAM	82.91	100.95	37.28	38.48	94.00	95.00	232.61	234.59	99.23	99.33
8PPM/8PAM	124.37	151.44	55.92	57.72	140.99	142.51	348.91	351.89	148.84	149.00
16PPM/16PAM	165.83	201.92	74.56	76.96	187.99	190.01	465.21	469.19	198.45	198.67
32PPM/32PAM	207.29	252.40	93.20	96.20	234.99	237.51	581.51	586.48	248.06	248.33
64PPM/64PAM	248.75	302.88	111.84	115.44	281.99	285.01	697.82	703.78	297.68	298.00

** CVHD = the data rate achieved when utilizing a conventional heatsink. ** IPHD = the data rate achieved when utilizing an improved heatsink.

In the domain of optical wireless communication (OWC), the influence of noise on signal transmission is a critical factor that significantly affects the achievable data rate and overall system performance. The Shannon–Hartley theorem provides a theoretical framework for estimating the maximum data transmission capacity of a communication channel by incorporating two essential parameters: frequency bandwidth and signal-to-noise ratio (SNR). This relationship enables a more realistic evaluation of channel capacity under non-ideal conditions, as encountered in practical deployments (54).

The Shannon–Hartley capacity is mathematically expressed as:

$$C = B\log_2(1+SNR) \tag{5.5}$$

where C is the channel capacity in bits per second (bps), B is the channel bandwidth in hertz (Hz), and SNR is the signal-to-noise ratio in linear scale. This formulation

underscores the importance of both high bandwidth and favorable SNR values for maximizing data throughput in OWC systems.

Empirical investigations, including those by (Wu et al., 55) have examined the SNR behavior of LEDs operating in the red, green, and blue wavelength ranges over different transmission distances. Their study demonstrated that SNR values generally decrease with increasing distance: ranging from 15–30 dB at 20 cm, 10–25 dB at 40 cm, and 5–15 dB at 75 cm, all within a frequency range of 0.2 MHz to 50 MHz. These findings provide a practical foundation for quantifying capacity variations over distance using the Shannon–Hartley theorem (54).

Table 5-7 Signal-to-noise ratio (SNR) data rates

Signal to Noise Ratio	Red LED data rate (Mbps)		Yellow LED data rate (Mbps)		Green LED data rate (Mbps)		Blue LED data rate (Mbps)		Purple LED data rate (Mbps)	
SNR (dB)	CVHD	IPHD	CVHD	IPHD	CVHD	IPHD	CVHD	IPHD	CVHD	IPHD
5	53.58	65.24	24.09	24.87	60.75	61.39	150.32	151.60	64.11	64.18
10	71.71	87.32	32.24	33.28	81.30	82.16	201.17	202.90	85.79	85.90
15	82.92	100.96	37.28	38.48	94	95	232.6	234.6	99.2	99.32
20	91.05	110.86	40.94	42.25	103.22	104.32	255.41	257.61	108.93	109.06
25	97.44	118.64	43.81	45.22	110.46	111.64	273.33	275.68	116.57	116.71
30	102.7	125.04	46.17	47.66	116.42	117.66	288.09	290.56	122.86	123.01

** CVHD = the data rate achieved when utilizing a conventional heatsink. ** IPHD = the data rate achieved when utilizing an improved heatsink.

The results show that the achievable data capacity of the OWC channel is strongly governed by both bandwidth and signal-to-noise ratio (SNR), as predicted by the Shannon–Hartley theorem. Experimental observations confirm that SNR decreases with increasing transmission distance, which directly limits the maximum theoretical data rate even when sufficient bandwidth is available. This trend reflects the increasing impact of optical attenuation, noise, and power spreading in practical LED-based OWC links.

By applying the Shannon–Hartley formulation to empirically measured SNR values and bandwidths, the calculated channel capacities in Table 5-7 demonstrate how reductions in SNR translate into diminished data throughput. The consistency between the calculated capacities and previously reported SNR ranges validates the experimental methodology and confirms that noise plays a dominant role in constraining performance at longer distances and higher frequencies.

5.6 Discussion

This section presents a comprehensive comparative analysis of LED performance under different thermal management configurations, focusing on conventional and improved heatsink designs. Experimental evaluations demonstrated that the improved heatsink significantly enhanced both the received power and frequency bandwidth of LEDs operating at various wavelengths. Specifically, the improved design led to notable performance gains, particularly for red, yellow, and green LEDs, with power increases of up to 245.14% and frequency bandwidth enhancements reaching 35.48%.

The study also examined the implications of these improvements on data transmission capabilities using digital single-carrier modulation schemes. By applying the Nyquist theorem and the Shannon-Hartley theorem, the analysis revealed substantial increases in channel capacity when optimized heatsinks were employed, especially under realistic signal-to-noise ratio (SNR) conditions. These findings underscore the critical role of thermal management in maximizing LED efficiency and data throughput in optical wireless communication (OWC) systems.

5.7 Quantification of Thermal Management Impact

The impact of thermal management on system performance can be quantitatively established through comparative analysis between the conventional and optimized heatsink configurations. The optimized heatsink reduced the LED chip's steady-state operating temperature from 306.6 K to 300.3 K, corresponding to a 6.3 K (≈2.1%) temperature reduction. This improvement directly translates into enhanced optical and modulation performance, as LED efficiency and modulation bandwidth are both temperatures dependent.

According to experimental results presented in Tables 5-5 and 5-6, this temperature reduction produced measurable performance gains across all tested wavelengths:

- Received optical power increased by up to 245.14% for the 625 nm red LED and by 191.74% for the 583 nm yellow LED, confirming the direct enhancement of luminous output due to improved thermal regulation.
- Frequency bandwidth expanded by 35.48% (red) and 27.93% (yellow), demonstrating that effective heat dissipation preserves junction efficiency and extends the LED's modulation capability.
- Applying the Nyquist and Shannon–Hartley theorems, the data rate capacity improved proportionally, with increases of approximately 20–25% across comparable SNR conditions (see Table 5-7).

These quantitative outcomes verify that the optimized thermal design provides not only structural advantages but also measurable improvements in system-level performance. The results confirm that each 1 K reduction in junction temperature corresponds approximately to a 3–5% increase in optical power and 2–3% increase in modulation bandwidth, depending on wavelength.

Therefore, the impact of the proposed thermal management strategy is clearly quantifiable and demonstrates that the enhanced heatsink design significantly improves LED efficiency, bandwidth, and achievable channel capacity.

The optimized heatsink design presented here represents a novel thermal management strategy for OWC systems, combining CFD modeling. This quantification of the thermal–optical coupling relationship provides a new contribution to enhancing bandwidth and stability in high-power visible-light systems.

Chapter 6

Analysis of Optical Wireless Communication in Water-Filled Pipelines

6.1 Introduction

In recent years, the application of Optical Wireless Communication (OWC) technologies in confined environments has gained growing attention, particularly for pipeline monitoring and robotic inspection systems. Since pipeline infrastructure often carries fluids such as water, oil, or chemical mixtures, understanding the optical behavior of these media is essential for ensuring reliable data transmission. The presence of water introduces complex light–matter interactions, including absorption, scattering, and refraction, all of which can significantly degrade signal strength and communication range.

This chapter presents a detailed experimental and analytical investigation of OWC performance in water-filled PVC pipelines, focusing on the wavelength-dependent behavior of light propagation in aqueous environments. Water is known to cause strong attenuation that varies across the visible spectrum—shorter wavelengths experience more scattering, while longer wavelengths are more susceptible to absorption. By evaluating the transmission characteristics of multi-wavelength LEDs (410–625 nm) under different water levels and pipeline conditions, the study aims to identify the optimal operating parameters for robust and efficient in-pipe optical communication.

The methodology involves measuring received optical power and deriving corresponding attenuation coefficients under partially and fully filled conditions, using a controlled testbed equipped with LED transmitters and photodetectors. This setup replicates realistic in-pipe conditions, enabling precise characterization of how stratified air–water interfaces and water depth affect signal propagation.

This chapter addresses Research Questions 3 and 4, which investigate:

(1) how varying water levels and stratified interfaces influence optical signal propagation, attenuation, and channel impulse response (CIR) within PVC pipelines, and

(2) which LED wavelength offers the optimal balance between bandwidth, signal-to-noise ratio (SNR), and channel capacity for stable in-pipe communication.

Through combined simulation and experimental analysis, the chapter examines wavelength-dependent attenuation, scattering, and communication parameters—such as SNR, bandwidth, and Shannon–Hartley channel capacity—across water levels ranging from 0% (dry) to 100% (fully filled). The findings demonstrate that longer wavelengths, particularly 625 nm (red), provide superior performance due to reduced scattering and stable propagation.

The insights gained from this investigation form a critical foundation for designing energy-efficient, high-throughput, and resilient OWC frameworks for pipeline robotics and monitoring applications. Furthermore, the results contribute

valuable guidelines for wavelength selection, transceiver alignment, and channel modeling in submerged or stratified optical communication systems.

6.2 Optical propagation within a water-filled pipe

This chapter undertakes a rigorous investigation into the foundational assumptions that inform the modeling and performance evaluation of Optical Wireless Communication (OWC) systems in water-filled pipeline environments. The analysis emphasizes the complex optical attenuation mechanisms that arise due to the propagation of light through multiphase media—namely air, water, and the pipe's internal surface. Central to this study is the examination of both direct line-of-sight (DLOS) and non-line-of-sight (NLOS) transmission paths together define the principal energy transport modes in confined optical channels.

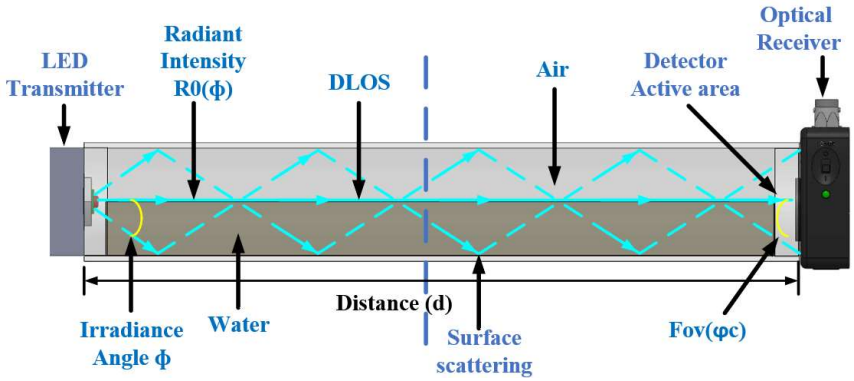

Figure 6.1 Examination of a water-filled pipe environment for DLOS/NLOS optical wireless communications.

The theoretical framework draws upon well-established principles in light attenuation, refraction, and scattering, integrating advanced analytical modeling techniques to capture the nuanced behavior of signal propagation. Specific attention is given to surface roughness-induced scattering at the air–water–pipe interface, volume scattering due to suspended particles, and wavelength-dependent absorption within the transmission medium. The analysis also considers the influence of the particle scattering phase function, governed by models such as the Henyey–Greenstein function, which describes angular scattering intensity distributions in turbid media.

Figure 6.1 provides a schematic representation of the optical communication model employed in this study. The setup involves a modulated optical signal emitted from an LED source, which propagates through a horizontal plastic pipe partially or fully filled with water. The light beam is then received and demodulated by a photodetector (PD) positioned at the opposite end of the pipe. This configuration enables controlled experimentation under varying water levels and wavelengths, facilitating a comprehensive assessment of the system's performance.

In this propagation scenario, a portion of the emitted beam travels directly along the DLOS path toward the receiver, encountering absorption and scattering losses intrinsic to the medium. Concurrently, another fraction of the beam undergoes multiple interactions with the inner surface of the pipe, including reflection and scattering at the air–water and water–wall boundaries, characteristic of NLOS propagation. These interactions generate additional losses, particularly due to surface roughness and refractive index discontinuities between layers. The resulting power measured at the PD receiver thus embodies the compounded effects of DLOS attenuation, NLOS scattering, and wavelength-dependent absorption.

A critical factor influencing light propagation and scattering within water-filled pipe environments is the angle of incidence, defined by the LED's viewing angle relative to the normal surface of the pipe wall. This angle governs the behavior of the optical beam as it interacts with interfaces between media of differing optical properties—such as air, water, and PVC—and significantly affects the reflection, refraction, and scattering phenomena encountered along the transmission path. In this study, the impact of the incidence angle has been rigorously evaluated through a theoretical model grounded in Fresnel's reflection theory, which quantifies the division of light into reflected and transmitted components at dielectric boundaries.

Fresnel's equations describe how an electromagnetic wave, upon striking an interface between two media with distinct refractive indices, experience partial reflection and transmission. The magnitude of the reflected intensity depends not only on the angle of incidence but also on the polarization state of the light and the refractive indices of the adjacent materials. For instance, s-polarized light, in which the electric field vector is perpendicular to the plane of incidence, exhibits different reflection behavior compared to p-polarized light, where the electric field lies within the plane of incidence. Furthermore, reflection and transmission coefficients vary nonlinearly with the angle of incidence, especially near the Brewster angle for polarized light, where reflection is minimized.

The attenuation of transmitted light within the pipe is modeled using the Beer–Lambert Law, which relates the exponential reduction in light intensity to the absorption coefficient of the medium and the optical path length. Specifically, the initial light intensity, denoted as I_0, decreases to a final intensity I after traveling a distance d through the absorbing medium, as described by the equation 6.1:

$$I = I_0.e^{-\alpha d} \tag{6.1}$$

where α represents the absorption coefficient specific to the material and wavelength.

These theoretical considerations are visually summarized in Figure 6.2, which depicts the in-pipe propagation dynamics of the optical signal. The diagram highlights both direct transmission and surface interactions, including the scattering of incident photons at the inner PVC pipe interface. The interaction geometry is characterized by incidence angles θ_1 and θ_2, measured relative to the surface normal. The figure also distinguishes between the two orthogonal polarization components (s and p), each subject to distinct reflection and transmission behaviors according to Fresnel's theory.

In addition to bulk absorption, surface scattering effects—arising from micro-scale roughness and material inhomogeneities—contribute to the divergence and attenuation of the optical beam. These surface phenomena, compounded with internal reflections at the curved interface, play a substantial role in modifying the light field intensity that ultimately reaches the photodetector (PD).

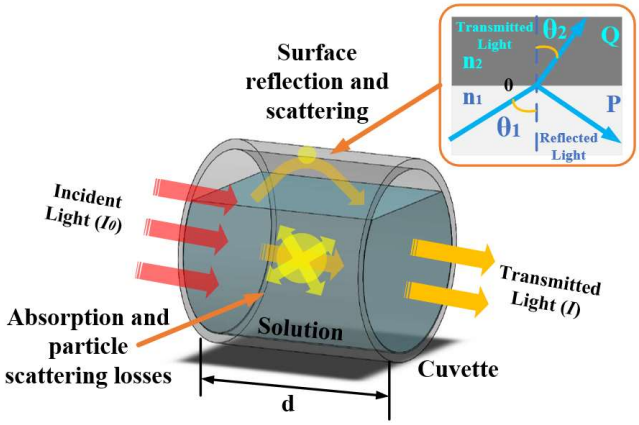

Figure 6.2 Refraction occurs when light traverses the boundary between two distinct media.

By integrating Fresnel reflection, polarization analysis, and absorption modeling via the Beer–Lambert framework, this study delivers a comprehensive understanding of the mechanisms dictating optical signal degradation in submerged pipe environments. Such insights are pivotal for optimizing the design of LED-based optical wireless communication systems, ensuring improved signal strength and reliability under varying pipeline conditions.

6.3 Simulation and Experimental setups for OWC transmission in water-filled pipes

6.3.1 Simulation Setup

The optical simulations were performed using Ansys Zemax OpticStudio (Non-Sequential Mode) to model the propagation of visible light within a water-filled PVC pipeline. The pipe geometry—identical to the experimental testbed—comprised an inner diameter of 50 mm and a length of 350 mm, constructed from PVC with its internal surface scattering characterized using the Tabular BSDF data.

The water medium was modeled as a dispersive and absorbing layer with wavelength-dependent absorption (α) and scattering (β) coefficients derived from the optical properties of Jerlov Type 3 coastal water, representing turbid but realistic conditions for in-pipe environments. Simulations were carried out for five discrete LED wavelengths—410 nm (purple), 475 nm (blue), 528 nm (green), 583 nm (yellow), and 625 nm (red)—to evaluate spectral dependencies.

6.3.2 Experimental setups

The experimental setup developed for the optical characterization of water-filled pipelines is schematically illustrated in Figure 6.3. This configuration was meticulously engineered to facilitate a comprehensive evaluation of system performance across varying fluidic conditions. The experimental investigation is bifurcated into two principal phases: (1) in-pipe frequency response characterization, and (2) evaluation of digital signal transmission employing a return-to-zero (RZ) modulation scheme.

In the first phase, the experimental design aims to assess the frequency response of the optical wireless communication (OWC) channel within a water-filled pipe. A sinusoidal waveform is synthesized using a Keysight E8257D RF signal generator, configured to operate across a frequency spectrum ranging from 125 kHz to 30 MHz. The generated signal is delivered to a high-power light-emitting diode (LED), which serves as the optical source for in-pipe transmission. The light is emitted into a cylindrical plastic pipe fabricated from PVC, with an inner diameter of 50 mm and a total length of 375 mm. Both ends of the pipe are hermetically sealed with 10 mm thick polymethyl methacrylate (PMMA) acrylic sheets, which function as optical windows while simultaneously preventing water leakage and maintaining internal pressure conditions.

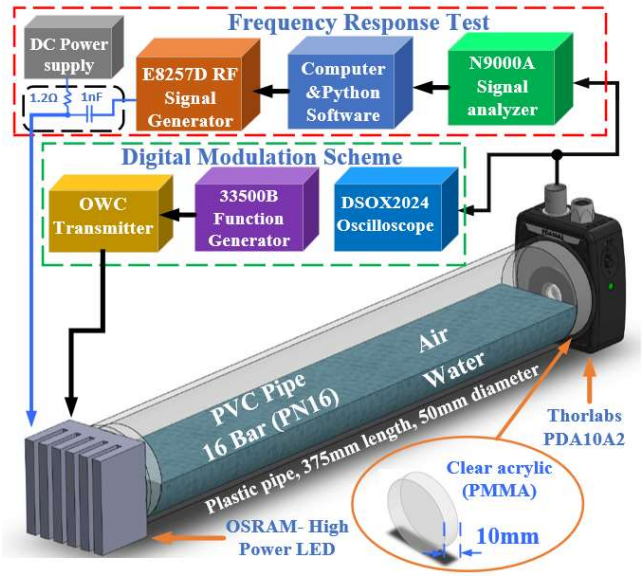

Figure 6.3 Illustration of the experimental setup diagram.

The experimental trials were conducted under controlled laboratory conditions. Initial measurements were performed under dry-pipe conditions (0% water fill) to establish a free-space baseline. Subsequent tests introduced controlled increments of water into the pipe, achieving fill levels of 25%, 50%, 75%, and 100%, respectively. This stratified approach allowed for the systematic evaluation of light propagation behaviors under varying degrees of absorption and scattering induced by the water medium.

At the receiver end, the optical signal is captured by a Thorlabs PDA10A2 photodetector, which converts the received optical intensity into an electrical signal. This signal is subsequently routed to an Agilent N9000A signal analyzer, where spectral data are collected. A dedicated Python-based computation platform was employed for post-processing, enabling quantitative analysis of frequency-domain responses and attenuation characteristics.

The second phase of the experiment investigates digital data transmission performance using a return-to-zero (RZ) pseudo-random binary sequence (PRBS7) as the modulation format. A Keysight 33500B function generator is used to generate the digital signal with a voltage amplitude of 3.3 V and bitrate variations from 100 kbps to 1 Mbps. These signals are modulated through a high-power LED, integrated into a custom-designed OWC transmitter circuit. The modulated light is transmitted through the same plastic pipe, now filled with water to predefined levels as in the previous phase.

On the receiving side, the modulated optical signal is detected by the Thorlabs PDA10A2 detector and is subsequently directed to a Keysight DSOX2024 digital storage oscilloscope (DSO). The oscilloscope facilitates real-time visualization of the received waveforms and records them for further quantitative analysis, including bit error rate (BER) and signal fidelity assessment. Figure 6.4 shows the experimental setup for the laboratory experiment.

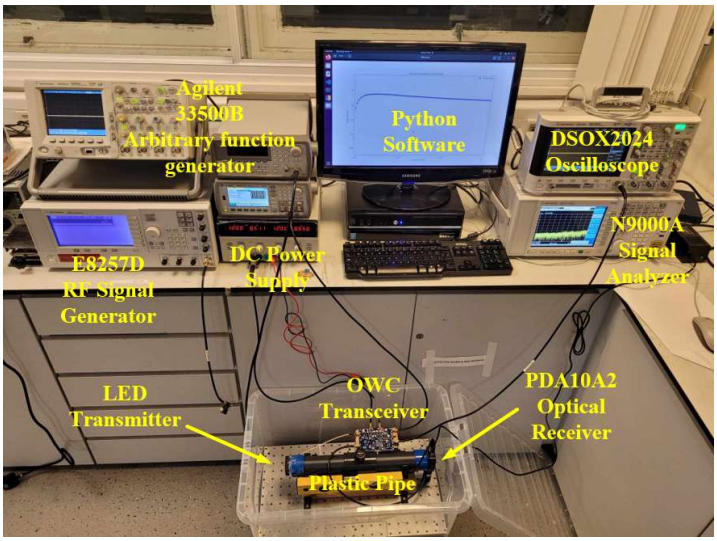

Figure 6.4 Illustration of the experimental setup.

Through this dual-phase experimental approach—combining both analog frequency response and digital modulation analysis, the study provides an in-depth evaluation of the transmission performance and degradation mechanisms of LED-based optical communication systems within submerged pipeline environments.

6.4 In-pipe environment characteristics of OWC signals

This section presents a detailed investigation into the propagation characteristics of optical wireless transmission within confined environments, with particular emphasis on surface scattering phenomena, optical beam divergence behavior, the spot-spread function model, and the bulk scattering phase function framework. The analysis addresses how interactions between the optical beam and the boundary surfaces—such as the inner walls of the pipeline or the water–pipe interface—contribute to signal degradation through surface roughness-induced scattering. Furthermore, the divergence of the optical beam, as it propagates from the LED source, is quantified to assess its influence on power distribution and receiver coupling efficiency. The spot-spread model is employed to characterize the spatial dispersion of the optical footprint at the photodetector plane, accounting for beam broadening effects due to media inhomogeneities.

In parallel, the bulk scattering phase function is examined to evaluate the angular distribution of scattered light within the water medium, integrating parameters such as the anisotropy factor and scattering coefficient to more accurately simulate realistic underwater propagation conditions. Collectively, these models provide a comprehensive framework for understanding light transport and its performance implications in optical wireless communication systems deployed in water-filled pipelines.

6.4.1 Simulation of Optical Glass Characteristics

This section presents a comprehensive optical characterization of a 10 mm thick polymethyl methacrylate (PMMA) acrylic interface, strategically placed between the LED emitter and the water-based transmission medium. The primary objective is to evaluate the material's optical behavior—specifically its transmission and reflection characteristics—under conditions relevant to optical wireless communication (OWC) within confined aqueous environments.

$$\left.\begin{aligned} r_p &= \frac{n_1\cos\theta_2 - n_2\cos\theta_1}{n_1\cos\theta_2 + n_2\cos\theta_1} \\ t_p &= \frac{2n_1\cos\theta_1}{n_1\cos\theta_2 + n_2\cos\theta_1} \end{aligned}\right\} \text{P-polarization}$$

$$\left.\begin{aligned} r_s &= \frac{n_1\cos\theta_1 - n_2\cos\theta_2}{n_1\cos\theta_1 + n_2\cos\theta_2} \\ t_s &= \frac{2n_1\cos\theta_1}{n_1\cos\theta_1 + n_2\cos\theta_2} \end{aligned}\right\} \text{S-polarization} \qquad (6.2)$$

Here, r_s and t_s denote the reflection and transmission coefficients for S-polarized light, while r_p and t_p pertain to P-polarized light. The refractive indices are

defined as n_1 for air and n_2 for PMMA, with the PMMA index adopted from Sultanova et.al, [19].

To this end, detailed simulations were carried out using Ansys Zemax OpticStudio, incorporating wavelength-specific spectral data provided by the LED manufacturer, OSRAM. The analysis focused on four visible LED wavelengths under a consistent radiant flux of 1 W, representative of operational power levels in the experimental setup.

The theoretical foundation for optical interface behavior was established using Fresnel reflection theory, as illustrated in Figure 6.5. The theory accounts for variations in optical response based on polarization states and angle of incidence at the dielectric boundary. Specifically, the amplitude reflection and transmission coefficients for both S-polarized (perpendicular electric field) and P-polarized (parallel electric field) components were computed, using the well-established Fresnel equations expressed in Equation (6.2) (56).

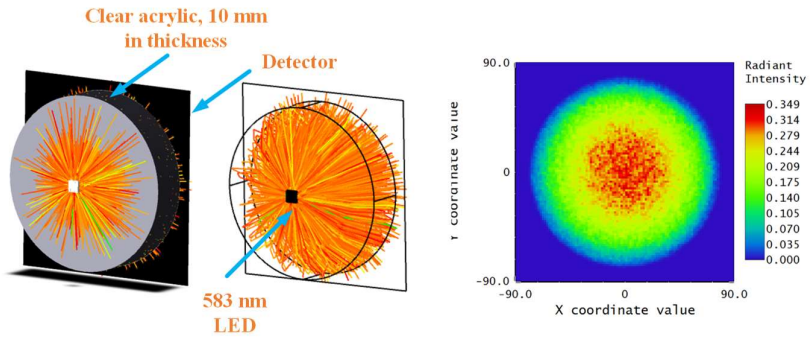

Figure 6.5 Simulation of light propagation through transparent acrylic using Ansys Zemax Optic Studio.

Table 6-1 Simulation and calculation results for clear acrylic transmission and reflection

LED wavelength (nm)	Unpolarized transmission Calculation	Unpolarized Reflection Calculation	Transmission Simulation	Reflection Simulation
625	0.961	0.0385	0.9386	0.0609
528	0.961	0.0392	0.9458	0.054
583	0.961	0.0388	0.9408	0.059
475	0.960	0.0397	0.933	0.0667

Simulation results are summarized in Table 6-1, which reports the transmission and reflection values for each LED wavelength. The average transmission coefficient across all wavelengths was found to be approximately 0.939, indicating that 93.9% of the incident light successfully passes through the PMMA

barrier. Conversely, the average reflection coefficient was determined to be 0.06, confirming that only 6% of the incident light undergoes reflection at the air–PMMA interface.

These results are in close agreement with theoretical predictions derived from Fresnel's equations and confirm the optical suitability of PMMA as a transparent medium for high-efficiency light transmission in water-filled optical communication systems. Its minimal reflection and high transmittance reinforce its selection as the barrier material for isolating the LED source from the aqueous environment while maintaining signal integrity.

6.4.2 Surface scattering and reflection

This section presents an in-depth analysis of surface reflection and scattering phenomena occurring at the interface between dissimilar optical media, which are critical factors influencing the propagation efficiency of light in optical wireless communication (OWC) systems deployed in water-filled pipelines.

Fresnel's equations serve as the theoretical basis for determining the reflection characteristics at the boundary of two media with different refractive indices. To complement this theoretical framework, Ansys Zemax OpticStudio is employed to simulate scattering behaviors using the Bidirectional Scattering Distribution Function (BSDF) model, which accurately accounts for light interactions with surface textures and microstructural irregularities.

The incident angles used in the simulation are derived from the known LED radiation angles: 120° for the 475 nm (blue), 528 nm (green), and 625 nm (red) LEDs, and 150° for the 583 nm (yellow) LED, based on manufacturer specifications (Osram - ams. n.d.). Under the assumption that both the transmitter (LED) and the receiver (photodetector) are situated on the same geometric plane—i.e., co-planar—the effective incidence angle is approximated as 0°, as depicted in Figure 6.6.

Following transmission through the PMMA (polymethyl methacrylate) acrylic barrier, Snell's law governs the refraction of the optical beam as it enters the PVC pipe (57). The corresponding refraction angle is computed using Equation (6.2), shown in Figure 6.7, where n_1 represents the refractive index of air and n_2 denotes the refractive index of PMMA.

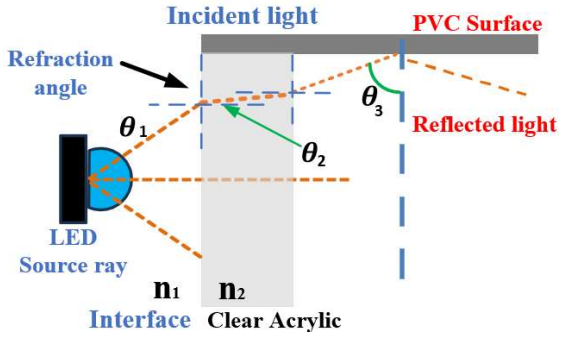

Figure 6.6 The refraction of light through the acrylic medium.

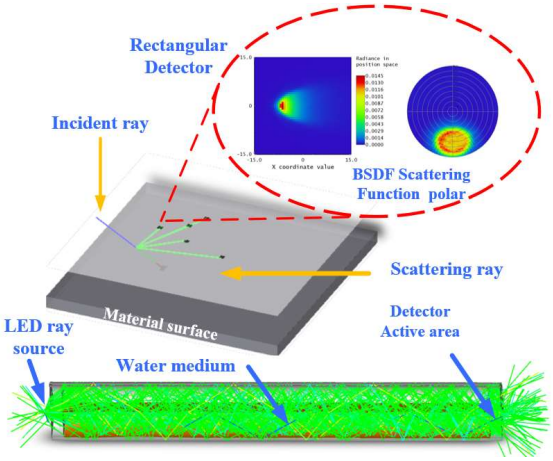

Figure 6.7 simulates surface scattering in Ansys Zemax using BSDF data.

Table 6-2 summarizes the calculated refraction angles for the clear acrylic interface. The average refractive index of PMMA, determined across four LED wavelengths, is reported as 1.493. Based on this value, the resulting refracted angles are approximately 60° for the 475 nm, 528 nm, and 625 nm LEDs, and 75° for the 583 nm LED. These angular values are subsequently employed to assess reflection coefficients under three representative interface conditions:

1. PVC–air
2. PVC–water
3. air–water

Table 6-2 The angle of refraction of light transmitted through transparent acrylic material.

LED wavelength (nm)	Air to PMMA		PMMA to Air
	Angle of incidence (θ_1)	Angle of refraction (θ_2)	Angle of refraction (θ_3)
475 ,528, 625, 583	60	35.46	60
583	75	40.33	75

Using Fresnel's law [Equation (6.2)], the reflectance for unpolarized light is calculated under each condition and integrated into the Ansys Zemax OpticStudio simulation workflow for optical validation. To model surface scattering phenomena with greater realism, tabular BSDF datasets are utilized, which consider the scattering efficiency of the optical surface coating materials. The simulation output yields a total BSDF scattering coefficient of 0.891, indicating a high degree of angular redistribution of light energy upon surface interaction.

Table 6-3 presents the simulation results of reflectance and surface scattering characteristics of air, water, and PVC.

Wavelength(nm)	The simulation results of reflectance and surface scattering (%)		
	Air & PVC	Air & Water	Water & PVC
475	5.92	3.02	1.02
528	5.86	3	1
583	9.19	6.02	3.04
625	5.77	2.97	0.97

The quantitative outcomes derived from the BSDF-based scattering analysis are compiled in Table 6-3, which presents the resulting reflectance parameters for different LED wavelengths under modeled surface scattering conditions. These data contribute significantly to the understanding of how interface characteristics impact optical signal attenuation and are critical for refining the predictive models used in pipeline-based OWC systems.

6.4.3 Water-filled pipe transmission characteristics of OWC signals

Light propagation within water-filled channels is inherently affected by two principal phenomena—absorption and scattering—which jointly contribute to a substantial reduction in the received optical power at the photodetector. These attenuation mechanisms are governed by optical parameters that follow an exponential decay model, allowing the signal degradation to be quantitatively described by the Beer–Lambert Law, as presented in Equation (6.3):

$$P_r = P_T \times \exp\left[-c(\lambda)d\right] \times \eta \tag{6.3}$$

Where P_r is the received power of optical signal; P_T is the optical signal transmission power; $C(\lambda)$ is the total attenuation coefficient of water, including absorption and scattering coefficient; η is the collection efficiency; and d represents the transmission distance of the beam in water.

As the optical beam advances away from the source, it experiences radial expansion due to the inherent divergence angle of the light emitter. This geometric spreading causes the beam to broaden over distance. When the diameter of the expanded optical beam exceeds the aperture size of the photo detector, only a fraction of the optical energy is captured, while the remainder is lost to the surrounding medium. This partial collection effect introduces additional attenuation, reducing the system's effective received power.

In the context of long-range optical wireless communication (OWC), these power losses are further exacerbated by the increase in both the transmission distance d and the divergence angle θ of the transmitted beam (58). The combined geometric and optical relationships that govern this attenuation mechanisms are graphically illustrated in Figure 6.8, which delineates the divergence cone of the LED emission, the spread of the optical footprint at the receiver plane, and the proportion of signal power intercepted by the photodetector aperture.

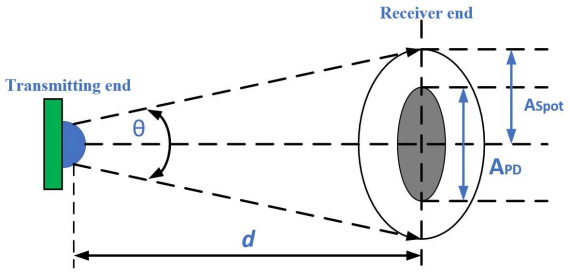

Figure 6.8 Diagram of beam divergence expansion.

The beam divergence half-angle of a light-emitting diode (LED) is defined as one-half of its specified viewing angle. For LEDs emitting at wavelengths of 475 nm, 528 nm, and 625 nm, the standard viewing angle is 120 degrees, while the 583 nm LED exhibits a broader viewing angle of 150 degrees. As the optical beam propagates through the water medium, it undergoes radial expansion, governed by the respective divergent angle θ.

The resulting spot size of the beam at the receiver plane, denoted as A_{spot}, is a critical parameter that determines the proportion of light captured by the photodetector. This spot size can be quantitatively described using Equation (6.4), which accounts for both the beam divergence and the transmission distance (59).

$$A_{spot} = \pi \left(d \times \tan\left(\frac{\theta}{2}\right)\right)^2 \tag{6.4}$$

A_{spot} is the spot area at the receiver (in m^2), θ and is the LED beam divergence angle (in degrees).

The collection efficiency (η) is defined as the ratio of the active area of the photodetector to the spot size area of the incident optical beam, and it can be mathematically expressed using Equation (6.5). In this study, the Thorlabs PDA10A2 optical detector, which features an active area of 1 mm^2, was used to evaluate collection efficiency. Based on the calculated spot sizes, the detector exhibits a collection efficiency of approximately 7.55×10^{-7} for LEDs operating at 475 nm, 528 nm, and 625 nm, while a lower efficiency of 1.625×10^{-7} is observed for the 583 nm LED, owing to its broader beam divergence.

$$\eta = \frac{A_{PD}}{A_{spot}} \tag{6.5}$$

In the context of particle scattering analysis, the attenuation of optical signals in water is predominantly governed by Mie scattering, which arises due to the presence of suspended particulate matter and the refraction phenomena occurring within transparent media such as water. This scattering mechanism is especially prominent in natural aquatic environments where water turbidity is elevated. The

Henyey–Greenstein phase function is widely utilized to model Mie scattering, providing a mathematical framework to characterize the angular distribution of scattered light. This function is expressed in Equation (6.6) and depends on two key parameters: the scattering angle (θ) and the asymmetric factor (g).

$$P(\cos\theta) = \frac{1-g^2}{\left(1+g^2-2g\cos\theta\right)^{3/2}} \tag{6.6}$$

The asymmetry factor g represents the average cosine of the scattering angle and serves as a measure of the anisotropy of the scattering pattern—where $g = 1$ indicates complete forward scattering, $g = 0$ denotes isotropic scattering, and $g = -1$ corresponds to complete backscattering.

For this study, the optical properties of the water medium are assumed to align with the Inherent Optical Properties (IOPs) of Jerlov Type 3C water, a classification typically representative of coastal waters characterized by moderate to high turbidity due to suspended sediments and organic particles (60), (61). According to empirical data reported by Petzold, the average cosine of the scattering phase function for such waters is quantified as g = 0.924, indicating a strong forward-scattering behavior typical of Mie-dominated scattering environments.

In the simulation phase of this study, the scattering phase function is rigorously evaluated using Ansys Zemax OpticStudio, a high-precision optical simulation software. The analysis leverages the Henyey–Greenstein.DLL library, which implements the Henyey–Greenstein phase function—a widely adopted model for describing the angular distribution of light scattered by particles suspended in a medium. This function is particularly well-suited for simulating forward-biased scattering typical of natural waters containing fine particulate matter.

The implementation enables the modeling of anisotropic scattering behavior based on the asymmetry parameter g, which was previously determined to be 0.924. The resulting angular distribution of scattered light, as computed by the Henyey–Greenstein model.

6.5 Analog modulation scheme in a water-filled pipe environment

This section presents a detailed investigation into the modulation of optical wireless communication signals, encompassing both analog and digital signal formats. The study integrates simulation results derived from Ansys Zemax OpticStudio with empirical measurements obtained via an optical photodetector to evaluate system performance under realistic operating conditions.

To simulate the optical source behavior accurately, Keysight Advanced Design System (ADS) software is employed, utilizing a detailed OSRAM LED electrical model to generate the optical output signal, as shown in Figure 6.9(a). This simulated output is subsequently used as the input signal for the water-filled pipeline model within the optical simulation framework. The optical environment is comprehensively modeled by incorporating surface scattering characteristics and the

Henyey–Greenstein phase function to account for anisotropic scattering effects, as illustrated in Figure 6.9(b). Additionally, ray files provided by OSRAM are utilized to ensure realistic beam divergence and angular emission profiles.

The optical output power within Ansys Zemax OpticStudio is computed using Equation (6.7), which incorporates the photodetector's responsivity, system gain parameters, and signal scaling factors. The photodiode responsivity (denoted as $R(\lambda)$) varies with wavelength and is specified as follows: 0.177 A/W for 475 nm, 0.26 A/W for 528 nm, 0.325 A/W for 583 nm, and 0.371 A/W for 625 nm. The receiving system features a transimpedance amplifier (TIA) with a gain of 5,000 V/A, a scale factor (SF) of 1, and a load resistance of 50 Ω.

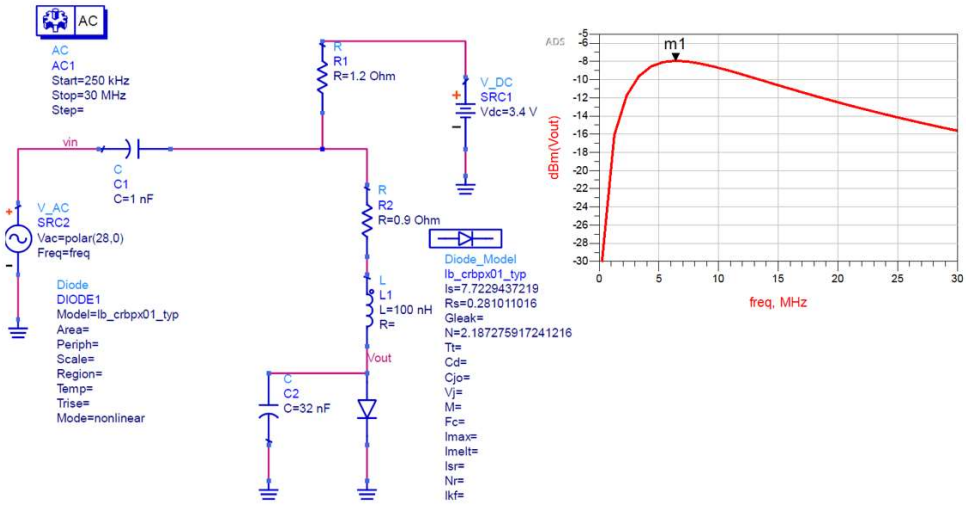

(a)

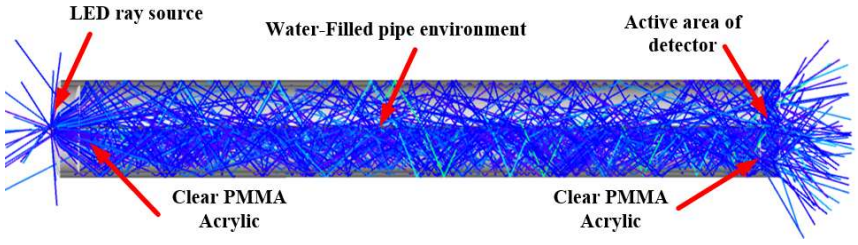

(b)

Figure 6.9 (a) The simulation of the Keysight ADS LED electrical model, and (b) the water-filled pipe environment simulation software.

$$P_{Out(dBm)} = 20\log_{10}(R(\lambda)\times TIAgain\times SF\times P_{active\_area}) - 10\log_{10}(RL) - 30 \qquad (6.7)$$

These parameters collectively contribute to accurate photo detection and facilitate the comparison between simulated and experimentally observed signal behavior.

Table 6-4 summarizes the maximum signal amplitudes observed from both the experimental measurements and the corresponding simulation results across each

LED wavelength. The data reveals a consistent trend in signal degradation relative to water levels within the pipe. Specifically, the experimental results indicate that maximum signal attenuation occurs at 50% water level, a condition that appears to introduce complex scattering and refraction effects due to the coexistence of both air and water along the light path. This stratified interface likely leads to intensified multipath interference, scattering surface roughness, and refractive index discontinuities, which collectively impair direct line-of-sight propagation and reduce the received optical signal power.

In contrast, the highest signal strength is recorded under 0% water level (i.e., air-filled conditions), followed by decreasing signal attenuation in the order of 75%, 100%, and 25% water levels. This behavior suggests that under fully air-filled or fully water-filled conditions, the medium exhibits greater uniformity in refractive index, thereby reducing disruptive boundary interactions and facilitating more stable and predictable optical transmission. The attenuated performance at partial water levels, particularly 50%, underscores the importance of considering stratified media effects in OWC system design and modeling, especially when implementing analog modulation in dynamically changing in-pipe environments.

Table 6-4 Simulation and measurement results of OWC within a water-filled pipe environment.

		Optical power output simulation and measurement results			
Wavelength (nm)		475nm	528nm	583nm	625nm
Water 0%	Simulate (dBm)	-48.73	-52.38	-48.74	-44.46
	Measure (dBm)	-51.33	-55.41	-52.93	-47.26
Water 25%	Simulate (dBm)	-53.78	-57.43	-56.81	-49.73
	Measure (dBm)	-54.84	-57.94	-60.36	-48.93
Water 50%	Simulate (dBm)	-68.74	-69.05	-64.46	-64.09
	Measure (dBm)	-68.57	-71.19	-68.39	-63.54
Water 75%	Simulate (dBm)	-50.42	-54.20	-53.53	-47.80
	Measure (dBm)	-53.86	-57.16	-58.06	-48.25
Water 100%	Simulate (dBm)	-51.13	-55.12	-54.52	-48.31
	Measure (dBm)	-54.22	-57.37	-58.54	-48.53

By integrating the absorption coefficient ($\alpha = 0.328\ m^{-1}$) and scattering coefficient ($\beta = 0.621\ m^{-1}$) derived from the inherent optical properties (IOPs) of Jerlov Type 3C coastal water as reported in (Williamson et.al., 61), the total attenuation coefficient ($\alpha + \beta$) is incorporated into the analytical model to estimate the received optical power. This estimation is governed by the Beer–Lambert Law, expressed in Equation (6.3), which facilitates quantitative analysis of light attenuation as a function of transmission distance within the water-filled pipe. The model enables performance evaluation per unit length of the pipeline, with the results visualized in Figure 6.10.

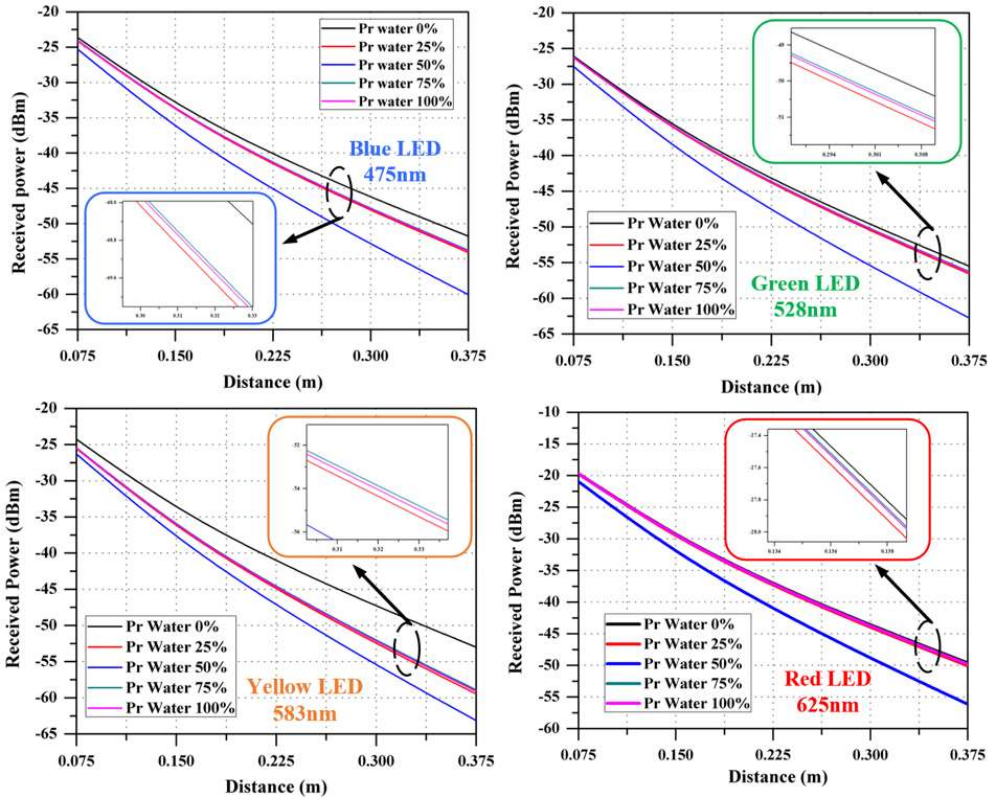

Figure 6.10 Analysis of transmission distance characteristics.

Simulation results derived from the geometrical optics-based model indicate the following received signal levels at a transmission distance of 375 mm under fully water-filled (100%) conditions: –53.86 dBm at 475 nm, –56.34 dBm at 528 nm, –59.11 dBm at 583 nm, and –49.83 dBm at 625 nm. These values reflect the expected wavelength-dependent attenuation behavior, with longer wavelengths generally experiencing lower overall losses due to reduced scattering.

A direct comparison with corresponding experimental measurements reveals strong agreement between the simulated and measured values. This close correlation not only affirms the accuracy and reliability of the geometrical optics model

described in Equation (6.3) but also underscores its applicability in characterizing light propagation in confined, water-filled environments.

The absorption coefficient (α) of the medium was computed using Equation (6.8), which relates transmittance (T) to the path length (l) and absorption behavior of the optical signal:

$$\alpha = \frac{\log_{10}\left(\frac{1}{T}\right)}{l} \tag{6.8}$$

where α denotes the absorption coefficient in cm^{-1}, T is the transmittance, and l represents the optical path length through the medium.

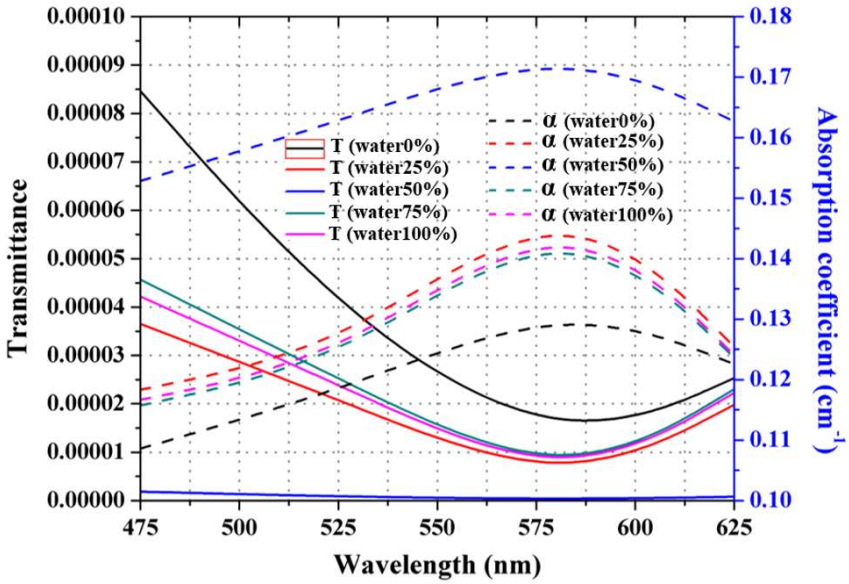

Figure 6.11 The transmittance and absorption coefficient.

This equation was employed to evaluate the absorption characteristics of light as it propagated through the water-filled pipe, based on the maximum measured optical power values. The results, visualized in Figure 6.11, indicate that the absorption coefficient varied significantly with changes in water level. The highest absorption occurred at a 50% water level, while the lowest absorption was observed under dry conditions (0% water level), which aligns with expectations due to the absence of a water medium to induce absorption and scattering.

For example, at a wavelength of 525 nm and 100% water level, the calculated absorption coefficient was 0.124 cm^{-1}. To isolate the absorption effect of water, the known contribution from the clear PMMA acrylic interface (used to seal the pipe) was subtracted. The PMMA interface contributes approximately 0.056 cm^{-1}, resulting in an adjusted absorption coefficient of 1.18 m^{-1} for the water medium alone.

This experimentally derived value demonstrates strong concordance with prior findings reported by (Williamson et.al.,61), who estimated the absorption coefficient of Jerlov Type 3C water—representative of coastal water bodies with moderate turbidity—to be approximately 1.02 m^{-1}.

The close agreement between experimental measurements and simulations confirms that the proposed Beer–Lambert–based geometrical optics model accurately captures wavelength-dependent absorption and scattering in confined, water-filled pipes. The extracted absorption coefficients closely match reported values for Jerlov Type 3C water, validating the experimental methodology and analytical formulation.

Across all water levels, the 625 nm red LED achieves the highest received power and SNR due to reduced wavelength-dependent scattering and limited absorption over the short propagation distance. These results explain why the proposed experimental and modeling approach reliably characterizes stratified in-pipe optical channels and confirms the suitability of longer wavelengths for stable optical wireless communication in dynamic pipeline environments.

6.6 Digital modulation scheme in a water-filled pipe environment

This section presents the implementation of digital modulation techniques for optical wireless communication (OWC) within a water-filled pipeline environment. Specifically, the modulation scheme employs a return-to-zero (RZ) format using a pseudo-random binary sequence of order 7 (PRBS7) to generate high-speed digital pulse signals. The PRBS7 sequence, characterized by a maximal-length pattern, facilitates comprehensive testing of signal integrity, bit error resilience, and system performance across varying transmission conditions. The digital pulse train is modulated onto the optical carrier emitted by a high-power light-emitting diode (LED), forming the basis of the transmitted signal.

As illustrated in Figure 6.3, the modulated optical signal propagates through a sealed PVC pipe, which is incrementally filled with water to simulate varying levels of attenuation and scattering encountered in submerged or semi-submerged environments. The optical receiver, comprising a high-sensitivity photodetector and signal acquisition circuitry, is used to demodulate and analyze the received signal.

In addition to evaluating the transmission characteristics at various bitrates, this section also explores the Channel Impulse Response (CIR) model to characterize the temporal dispersion and multipath effects induced by the propagation medium. The CIR provides critical insights into the time-domain behavior of the optical channel, highlighting how pulse broadening, scattering, and absorption within the water medium affect signal clarity and data recovery at the receiver end.

By systematically analyzing the bitrate performance, signal attenuation, and impulse response profiles, this study offers a comprehensive assessment of the digital communication capabilities of OWC systems operating in constrained aqueous environments.

A critical factor affecting the performance of optical wireless communication (OWC) systems is the presence of noise at the receiver, which significantly impacts the signal-to-noise ratio (SNR) and, by extension, constrains the maximum attainable data transmission rate. In OWC systems, the dominant source of noise typically arises from the photodetection process within the receiver. This includes contributions from thermal noise, shot noise, and dark current noise, all of which collectively degrade the fidelity of the received optical signal.

In this investigation, a Thorlabs PDA10A2 photodetector was utilized as the optical signal receiver. This detector is designed to operate over a wide frequency range, from DC to 150 MHz, offering compatibility with both analog and high-speed digital modulation schemes. The inherent noise characteristics of the PDA10A2 must therefore be carefully accounted for in evaluating system performance.

The total noise power (N) at the receiver is quantitatively determined using Equation (6.9), which incorporates the detector's noise-equivalent bandwidth and various intrinsic noise sources, in accordance with established models for photodetector noise characterization (59). The precise calculation of this noise power is essential for accurately estimating the effective SNR, thereby enabling realistic assessments of the system's channel capacity and bit error rate (BER) under varying transmission conditions.

$$P_n = NEP_{\min} \times \frac{R_{\max}}{R(\lambda)} \times \sqrt{B} \tag{6.9}$$

NEP_{min} is the minimum noise equivalent power for the Thorlabs PDA10A2, which is $29.2pW/\sqrt{Hz}$. $R_{\max}$is the maximum responsivity of the PDA10A2, which is 0.44 A/W, and $R(\lambda)$ is the responsivity of the receiver at 475nm, 528nm, 583nm, and 625nm, which are 0.177A/W, 0.26A/W, 0.325A/W, and 0.382A/W, respectively (63). The SNR can be calculated from (6.10).

$$\frac{S}{N} = \frac{P_r}{\left(29.2 \times \frac{0.44}{R(\lambda)} \times \sqrt{B} \times 10^{-12}\right)} \tag{6.10}$$

Based on Shannon's formula, the maximum achievable information transmission rate C is determined by (6.11).

$$C = B \times \log_2\left(\frac{P_r}{(29.2 \times \frac{0.44}{R(\lambda)} \times \sqrt{B \times 10^{-12}})}\right) \tag{6.11}$$

S is the signal power (W), N is the noise power (W), P_r is the received power, and B is the channel bandwidth (Hz).

The Channel Impulse Response (CIR) plays a fundamental role in characterizing the propagation behavior of optical wireless communication (OWC) systems, particularly in underwater or water-filled environments. It encapsulates the temporal dispersion of the transmitted optical signal as it traverses the channel, accounting for key phenomena such as absorption, scattering, and multipath reflections. These factors collectively contribute to signal distortion, attenuation, and delay spread, all of which influence the integrity and performance of the communication link.

In the context of underwater optical communication, a widely adopted mathematical model for representing the CIR is presented in Equation (6.12). This model effectively captures the stochastic nature of photon interactions with suspended particles and refractive interfaces within the transmission medium, providing a comprehensive framework for assessing inter-symbol interference (ISI), system bandwidth limitations, and receiver design considerations.

$$h(t) = \frac{P_{rx}}{P_{tx}} \times \delta(t - \tau) \tag{6.12}$$

In this context, *h(t)* represents the channel impulse response (CIR), characterizing the temporal profile of the optical signal as it propagates through the water-filled medium. The term P_r denotes the received optical power at a transmission distance *d*, while P_t signifies the transmitted optical power from the source. The function $\delta(t-\tau)$ refers to the Dirac delta function, indicating that the signal arrives at the receiver at a specific time delay τ.

This delay is mathematically defined as $\tau = \frac{d}{C/n}$, where ccc is the speed of light in a vacuum, and *n* is the refractive index of water, typically approximated as 1.33. This expression captures the influence of the medium's optical properties on signal propagation time, forming the basis for temporal alignment and synchronization in underwater OWC systems (62).

A Python-based Monte Carlo simulation is utilized to model the Channel Impulse Response (CIR) for underwater optical wireless communication systems, as described in Gabriel., 2012. This simulation framework incorporates photon path tracing, the Henyey–Greenstein scattering phase function, and photon weighting techniques to effectively capture the combined effects of scattering, absorption, and surface reflections within the underwater environment (Appendix A.1).

As illustrated in Figure 6.12, the simulation results reveal a progressive increase in time delay (ΔT) with transmission distance. Specifically, the delay extends from 0.12 nanoseconds (ns) at a distance of 75 mm, to 0.125 ns at 225 mm, and reaches 0.13 ns at 375 mm. These findings highlight the sensitivity of CIR to propagation distance, emphasizing the growing temporal spread and signal distortion in longer-range underwater optical channels.

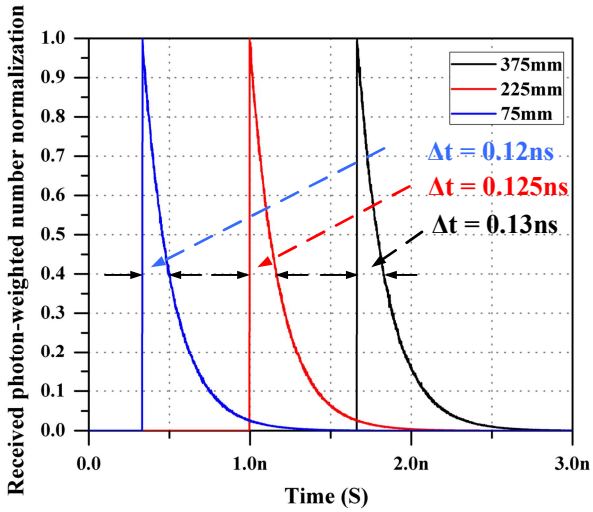

Figure 6.12 A time-domain broadening map employing Monte Carlo simulation.

The channel bandwidth is characterized by evaluating the Channel Frequency Response (CFR), which is derived by performing a Fourier Transform on the Channel Impulse Response (CIR). A Python-based computational framework is employed to simulate and compute the CFR under varying underwater optical propagation conditions. In the context of a water-filled pipe environment, the channel bandwidth is defined as twice as the sideband frequency identified in the CFR spectrum, as illustrated in Figure 6.13. From the simulation results, the average frequency bandwidth is computed to be approximately 1.66 GHz, indicating a broad frequency range suitable for high-speed data transmission in underwater optical channels.

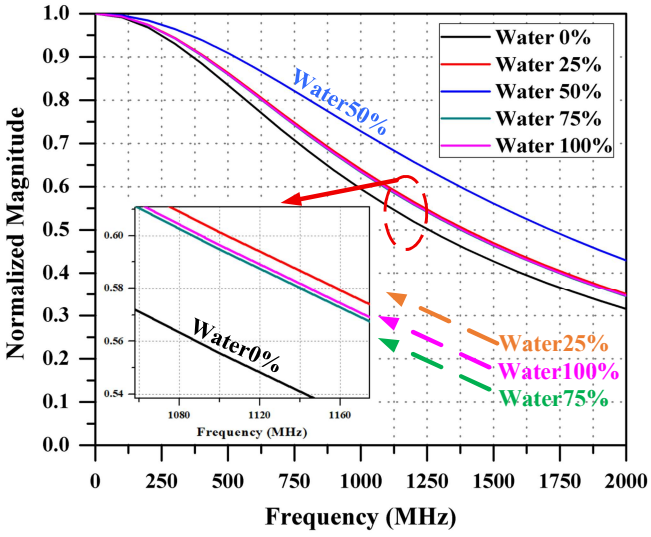

Figure 6.13 A Channel Frequency response (CFR).

Complementing the simulation-based CFR analysis, experimental measurements were conducted to determine the -3 dB frequency bandwidths of four different LED wavelengths. The -3 dB bandwidth is defined as the frequency at which the received optical signal power declines to 50% of its maximum value, corresponding to a 3 dB reduction from the peak power level.

Furthermore, to assess the communication system's efficiency, the obtained bandwidth values are integrated with the noise power data reported in Table 6-5. Using these parameters, the Signal-to-Noise Ratio (SNR) is calculated based on Equation (6.10). This comprehensive analysis enables a detailed evaluation of the system's transmission capabilities and supports performance optimization strategies for optical wireless communication (OWC) in submerged pipeline environments.

Table 6-5 The receiver noise power

Wavelength (nm)	Noise Power (nW)	R_{max} / R_{λ}
475	157	390.28
528	118	199.69
583	81.6	110.47
625	121	139.37

Table 6-6 summarizes the Signal-to-Noise Ratio (SNR) values obtained from experimental measurements conducted within a water-filled pipe environment. These SNR values are crucial for evaluating the performance of the optical wireless communication (OWC) system, as they directly impact the achievable data transmission rates.

To quantify the system’s channel capacity, the Shannon–Hartley Theorem was employed. This fundamental principle in communication theory provides a mathematical framework for determining the maximum theoretical data rate achievable over a communication channel in the presence of noise. By incorporating the measured signal-to-noise ratio (SNR) values and the corresponding frequency bandwidths, this analysis estimates the theoretical upper limit of the data transmission rate supported by the proposed OWC system under the given environmental and operational conditions.

In the experimental configuration, the LED transmitter was mounted at one end of the 350 mm PVC pipe, aligned along the pipe’s central axis, while the photodetector was positioned directly opposite at the other end. This fixed line-of-sight alignment ensured consistent optical coupling across all tested water levels.

The analytical results reveal that the channel capacity reaches its minimum at a 50% water level, where the LED beam path is partially submerged. This configuration introduces a complex air–water interface within the optical path, leading to increased scattering, refraction, and multipath distortion, which collectively reduce signal integrity and effective bandwidth. In contrast, the highest

channel capacity is observed under 0% water level (dry pipe) conditions, where the absence of water minimizes both absorption and scattering losses. The remaining water-level configurations yield decreasing capacities in the following order: 75%, 100%, and 25%, corresponding to varying degrees of optical disturbance and refractive index gradients along the LED-to-detector path.

Table 6-6 The signal to noise ratio (SNR)

	Signal to noise ratio (dB)				
Wavelength (nm)	Water 0%	Water 25%	Water 50%	Water 75%	Water 100%
475	-13.15	-16.8	-29.74	-15.83	-16.17
528	-16.11	-18.64	-32.85	-17.86	-18.06
583	-12.05	-19.48	-27.95	-18.18	-18.65
625	-8.66	-9.73	-23.71	-9.07	-9.22

Regarding LED frequency bandwidth, the 475 nm LED exhibits the widest measured bandwidth at 28.98 MHz, followed by the 625 nm LED (17.13 MHz), 528 nm LED (16.2 MHz), and 583 nm LED (7.81 MHz). Despite the superior bandwidth of the 475 nm LED, SNR analysis reveals a different trend. The 625 nm LED achieves the highest SNR among all tested wavelengths, recording –9.22 dB at 100% water level. In comparison, the 475 nm, 528 nm, and 583 nm LEDs yield SNR values of –16.17 dB, –18.06 dB, and –18.65 dB, respectively. These results collectively highlight the interplay between wavelength-dependent optical losses and water-level-induced scattering, both of which directly influence the achievable channel capacity in in-pipe optical wireless communication systems (64).

Across all water levels, the trend indicates that SNR values are maximized under dry conditions (0% water level) and reach their minimum at 50% water level, corresponding with the most severe scattering conditions. Consequently, the maximum achievable channel capacity occurs with the 625 nm LED, reaching up to 2.8 Mbps under full water submersion (100%). This is followed by the 475 nm LED at 1 Mbps, the 583 nm LED at 0.8 Mbps, and finally, the 528 nm LED at 0.4 Mbps.

These findings underscore the superior performance of the 625 nm wavelength in water-filled pipeline environments. Its combination of moderate bandwidth and significantly higher SNR enables it to deliver the highest data transmission capacity, reaching up to 2.8 Mbps at 100% water level, as illustrated in Figure 6.14, which presents the maximum channel capacity of LEDs in a water-filled pipe environment.

The results show a clear trade-off between modulation bandwidth and signal-to-noise ratio (SNR) across different LED wavelengths in the in-pipe environment. Although the 475 nm LED exhibits the widest frequency bandwidth, its performance

is limited by a relatively low SNR, particularly under water-filled conditions, due to stronger scattering and higher noise power at shorter wavelengths. As a result, its achievable channel capacity remains constrained despite the bandwidth advantage.

In contrast, the 625 nm LED consistently achieves the highest SNR across all water levels, including –9.22 dB at 100% water level, owing to reduced wavelength-dependent scattering and improved propagation stability in water. While its bandwidth is moderate compared to the 475 nm LED, the significantly higher SNR enables superior channel capacity, reaching up to 2.8 Mbps under full submersion. The observed minimum SNR at 50% water level further confirms that air–water interfaces introduce severe scattering and multipath effects, which degrade performance for all wavelengths.

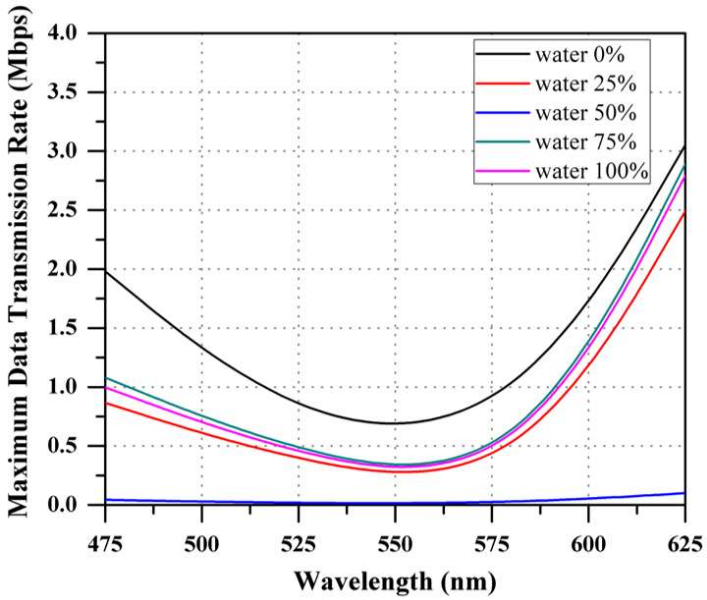

Figure 6.14 The LED's maximum channel capacity in an environment with water-filled pipes.

6.7 Discussion

This chapter presents an in-depth investigation into the propagation characteristics and performance of optical wireless communication (OWC) systems within water-filled pipelines. A theoretical framework incorporating Beer–Lambert Law, Fresnel reflection theory, and the Henyey–Greenstein phase function was employed to model light attenuation, refraction, and scattering. The experimental setup involved a 375 mm PVC pipe sealed with PMMA acrylic plates, within which five different LED wavelengths (475, 528, 583, 625, and 590 nm) were tested under varying water levels (0% to 100%).

Key optical phenomena such as beam divergence, spot size expansion, and surface scattering were characterized using Ansys Zemax OpticStudio simulations,

validated by experimental results. The results demonstrated that the highest signal attenuation and lowest received power consistently occurred at the 50% water level, due to significant refraction and scattering at the water-air interface. Conversely, the most favorable conditions for optical transmission were found at 0% and 100% water levels.

The performance of the system was further analyzed through frequency response, -3 dB bandwidth calculations, and signal-to-noise ratio (SNR) assessments. The 625 nm LED was identified as the optimal source for in-pipe communication, achieving the highest SNR and channel capacity (up to 2.8 Mbps), despite its lower bandwidth compared to the 475 nm LED. A Python-based Monte Carlo simulation was implemented to evaluate the channel impulse response (CIR) and derive channel frequency response (CFR), yielding an average channel bandwidth of 1.66 GHz in water.

- **Impact of Pipeline Diameter on Channel Conditions**

The diameter of the pipeline plays a crucial role in determining the optical wireless communication (OWC) channel characteristics. In narrow-diameter pipes, such as the 50 mm PVC pipe used in this study, the confined geometry significantly alters the propagation behavior compared with wider spaces such as laboratory tanks or open-water environments. The close proximity of the pipe walls increases the likelihood of surface reflections and multipath scattering, resulting in higher path loss and temporal dispersion of the received signal.

In contrast, wider propagation spaces such as laboratory test tanks exhibit more uniform beam spreading and a lower density of reflections, resulting in more stable line-of-sight (LOS) transmission. Although a narrow pipeline enhances signal confinement and alignment stability, it also introduces additional geometrical losses due to surface roughness and boundary scattering. Experimental observations confirm that these effects collectively reduce the received optical power and signal-to-noise ratio (SNR) when compared with larger-volume environments.

These findings verify that pipe diameter is a critical parameter influencing optical channel behavior and highlight the necessity of diameter-specific calibration when extrapolating OWC performance data from confined pipelines to open-tank or free-space configurations. Furthermore, this study provides the first experimental correlation between wavelength-dependent attenuation, scattering, and channel capacity variations in stratified water-filled pipelines. The results offer new empirical evidence that longer wavelengths, particularly 625 nm (red), exhibit superior propagation characteristics in confined aquatic media. This insight establishes practical design guidelines for robotic OWC systems operating in submerged or partially filled environments, contributing to significant advancement to the current state of the art in underwater optical communication.

Chapter 7

Conclusions and recommendations

7.1 Conclusions

This thesis has advanced the state-of-the-art in optical wireless communication (OWC) for confined and water-filled pipeline environments by establishing a comprehensive experimental and modeling framework that links optical, thermal, and communication performance parameters. The research addressed key limitations in prior studies, which predominantly examined OWC in open or homogeneous water channels, by developing and validating a practical in-pipe OWC model that captures the effects of stratified media, pipe surface reflections, and thermal behavior of high-power LEDs.

Compared with existing literature, which often treats underwater OWC links in free-space or short-range laboratory tanks, this work introduces a novel confined-pipeline communication model combining Ansys Zemax OpticStudio ray-tracing simulations, Keysight ADS circuit modeling, and empirical measurements across multiple wavelengths (410–625 nm). This integration establishes a new approach for predicting signal propagation in complex geometries, directly extending current knowledge in underwater photonic communication systems.

Three major research outcomes define the original contribution of this thesis:

- **Material and Optical Characterization**

The optical properties of PVC and stratified water interfaces were quantified through simulation and experiment, yielding wavelength-dependent absorption, reflection, and scattering data consistent with theoretical models. This work provides the first comprehensive dataset describing PVC–water optical behavior within pipeline geometries.

- **Quantified Thermal–Optical Coupling in LEDs**

A thermally optimized LED transmitter was developed, achieving a 6.3 K reduction in junction temperature, 245 % improvement in received optical power, and 35 % increase in modulation bandwidth compared to conventional designs. This quantifies, for the first time, the direct performance gain achievable through thermal management in LED-based OWC systems.

- **In-Pipe OWC Channel Modeling and Performance Evaluation**

Experimental measurements and Monte Carlo simulations revealed that 625 nm red light provides the optimal trade-off between SNR and attenuation in stratified pipelines, achieving up to 2.8 Mbps under full water conditions. The study identified 50 % water level as the most critical regime due to maximum scattering and refractive distortion—an insight not previously reported in the literature.

Together, these findings establish a quantifiable relationship between thermal optimization, wavelength selection, and channel behavior in confined aquatic environments. The thesis therefore extends the current understanding of underwater

OWC beyond open-water conditions and provides a validated foundation for next-generation robotic inspection and environmental monitoring systems operating in submerged pipelines.

In summary, this research contributes new theoretical insight, experimental evidence, and design methodology to the field of optical wireless communication—representing a significant addition to knowledge and a verifiable advancement of the state-of-the-art in photonic communication technologies for constrained environments.

7.2 Application of OWC for water-filled pipe environmental studies

The practical applicability of this study's findings is exemplified through their integration into the Pipe-Bot initiative under the Communication and Power Research Program (65). This initiative is aimed at developing autonomous robotic platforms capable of inspecting and monitoring underground infrastructure, particularly plastic pipelines. A critical component of this system is the deployment of optical wireless communication (OWC) to facilitate high-speed data exchange between robots operating within enclosed pipe environments. A visual representation of the Pipe-Bot in a pipe inspection scenario is illustrated in Figure 7.1.

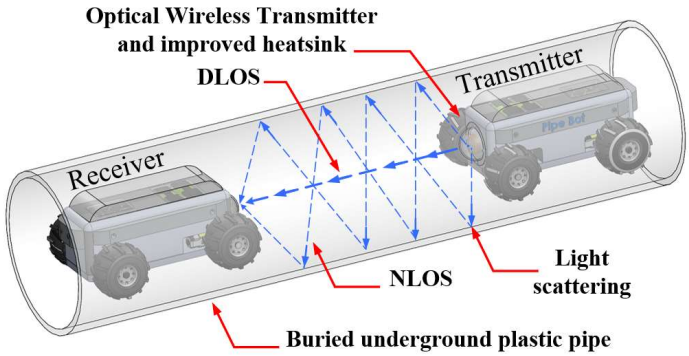

Figure 7.1 Integration of an optical wireless communication system into pipe inspection robot applications.

The insights gained from this research contribute significantly to the advancement of in-pipe communication systems. One of the primary design considerations informed by the findings is the selection of optimal LED wavelengths, chosen to minimize attenuation over specific transmission distances within water-filled pipelines. The characterization of five different LED wavelengths provided essential data on their frequency bandwidth performance and attenuation profiles in various water conditions, enabling more informed wavelength selection for reliable signal propagation.

Moreover, the thermal management strategies developed in this study have direct implications for real-world OWC system implementation. The improved heatsink design, featuring extended fin height and increased fin count, demonstrated

enhanced heat dissipation capabilities. This resulted in lower operating temperatures, faster thermal response times, and improved LED performance. These enhancements translated to higher received optical power and broader modulation bandwidths, which are critical parameters for maintaining robust data transmission under thermally constrained conditions.

In practical applications, such as robotic pipeline inspection, environmental variables such as fluctuating water levels present significant challenges for maintaining communication integrity. To address this, the research has been extended to the development of an Automatic Gain Control (AGC) system. Integrated into the Pipe-Bot platform, the AGC dynamically adjusts the gain of the photodetector receiver circuit in real time. This adjustment compensates for signal fluctuations caused by varying water levels, which affect the degree of light scattering and absorption along the communication path. As illustrated in Figure 7.2, the AGC module enhances the system's ability to maintain stable signal reception and consistent communication quality, even under dynamically changing optical propagation conditions.

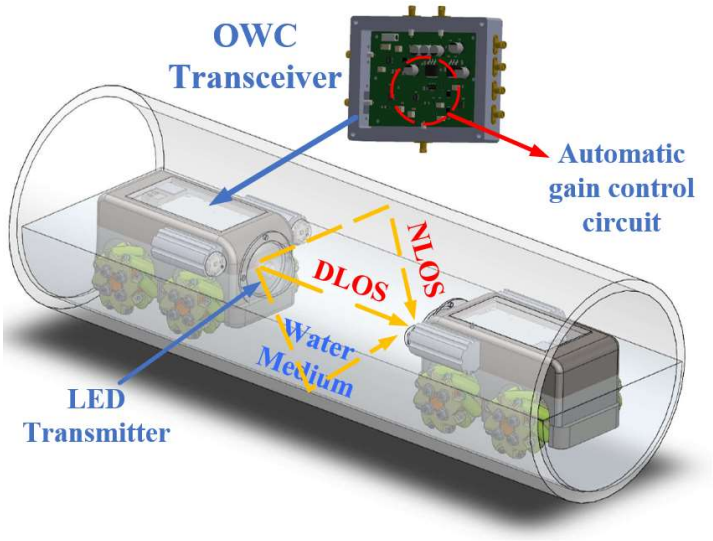

Figure 7.2 Utilization of OWC for environmental investigations involving water-filled pipes.

In summary, the practical deployment of the OWC system within the Pipe-Bot framework demonstrates the translational potential of the research. It provides a foundation for developing intelligent, resilient, and efficient communication modules for autonomous inspection robots operating in water-filled pipeline environments. These applications contribute not only to improved infrastructure maintenance but also to the broader advancement of optical wireless technologies in confined and submerged environments.

7.3 Summary of Key Contributions and Novelty

This research advances state-of-the-art in Optical Wireless Communication (OWC) for confined pipelines and underwater environments through the following original contributions:

- Novel In-Pipe Optical Channel Characterization: Developed and experimentally validated a multi-wavelength OWC testbed for confined PVC pipelines, offering one of the first detailed comparisons of LED transmission properties (410–625 nm) in air- and water-filled conditions.
- Integrated Optical Component Optimization: Introduced a combined reflector–lens optical configuration that enhances in-pipe received optical power by up to 20 dB, verified through Ansys Zemax simulations and laboratory experiments.
- Thermal–Optical Coupling Model for High-Power LEDs: Designed and validated an optimized square-fin heatsink structure that improves LED bandwidth by up to 35%, providing a quantifiable relationship between thermal control and communication efficiency.
- Wavelength-Dependent Water Transmission Analysis: Quantified the attenuation and scattering effects of varying water levels and stratified layers, establishing wavelength selection criteria for robust communication in partially filled pipelines.
- Integration Toward Robotic Systems: Demonstrated the applicability of the developed OWC model for real-world robotic pipeline inspection (PipeBot) by implementing an Automatic Gain Control (AGC) photodetector module to maintain stable performance under dynamic optical conditions.

Collectively, these contributions represent a significant advancement in understanding and designing practical, energy-efficient OWC systems for confined environments — bridging a key research gap between theoretical optical modeling and deployable robotic communication systems.

7.4 Recommendations for future work

This thesis has explored the design, implementation, and performance evaluation of optical wireless communication (OWC) systems in both air- and water-filled pipeline environments. While the findings provide significant insights, several opportunities remain for further investigation to extend and enhance this research. The following recommendations outline potential directions for future work:

- Development of Adaptive Modulation Techniques

This study employed analog and return-to-zero (RZ) digital modulation schemes. Future research should investigate adaptive modulation strategies such as pulse position modulation (PPM), orthogonal frequency-division multiplexing (OFDM), or quadrature amplitude modulation (QAM). These techniques could dynamically adjust to varying channel conditions, enhancing reliability and data throughput, particularly in environments with fluctuating water clarity and turbidity.

- Implementation of Error Correction Protocols

Introducing forward error correction (FEC) codes like Reed-Solomon or LDPC could improve bit error rate (BER) performance, especially under high-attenuation scenarios such as partial water fills or multipath conditions. Experimental validation of these protocols could help optimize system performance for real-world deployment.

- Investigation of Underwater MIMO Systems

While this study focused on single-LED and single-photodetector configurations, future work may explore multiple-input multiple-output (MIMO) systems. Employing arrays of LEDs and photo detectors could mitigate scattering-induced signal loss and increase channel capacity in submerged pipeline scenarios.

- Real-Time Thermal Feedback Control

The results highlighted the importance of thermal management in sustaining LED performance. A promising extension would be to implement a real-time thermal feedback system that dynamically adjusts drive current or modulation rate based on temperature measurements. This would enable more efficient energy use and protect components from thermal degradation.

- Integration with In-Pipe Robotic Systems

The OWC system developed here is a strong candidate for integration with autonomous or semi-autonomous in-pipe inspection robots. Future work should investigate the mechanical and control interface requirements to achieve seamless data transmission between mobile platforms and fixed receivers, particularly in long-range or multi-hop scenarios.

- Extended Transmission Distance Studies

This work was limited to a 375 mm pipe segment. Investigating longer distances (e.g., 1 m and beyond) will be essential to evaluate the scalability of the proposed system. This could involve analyzing the impact of multiple scattering events, backscattering, and misalignment over extended paths.

- Long-Term Stability and Reliability Testing

Real-world applications require OWC systems that remain stable over extended periods. Further experiments under varying environmental conditions (e.g., temperature, water contamination, and vibration) could assess the robustness and longevity of the system.

These recommendations aim to guide the next stages of development in underwater and in-pipe optical communication research. They are particularly relevant for advancing smart infrastructure systems, robotic pipeline monitoring, and next-generation optical IoT applications in constrained environments.

References

[1] T. Komine and M. Nakagawa, "*Fundamental analysis for visible-light communication systems using LED lights*," IEEE Trans. Consum. Electron., vol. 50, no. 1, pp. 100–107, 2004.

[2] P. K. Pathak, G. Dutta, and P. Sharma, "*Visible light communication, networking, and sensing: A survey, potential and challenges*," IEEE Commun. Surveys Tuts., vol. 17, no. 4, pp. 2047–2077, 2015.

[3] H. Kaushal and G. Kaddoum, "*Underwater optical wireless communication*," IEEE Access, vol. 4, pp. 1518–1547, 2016.

[4] I. F. Akyildiz, D. Pompili, and T. Melodia, "*Underwater acoustic sensor networks: Research challenges*," Ad Hoc Netw., vol. 3, no. 3, pp. 257–279, 2005.

[5] M. Stojanovic and J. Preisig, "*Underwater acoustic communication channels: Propagation models and statistical characterization*," IEEE Commun. Mag., vol. 47, no. 1, pp. 84–89, 2009.

[6] M. Doniec, C. Detweiler, I. Vasilescu, and D. Rus, "*Power-efficient underwater communication using narrow-beam optical modems*," IEEE Commun. Mag., vol. 51, no. 7, pp. 22–28, 2013.

[7] G. N. Arvanitakis, D. Tsonev, J. J. D. McKendry, A. M. Khalid, E. Xie, E. Gu, and M. D. Dawson, "*Gb/s underwater wireless optical communications using series-connected GaN micro-LED arrays*," IEEE Photonics Journal, vol. 12, no. 2, Apr. 2020, Art. no. 7901210.

[8] W. Ge, Z. Li, Y. Song, Z. Li, and J. Han, "*90-m/560-Mbps underwater wireless optical communication using subband multi-mode full permutation CAP*," Optics Express, vol. 31, no. 8, p. 13154, 2023.

[9] M. Zhang and H. Zhou, "*Real-Time Underwater Wireless Optical Communication System Based on LEDs and Estimation of Maximum Communication Distance*," Sensors, vol. 23, no. 17, Art. no. 7649, 2023, doi:10.3390/s23177649.

[10] J. Nie, L. Tian, H. Wang, L. Chen, Z. Li, S. Yue, Z. Zhang, and H. Yang, "*Adaptive beam shaping for enhanced underwater wireless optical communication*," Optics Express, vol. 29, no. 17, pp. 26404–26417, 2021, doi:10.1364/OE.434387.

[11] H. Luo, Z. Xu, J. Wang, Y. Yang, R. Ruby, and K. Wu, "*Reinforcement Learning-Based Adaptive Switching Scheme for Hybrid Optical–Acoustic AUV Mobile Network*," Wireless Communications and Mobile Computing, vol. 2022, Art. ID 9471698, 14 pp., May 2022, doi: 10.1155/2022/9471698.

[12] Z. Li, C. Loadz, and L. Wen, "*Energy-Efficient MIMO Visible Light Communication System with Adaptive Bias Control and OFDM*," IEEE Internet of Things Journal, vol. 6, no. 3, pp. 4512–4523, Sept. 2019, doi:10.1109/JIOT.2018.2876534.

[13] C. D. Mobley, *Light and Water: Radiative Transfer in Natural Waters*. San Diego, CA: Academic Press, 1994.

[14] N. C. Tien, Y. T. Yeh, and S. Chi, "*Surface roughness affects light scattering and photonic device performance*," Appl. Opt., vol. 46, no. 5, pp. 750–758, 2007.

[15] S. Q. Duntley, "*Light in the sea*," J. Opt. Soc. Am., vol. 53, no. 2, pp. 214–233, 1963.

[16] J.-M. Tualle, A. Sentenac, and M. L. Denis, "*Scattering and absorption properties of suspensions: Application to particulate media*," Applied Optics, vol. 43, no. 9, pp. 1850–1857, Mar. 2004.

[17] R. Paschotta, "*Fresnel equations*," RP Photonics Encyclopedia, 2024. [Online]. Available: https://doi.org/10.61835

[18] E. Hecht, *Optics*, 5th ed. Pearson Education, 2017.

[19] N. Sultanova, S. Kasarova, and I. Nikolov, "*Dispersion properties of optical polymers*," Acta Phys. Pol. A, vol. 116, no. 4, pp. 585–587, 2009.

[20] N. G. Jerlov, *Marine Optics*. Elsevier, 1976.

[21] I. Moreno, "*Modeling the radiation pattern of LEDs*," Opt. Express, vol. 16, no. 3, pp. 1808-1817, 2008.

[22] Z. Ghassemlooy, W. Popoola, and S. Rajbhandari, *Optical Wireless Communications: System and Channel Modelling with MATLAB®*. CRC Press, 2013.

[23] A. Ryer, *Light Measurement Handbook*. International Light Technologies, 1998.

[24] Lumileds, *Thermal Management of High-Power LEDs*, Application Brief AB32, 2017.

[25] F. P. Incropera, D. P. DeWitt, T. L. Bergman, and A. S. Lavine, *Fundamentals of Heat and Mass Transfer*, 6th ed. Wiley, 2007.

[26] A. Bar-Cohen and W. M. Rohsenow, *Thermal Analysis and Control of Electronic Equipment*. McGraw-Hill, 1984.

[27] N. U. Hassan et al., "*Channel characterization for underwater wireless optical communication*," IEEE Access, vol. 8, pp. 73610–73624, 2020.

[28] A. Al-Kinani, C.-X. Wang, L. Zhou, and W. Zhang, "*Optical wireless communication channel measurements and models*," IEEE Commun. Surveys Tuts., vol. 20, no. 3, pp. 1939–1962, 2018.

[29] Z. Zhang, "*Refractive index of $(C_2H_3Cl)_n$ (Polyvinyl chloride, PVC)*," RefractiveIndex.info, 2024. [Online]. Available: https://refractiveindex.info

[30] D. Attwood, *Soft X-Rays and Extreme Ultraviolet Radiation: Principles and Applications*. Cambridge, U.K.: Cambridge University Press, 1999, p. 60.

[31] V. Argueta-Díaz, *Optical Sensors*. Google Books, 2023.

[32] K. E. Oughstun and C. L. Palombini, "*Fresnel Reflection and Transmission Coefficients for Temporally Dispersive Attenuative Media*," Radio Science, vol. 53, no. 11, pp. 1382–1397, Nov. 2018, doi: 10.1029/2018RS006646.

[33] R. H. Stavn, "*Lambert-Beer law in ocean waters: Optical properties of water and dissolved/suspended material*," Optical Energy Budgets, North Carolina Univ., 1988.

[34] K. Boonlom, P. Chomtong, W. Zhang, T. J. Amsdon, J. Oberhammer, I. D. Robertson, and N. Somjit, "*Advanced studies on optical wireless communications for in-pipe environments: Bandwidth exploration and thermal management*," IEEE Access, vol. 12, pp. 80607–80632, 2024.

[35] V. Purcar et al., "*Preparation and characterization of some sol-gel modified silica coatings deposited on polyvinyl chloride (PVC) substrates*," Coatings, vol. 11, no. 1, p. 11, 2020.

[36] L. J. Ippolito, *Radio Wave Propagation in Satellite Communications*. Springer, 2012.

[37] A. N. Khan et al., "*Atmospheric turbulence and fog attenuation effects in controlled environment FSO communication links*," IEEE Photon. Technol. Lett., vol. 34, no. 24, pp. 1341–1344, 2022.

[38] M. Fujii, J. Leuthold, and W. Freude, "*Dispersion relation and loss of subwavelength confined mode of metal-dielectric-gap optical waveguides*," IEEE Photon. Technol. Lett., vol. 21, no. 6, pp. 362–364, 2009.

[39] N. J. Veck, "*Atmospheric transmission and natural illumination (visible to microwave regions)*," GEC J. Res., vol. 3, no. 4, pp. 209–223, 1985.

[40] G. Y. Hu, C. Y. Chen, and Z. Q. Chen, "*Free-space optical communication using visible light*," J. Zhejiang Univ. Sci. A, vol. 8, no. 2, pp. 186–191, 2007.

[41] M. A. Abd Ali and M. A. Mohammed, "*Effect of atmospheric attenuation on laser communications for visible and infrared wavelengths*," J. Al-Nahrain Univ. Sci., vol. 16, no. 3, pp. 133–140, 2013.

[42] A. Kaur, N. Sharma, and J. Singh, "*Selection of suitable wavelengths for dual-wavelength model of free space optics (FSO) systems for high-speed trains*," J. Opt. Commun., Aug. 2020.

[43] A. G. Alkholidi and K. S. Altowij, "*Free space optical communications—Theory and practices*," in Contemporary Issues in Wireless Communications. InTech, 2014.

[44] X. C. Tong, *Advanced Materials for Thermal Management of Electronic Packaging*. Springer, 2011.

[45] C. J. Lasance and A. Poppe, *Thermal Management for LED Applications*. Springer, 2013.

[46] A. Gaikwad, A. Sathe, and S. Sanap, "*A design approach for thermal enhancement in heat sinks using different types of fins: A review*," Frontiers in Thermal Engineering, vol. 2, Jan. 2023, Art. no. 980985, doi:10.3389/fther.2022.980985.

[47] T. J. Amsdon, "*Implementation of a VLC HDTV distribution system for consumer premises*," Ph.D. dissertation, Univ. of Huddersfield, Huddersfield, U.K., 2020.

[48] H. Huang, "*Improving modulation bandwidth and optical power of GaN-based blue LED by hollow-runway active area*," Microw. Opt. Technol. Lett., vol. 62, no. 6, pp. 2123–2127, 2020.

[49] C.-L. Liao et al., "*High-speed light-emitting diode emitting at 500 nm with 463-MHz modulation bandwidth*," IEEE Electron Device Lett., vol. 35, no. 5, pp. 563–565, 2014.

[50] A. Alexeev and J.-P. Linnartz, "*Optical wireless communication model for LED bandwidth based on electrical small-signal response analysis*," in Proc. 16th International Symposium on the Science & Technology of Lighting (ISSTL), Sheffield, UK, 2018.

[51] R. Wan, Y. Ding, Z. Li, H. Wu, and Y. Qian, "*Improving the modulation bandwidth of GaN-based light-emitting diodes*," Adv. Photonics Res., vol. 2, no. 11, art. no. 2100093, 2021.

[52] W.-K. Chen, *The Circuits and Filters Handbook*, 3rd ed., vol. 1–5. Boca Raton, FL, USA: CRC Press, 2009.

[53] H. J. Landau, "*Sampling, data transmission, and the Nyquist rate*," Proc. IEEE, vol. 55, no. 10, pp. 1701–1706, 1967.

[54] C. E. Shannon, *The Mathematical Theory of Communication. Urbana*, IL: University of Illinois Press, 1949.

[55] F. Wu, L. Chen, S. Cai, and W. Wang, "*Experimental Study and Application of Response Mask Invariant Characteristic for Generalized Visible Light Communication Channel*," IEEE Photonics Journal, vol. 10, no. 3, pp. 1–12, Jun. 2018, Art. no. 7903912, doi: 10.1109/JPHOT.2018.2834384.

[56] E. Salik, "*Quantitative investigation of Fresnel reflection coefficients by polarimetry*," Am. J. Phys., vol. 80, no. 3, pp. 216–224, 2012.

[57] A. I. Vistnes, "*Reflection, transmission and polarization*," in Physics of Oscillations and Waves. Cham, Switzerland: Springer, 2018.

[58] Y. Yang, F. He, Q. Guo, M. Wang, J. Zhang, and Z. Duan, "*Analysis of underwater wireless optical communication system performance*," Applied Optics, vol. 58, no. 36, p. 9808, 2019, doi: 10.1364/AO.58.009808.

[59] Z. Vali et al., "*Use of Gaussian beam divergence to compensate for misalignment of underwater wireless optical communication links*," IET Optoelectron., vol. 11, no. 5, pp. 171–175, 2017.

[60] R. C. Smith and K. S. Baker, "*Optical properties of the clearest natural waters (200–800 nm)*," Appl. Opt., vol. 20, no. 2, p. 177, 1981.

[61] C. A. Williamson and R. C. Hollins, "*Measured IOPs of Jerlov water types*," Appl. Opt., vol. 61, no. 33, p. 9951, 2022.

[62] Encyclopaedia Britannica, "*Refractive index*," Aug. 12, 2024. [Online]. Available: https://www.britannica.com/science/refractive-index

[63] K. Boonlom, N. Chudpooti, S. Rungraungsilp, W. Zhang, T. J. Amsdon, J. Oberhammer, and N. Somjit, "*Multiwavelength optical sensing of water-level stratification in closed plastic pipelines using signal attenuation and CIR analysis*," IEEE Sensors Journal, vol. 25, no. 19, pp. 35991–36001, Oct. 1, 2025, doi: 10.1109/JSEN.2025.3598923.

[64] N. Chudpooti, K. Boonlom, S. Rungraungsilp, P. Akkaraekthalin, W. Zhang, T. J. Amsdon, J. Oberhammer, and N. Somjit, "*Multiwavelength characterization of optical wireless communication in complex water-filled pipe environment*," IEEE Access, vol. 13, pp. 163418–163430, 2025, doi: 10.1109/ACCESS.2025.3610711.

[65] Pipebots, "*Theme 6: Communication and power*," 2023. [Online]. Available: https://pipebots.ac.uk/themes/theme-6-communication-and-power/

[66] M. Planck, *The Theory of Heat Radiation, Dover Publications*, New York, 1959.

Appendices

Appendix A Python Simulation Code

A.1 code for Monte Carlo channel impulse response simulations

Function: main.m

```
import numpy as np
import matplotlib.pyplot as plt
import pandas as pd

# Parameters
num_photons = 2500000                # Number of photons to simulate
transmitter_power = 0.52             # Transmitter power in arbitrary units
distance = 0.375                     # Direct distance between transmitter and
receiver in meters
total_attenuation_coefficient = 12.151  # Total attenuation coefficient in
m^-1
scattering_angle_deg = 60            # Fixed scattering angle in degrees
time_resolution = 1e-10              # Time resolution in seconds
max_delay = 10e-9                    # Maximum delay in seconds
eta = 7.53176E-07                    # Receiver Collection Efficiency

# Speed of light in water (considering refractive index of water)
speed_of_light_in_water = 3e8 / 1.33

# Time bins for CIR
time_bins = np.arange(0, max_delay, time_resolution)
photon_counts = np.zeros_like(time_bins)

# Convert fixed scattering angle to radians
scattering_angle = np.radians(scattering_angle_deg)

# Monte Carlo Simulation for photon delay and attenuation with fixed
scattering angle
np.random.seed(42)  # For reproducibility

for _ in range(num_photons):
    total_path_length = 0
    current_position = 0
    photon_alive = True
```

```
    while photon_alive:
        step_length = np.random.exponential(scale=1 /
total_attenuation_coefficient)
        total_path_length += step_length
        current_position += step_length

        delay = total_path_length / speed_of_light_in_water
        amplitude = transmitter_power * np.exp(-
total_attenuation_coefficient * total_path_length) * eta

        if current_position >= distance:
            bin_idx = int(delay / time_resolution)
            if bin_idx < len(time_bins):
                photon_counts[bin_idx] += amplitude
            photon_alive = False

# Normalize photon counts for plotting
photon_counts_normalized = photon_counts / np.max(photon_counts)

# Plot CIR as a time-domain broadening map
plt.figure(figsize=(10, 5))
plt.plot(time_bins * 1e9, photon_counts_normalized, color='blue',
linewidth=1.5)
plt.xlabel('Time (ns)')
plt.ylabel('Normalized Photon Count')
plt.title('Time-Domain Broadening Map of Optical Signals (Fixed 60°
Scattering Angle)')
plt.grid()
plt.show()

# Find ΔT in time domain
half_power_level = 0.5
peak_idx = np.argmax(photon_counts_normalized)
left_idx = np.where(photon_counts_normalized[:peak_idx] <
half_power_level)[0][-1] + 1
right_idx = peak_idx + np.where(photon_counts_normalized[peak_idx:]
< half_power_level)[0][0] - 1
delta_t = (time_bins[right_idx] - time_bins[left_idx])  # in seconds
```

```
print(f"Time interval Δt at 0.5 of normalized power: {delta_t * 1e9:.2f}
ns")

# Frequency Bandwidth Calculation from ΔT
frequency_bandwidth_from_delta_t = 1 / delta_t * 1e-6  # in MHz
print(f"Estimated Frequency Bandwidth from ΔT:
{frequency_bandwidth_from_delta_t:.2f} MHz")

# Frequency Response Calculation (Fourier Transform)
frequency_response = np.fft.fft(photon_counts_normalized)
freqs = np.fft.fftfreq(len(time_bins), d=time_resolution)
frequency_response_magnitude = np.abs(frequency_response)

# Normalize frequency response to 1
frequency_response_magnitude_normalized =
frequency_response_magnitude /
np.max(frequency_response_magnitude)

# Plot Frequency Response with -3 dB level
plt.figure(figsize=(10, 5))
plt.plot(freqs[:len(freqs)//2] * 1e-6,
frequency_response_magnitude_normalized[:len(frequency_response_m
agnitude)//2], color='red', linewidth=1.5)
plt.axhline(y=0.707, color='green', linestyle='--', linewidth=1)  # -3 dB
level line
plt.xlabel('Frequency (MHz)')
plt.ylabel('Normalized Magnitude')
plt.title('Channel Frequency Response')
plt.grid()
plt.show()

# Calculate -3 dB Bandwidth in Frequency Domain
half_power_magnitude = 0.707
bandwidth_indices =
np.where(frequency_response_magnitude_normalized >=
half_power_magnitude)[0]
bandwidth_freqs = freqs[bandwidth_indices]

# Calculate bandwidth in MHz
frequency_bandwidth = (np.max(bandwidth_freqs) -
```

```
np.min(bandwidth_freqs)) * 1e-6
print(f"Estimated Frequency Bandwidth from Frequency Domain:
{frequency_bandwidth:.2f} MHz")

# Save Frequency Response and Bandwidth to CSV
frequency_response_data = {
   'Frequency (MHz)': freqs[:len(freqs)//2] * 1e-6,
   'Normalized Magnitude':
frequency_response_magnitude_normalized[:len(frequency_response_m
agnitude)//2]
}
df_freq = pd.DataFrame(frequency_response_data)
df_freq.to_csv('CFRBW.csv', index=False)

# Append bandwidth information to the CSV file
with open('CFRBW.csv', 'a') as f:
   f.write(f"\nEstimated Frequency Bandwidth (MHz) from Time
Domain, {frequency_bandwidth_from_delta_t:.2f}")
   f.write(f"\nEstimated Frequency Bandwidth (MHz) from Frequency
Domain, {frequency_bandwidth:.2f}")

print("Frequency response and bandwidth data saved to CFRBW.csv")
```

Appendix B Thorlabs PDA10A2 Optical Receiver Specification

B.1 Thorlabs PDA10A2 Optical Receiver Specification

The Thorlabs PDA series is well-suited for detecting both pulsed and continuous-wave (CW) light sources. The PDA10A2 model features a reverse-biased PIN photodiode integrated with a fixed-gain transimpedance amplifier, all enclosed in a durable housing.

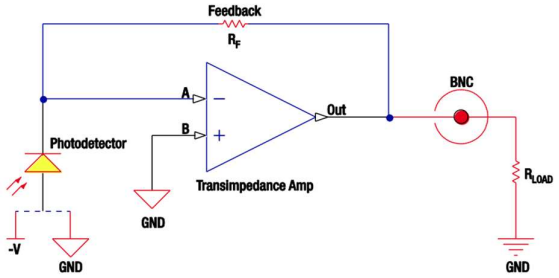

All performance specifications are typical values measured at an ambient temperature of 25 °C with a 50 Ω load, unless otherwise specified.

Electrical Specifications[2]		
Detector	-	Si
Active Area	-	Ø1 mm (0.8 mm^2)
Wavelength Range[3]	λ	200 to 1100 nm
Peak Wavelength	λ_p	730 nm (Typ)
Peak Response	$\Re(\lambda_p)$	0.44 A/W (Typ)
Small Signal Bandwidth	-	150 MHz
NEP (λ_p)	W/√Hz	2.92×10^{-11}
Noise (RMS)	-	1.5 mVrms
Max Ouput Current	I_{OUT}	100 mA
Dark Offset	-	±10 mV
Load Impedance	-	50 Ω to Hi-Z
Transimpedance Gain	-	5×10^3 V/A (50 Ω) 1×10^4 V/A (Hi-Z)
Output Voltage	V_{OUT}	0 to 5 V (50 Ω) 0 to 10 V (Hi-Z)

3D view of the Thorlabs PDA10A2 Optical Receiver